

M.Sc. Thesis
Master of Science in Engineering

DTU Construct

Department of Civil and Mechanical Engineering

Nonlinear State Estimation via Machine Learning

Lars K. Fogh s163761
Gabriele Mauro s202277

Kongens Lyngby 2023



Title: Nonlinear State Estimation via Machine Learning

Authors: Gabriele Mauro s202277 & Lars K. Fogh s163761

Period: August 29th 2022 - January 29th 2023

Language: English

ECTS: 30

University: Technical University of Denmark

Supervisors: Martin Skovgaard Andersen & Evangelos Katsanos

Co-supervisors: Andreas Asp Bock & Luigi Caglio

DTU Construct

Department of Civil and Mechanical Engineering

Technical University of Denmark

Koppels Allé

Building 404

2800 Kongens Lyngby, Denmark

Phone +45 4525 1960

www.construct.dtu.dk

Preface

This project was prepared in the Department of Civil and Mechanical Engineering at the Technical University of Denmark as part of the fulfillment of the requirements for acquiring a Master's degree in Civil Engineering.

The project accounts for 30 ECTS from each of the two authors, and have been carried out in the period between August 29th 2022 and January 29th 2023.

Both authors have discussed and contributed to the entirety of the report. Meaning that both parties are responsible, in the greater sense, for the complete and finalized report.

Supervisors:

Associate Professor Martin Skovgaard Andersen, DTU Compute

Associate Professor Evangelos Katsanos, DTU Construct

Postdoc Andreas Asp Bock, DTU Compute

PhD student Luigi Caglio, DTU Construct

Kongens Lyngby, Denmark, January 29th 2023



Gabriele Mauro s202277



Lars K. Fogh s163761

Abstract

The following thesis focuses on the topic of state estimation via machine learning. Here, state estimation refers to the prediction of acceleration responses from a reinforced concrete frame structure which has been excited with strong ground motions. The main objective has been to predict responses in one part of the structure given input responses from a different location.

An initial number of 301 ground motions have been selected and scaled such that a total number of 903 ground motions have been used to excite the structure. The structure has been modelled using OpenSees, from where the responses have been recorded in all free nodes. The materials defined in the model follow nonlinear constitutive law, therefore, the structure might respond in the non-linear regime. This implies that the generated responses can be associated with a structure operating either in the linear or non-linear domain, according to the intensity of the exciting ground motion.

Two machine learning models, namely a Gaussian Process (GP) and a Neural Network (NN), have then been trained and tested with the obtained structural responses in order for the models to predict accelerational time series responses. From the predictions of the two models, it has been seen that it is possible to predict the responses given an input response from a different location. Especially when the inputs are located on the same floor as the predictions, they then are most accurate. When the input and predictions are to be on different floors, predictions are still possible but less accurate. The NN performs, in general, better than the GP, both in terms of accuracy of the predictions as well as computational time. Even when noise is added to the input responses, the NN is able to make predictions with only slight implications on the accuracy. The NN further scales well in terms of training data. However, the NN does not give a deep insight into any physical relationship between the input responses and predictions. On the contrary, the GP does not scale well in terms of training data, and is therefore limited to smaller sets that must be selected based on the matching characteristics of the predicted responses. However, when using the GP, the predictions are associated with uncertainty measures.

Keywords: Gaussian Process, Neural Network, State estimation, Response prediction, Non-linear responses, OpenSees.

Acknowledgements

First of all, we would like to show our gratitude toward our supervisors Martin S. Andersen, Evangelos Katsanos, Andreas A. Bock, and Luigi Caglio. Your dedication to the project has been crucial for its progress, including the weekly meetings that have indeed been appreciated, in order to steer the project forward and have constructive discussions about further work. The final result could not have been obtained without these.

With all of you coming from two main focus areas, namely structural engineering and computer science, it has been a great journey being able to traverse topics within both fields and being able to combine them. All of you have contributed with helpful advice, whether this has been within modelling in OpenSees, where to look for inspiration regarding structural parameters, or which approaches within machine learning would be suitable for the given topic.

We would also like to show our appreciation to our families and friends who have been a great support throughout the entire process. Not only during this project but for the entirety of our education.

From the two of us, a great thank you to all of you.

Contents

Preface	i
Abstract	iii
Acknowledgements	v
Contents	vii
List of Figures	xi
List of Tables	xvi
Symbols	xix
1 Introduction	1
2 Methodology	5
2.1 Project Methodology	5
2.2 Machine Learning Methodology	6
2.3 The Gaussian Processes	11
2.4 Neural Networks	16
3 Structural Dynamics	23
3.1 Degrees of Freedom	23
3.2 Defining Matrices	29
3.3 Non-linearity	32
4 Finite Element Model	37
4.1 Structure	37
4.2 Preliminary analyses	44
4.3 Investigations of Dynamic loads	49
5 Results: Gaussian Process Regression	69
5.1 Preliminary study	69
5.2 Overall assessment of the model	82
5.3 Influence of the final structural damage state	86

6 Results: Neural Network	93
6.1 Overall assessment	93
6.2 Comparison	99
6.3 Noise	103
7 Conclusion & Further studies	111
7.1 Summary	111
7.2 Discussion	112
7.3 Further Work	113
7.4 Conclusion	116
References	119
A Structural Model - Finite Element Model	125
A.1 Equation of Motion	125
A.2 Newmark Integration	130
B Material properties of confined concrete	133
B.1 Mander Material	133
B.2 Confined Concrete Parameters	135
C Degree of Reinforcement	137
D OpenSees: Analysis & Load Application	139
D.1 Analysis Creation	139
D.2 Load application	140
E Gaussian Process	141
E.1 Ground motions - train set	141
E.2 Preliminary study for GM CHICHI-HWA033-N (ID 23)	144
E.3 Overall assessment for GM CHICHI-HWA033-N (ID 23)	148
F Gaussian Process - Error Matrices	149
F.1 Error Matrix for the entire structure	149
F.2 Error Matrix for each floor	151
F.3 Error distribution	152
G Neural Network - Responses related to the LDA & NDS Load-sets	154
H Comparison Gaussian Process & Neural Network	157
H.1 Comparison of mean error for each floor	157
H.2 Error Distributions	159
I Neural Network - Error Distribution	161

I.1	Distributions of error with noise	161
J	Project Plan	165
J.1	Initial Project Concept: 28-09-2022	166
J.2	Revised Project Concept: 29-01-2023	167
J.3	Evaluation of the project process	167

x

List of Figures

2.1	Visualization of sub-vectors z_i with length $l = 5$ and step-size $s = 3$	8
2.2	Samples from zero-mean GP priors with k_{SE} as covariance function [34].	13
2.3	Gaussian process regression using zero-mean GP prior with k_{SE} as covariance function. With noise level $\sigma_\varepsilon^2 = 1$ and a) $n = 10$, and b) $n = 20$ training examples x_n indicated with dots. The true function is given in a solid line (—), whereas the prediction is given in a dashed line (---). The 95 % confidence range based on the matrix Σ^* is shaded [20].	15
2.4	Example of a NN architecture with 1 hidden layer including 2 neurons [40].	17
2.5	NN: — training MSE curve, — testing MSE curve. Simulation with 20 hidden-neurons and learning rate fixed at $f_{lr} = 4 \cdot 10^{-5}$. GMs: 301. Input: node 23. Output: node 42.	21
3.1	Schematic of an internal damped mass-spring, with a single degree of freedom [62].	24
3.2	Free vibrations of under-damped, critically damped, and over-damped systems [63].	26
3.3	Schematic of a 2 degrees of freedom system [62].	28
3.4	Rayleigh damping including components of α - and β -terms.	31
3.5	Damping ratio as a function of natural frequency using two methods of Rayleigh Damping.	32
3.6	Strain-stress curves for a) steel and b) concrete.	33
3.7	Approaches to determine constitutive relation between force and deformation using a) linear approach and b) non-linear step approach.	34
4.1	FE model of the RC frame structure. Column height of $h = 3.5$ m and beam length of $L = 5.5$ m. Nodes (in blue) are two digits located at intersections of structural elements, and elements (in red) are four digits composed of two node-ends.	38
4.2	Cross sections for the structural elements. Both cross sections are equipped with longitudinal reinforcement (black) and equal stirrups reinforcement, resulting in an inner confined concrete (gray), and an outer un-confined concrete (red).	40
4.3	Material behaviour of Steel02 material with the stress-strain relation effected by R_0 and behaviour without isotropic hardening [65].	42

4.4	Material behaviour of Concrete02 material for the stress-strain relation and behaviour with and without tensile strength [13].	43
4.5	Static loads and masses structure represented as line- and nodal loads. Line loads p_i are given force where nodal loads M_i are given in mass. There are four load scenarios for each load type, i.e. $i = 1, 2, 3, 4$	45
4.6	Deformed structure due to gravity analysis.	47
4.7	The first three mode shapes for the RC frame structure. The mode shape are associated with the natural frequencies in Table 4.7.	48
4.8	Distribution of the selected ground motions, based on the characteristics of moment magnitude M_w , source-to-site distance, PGA, and mean period T_m [45].	52
4.9	Ground motions as a function of time, acceleration units is g.	53
4.10	Wavelet transform for ground motions. The horizontal lines referrs to the natural frequencies of the structure.	54
4.11	Response spectra for ground motions. The vertical lines represents the natural periods of the structure.	56
4.12	Hysteresis loops for the investigated frame structure. The area enveloped by the loops is an indication of the global energy dissipated.	60
4.13	Correlation between Global Energy and maximal peak inter-story drift, given 903 ground motion excitations.	62
4.14	Correlation between Global Energy and maximal inter-story drift in the range between 0 kNm and 6 kNm, given 903 ground motions.	63
4.15	Peak ground acceleration of GM compared with global energy.	64
4.16	Stiffness matrix evolution for GM 23 CHICHI-HWA033-N.	66
4.17	Stiffness matrix evolution for GM 41 CHICHI-TCU074-N.	67
5.1	C1.1: Non-optimized GP, prediction of CHICHI-TCU074-N, ID 41. Input and output nodes (a) - results and errors (b).	71
5.2	C1.2: Optimized GP, prediction of CHICHI-TCU074-N, ID 41. Input and output nodes (a) - results and errors (b).	72
5.3	Comparison of Kernel matrix for GP, prediction of CHICHI-TCU074-N, ID 41. With optimized parameters (a) - without optimized parameters (b) . .	73
5.4	C2.1: Optimized GP, prediction of CHICHI-TCU074-N, ID 41. Input and output nodes (a) - results and errors (b).	74
5.5	C2.2: Optimized GP, prediction of CHICHI-TCU074-N, ID 41. Input and output nodes (a) - results and errors (b).	75
5.6	C3.1: Optimized GP, prediction of CHICHI-TCU074-N, ID 41. Input and output nodes (a) - results and errors (b).	76
5.7	C4.1: Optimized GP, prediction of CHICHI-TCU074-N, ID 41. Input and output nodes (a) - results and errors (b).	78
5.8	C4.2: Optimized GP, prediction of CHICHI-TCU074-N, ID 41. Input and output nodes (a) - results and errors (b).	78
5.9	C4.1: Optimized GP, prediction of CHICHI-HWA033-N, ID 23. Input and output nodes (a) - results and errors (b).	79

5.10	The mean TRAC measure for the 296 output responses for each input/output node pair.	81
5.11	Mean TRAC values and distribution of error values from the 296 predictions of the 1st floor.	82
5.12	GP overall estimation: box plots of TRAC, SMSE and RMSE for Case 5 and Case 6. Input node: 23, output node: 42.	84
5.13	Comparison results Case 5 and Case 6 for the overall assessment of the GP. The predictions are seen for the responses associated with ground motion GM41 CHICHI-TCU074-N. The predictions were made in node 42 given the inputs from node 23.	85
5.14	Comparison results Case 5 and Case 6 for the overall assessment of the GP. The predictions are seen for the responses associated with ground motion GM23 CHICHI-HWA033-N. The predictions were made in node 42 given the inputs from node 23.	85
5.15	GP errors and TRAC value regarding the influence of the final structural state. The training and test sets used are listed in Table 5.15. The prediction were made for node 42 given the input for node 23.	90
6.1	NN overall estimation: Box-plots of TRAC, SMSE and RMSE for each of the 10 K-folds. The responses are related to the SAS load-set with the box-plot furthest to the right, including all the 301 predictions. Input node: 23, output node: 42.	95
6.2	NN predictions for responses corresponding to GMs CHICHI-TCU074-N (ID 041) and CHICHI-HWA033-N (ID 023) - Input node: 23, output node: 42.	96
6.3	NN, errors and TRAC value box-plots: influence of the final structural state. 4 cases - input node: 23, output node: 42.	99
6.4	Mean TRAC measure for each floor, given one node to be used as input that is used to predict responses on a different or the same floor.	101
6.5	Different noise levels added to a sine-wave with peak amplitude $A = 1$. The noise levels are related to; 5% of the STD of the signal, a white noise with STD of 5%, and a SNR of 25 dB.	104
6.6	Distributions of error for each fold, using the NN model to predict responses with various noise ratios SNR. Predictions of node 42 given input from node 23.	109
A.1	Frame structure and labeling of: (a) elements and (b) degrees of freedom.	125
A.2	Reference model for beams (a) and columns (b)	126
A.3	Deformed shape of a beam due to a unit displacement (a) or due to a unit rotation (b)	127
A.4	Deformed shape of the structure in case 1	128
B.1	Effectively Confined Core of Rectangular Stirrup Reinforcement [52].	134

B.2 Confined strength determination from lateral confining stresses for rectangular sections [52].	135
C.1 General cross section showing compression zone as well as strains in the section.	137
E.1 GM in the train set for preliminary study: ID 52.	141
E.2 GM in the train set for preliminary study: ID 86.	142
E.3 GM in the train set for preliminary study: ID 149.	142
E.4 GM in the train set for preliminary study: ID 182.	143
E.5 GM in the train set for preliminary study: ID 247.	143
E.6 C1.1: Non-optimized GP, prediction of CHICHI-HWA033-N, ID 23. Input and output nodes (a) - results and errors (b).	144
E.7 C1.2: Optimized GP, prediction of CHICHI-HWA033-N, ID 23. Input and output nodes (a) - results and errors (b).	144
E.8 Comparison of Kernel matrix for GP, prediction of CHICHI-HWA033-N, ID 23. With optimized parameters (a) - without optimized parameters (b)	145
E.9 C2.1: Optimized GP, prediction of CHICHI-HWA033-N, ID 23. Input and output nodes (a) - results and errors (b).	145
E.10 C2.2: Optimized GP, prediction of CHICHI-HWA033-N, ID 23. Input and output nodes (a) - results and errors (b).	146
E.11 C3.1: Optimized GP, prediction of CHICHI-HWA033-N, ID 23. Input and output nodes (a) - results and errors (b).	146
E.12 C4.1: Optimized GP, prediction of CHICHI-HWA033-N, ID 23. Input and output nodes (a) - results and errors (b).	147
E.13 C4.2: Optimized GP, prediction of CHICHI-HWA033-N, ID 23. Input and output nodes (a) - results and errors (b).	147
E.14 Comparison results Case 5 and Case 6 for the overall assessment of the GP. The predictions are seen for the responses associated with ground motion GM23 CHICHI-HWA033-N. The predictions were made in node 42 given the inputs from node 23.	148
F.1 The mean RMSE measure for the 296 output responses for each input/output node pair.	149
F.2 The mean SMSE measure for the 296 output responses for each input/output node pair.	150
F.3 The mean TRAC measure for the 296 output responses for each input/output node pair.	150
F.4 Mean error estimations for each floor from 296 predictions.	151
F.5 Distribution of error measure based on the 296 estimation of each floor. .	152

G.1	LDS (L in the figure) and NDS (NL in the figure) divided in 10 folds leading to the dataset introduced in Table G.1 and Table G.2. Composition of the train-set and test-set by sampling from LDS and NDS according to the considered case (Table 5.15).	156
H.1	Mean RMSE measure for each floor, given one node to be used as input that is used to predict responses on a different or the same floor.	157
H.2	Mean SMSE measure for each floor, given one node to be used as input that is used to predict responses on a different or the same floor.	158
H.3	Mean TRAC measure for each floor, given one node to be used as input that is used to predict responses on a different or the same floor.	158
H.4	Gaussian Process distribution of error measure based on the 281 estimation of each floor.	159
H.5	Neural Network distribution of error measure based on the 281 estimation of each floor.	160
I.1	Distributing of errors given each fold for the NN mode, with no noise. Predictions of node 42 given input from node 23.	161
I.2	Distributing of errors given each fold for the NN mode, with noise level 40 dB. Predictions of node 42 given input from node 23.	162
I.3	Distributing of errors given each fold for the NN mode, with noise level 30 dB. Predictions of node 42 given input from node 23.	162
I.4	Distributing of errors given each fold for the NN mode, with noise level 20 dB. Predictions of node 42 given input from node 23.	163
J.1	Gantt-Chart as estimated in the initial and revised project.	168

List of Tables

4.1	Modelling of structural elements, including element type in OpenSees, integration method, and geometric transformation.	39
4.2	Modelling of cross sections.	41
4.3	Material properties given for the steel material, modelled as a Steel02 material in OpenSees.	41
4.4	Material properties for concrete.	43
4.5	Dead-loads and live-loads applied to the structural elements. All values are in kN/m.	45
4.6	Line- and nodal loads for elements corresponding to Figure 4.5. Line loads are given in [kN/m], whereas nodal loads are given in $10^3 \cdot [\text{kg}]$	46
4.7	The first three natural frequencies and -periods of the RC frame structure. The natural frequencies are associated with the mode shapes in Figure 4.7.	48
4.8	Calibration of Rayleigh damping coefficients given a frequency range and a damping ratio of $\zeta = 0.03$. Utilizing Equation (3.16).	49
4.9	Earthquake events used in the study and relevant information. All events with load-factor = 1. Data retrieved from PEER-NGA Database [45, 9]. Minimum PGA = 0.1001 g from LOMAP, maximum PGA = 0.4964 g from MANJIL.	50
4.10	Ground motion IDs and associated load-factor. The linear and non-linear behaviour is based on a threshold of the global energy dissipation of 1.5 kNm.	58
4.11	Performance levels, corresponding damage state and maximal peak drift limits [31, 8].	61
4.12	Global dissipated energy and maximum inter-storey drift for GM23 and GM41.	61
5.1	Train set used in the preliminary study.	70
5.2	Case1: Settings of the simulations used to present the effects of the optimization.	71
5.3	Case 1: Input nodes and optimized variances for each node. C1.1 is not optimized, meaning the initial values are listed.	72
5.4	Case 2: Settings of the simulations used to present the effects of the optimization.	74
5.5	Case 2: Input nodes and optimized variances for each node.	75

5.6	Case 3: Settings of the simulations used to present the effects of the optimization.	76
5.7	Case 3: Input nodes and optimized variances for each node.	77
5.8	Case 4: Settings of the simulations used to present the effects of the optimization.	77
5.9	Error and TRAC values for GP predicting signal in node 32, given different input nodes. Response 041, GM CHICHI-TCU074-N	79
5.10	Error and TRAC values for GP predicting signal in node 32, given different input nodes. Response 023, GM CHICHI-HWA033-N	80
5.11	Training and testing sets used for the overall assessment in Case 5 and Case 6. Only the responses related to the initial 301 GMs in the SAS load-set are to be used.	83
5.12	Error and TRAC values for Case 5 and Case 6. The listed values refer to the prediction of the signals associated with CHICHI-TCU074-N and CHICHI-HWA033-N. Input node:23, output node:42	86
5.13	Specific selected GMs based on linear and non-linear behaviour. The linear subset is based on the LAS whereas the non-linear subset is based on the HAS. Both subsets are a total of including 198 GMs. In the table are listed the loaf-factor (LF) as well as the response type (RT). The RT is either linear (L) or non-linear (N).	88
5.14	Training and test sets that only includes accelerational responses related to the LDS and NDS. These sets are to be used with the GP.	88
5.15	Overview of the training and test sets used in the four cases for the GP predictions. The responses composing the sets are further based on the GMs in Table 5.14.	89
6.1	K-Fold validation results for NN: Testing errors and TRAC values for the predictions. The considered responses correspond to the 301 SAS GMs. For each fold, 90 % of the data has been used for training, where the remaining 10 % were used for predictions. The responses are estimated in node 42, given input responses for node 23.	94
6.2	Error and TRAC values for NN predicting signal in node 42, given input responses in nodes 23.	96
6.3	Training and test sets for the K=6 fold for the NN. The predicted responses then matches the ones predicted for the GP.	97
6.4	K-Fold validation for NN for different state of input/output. In total 198 responses are used, which are all preset in both the linear and nonlinear state. Predictions of node 42 given input from node 23. The case of linear inputs and non-linear output is then referred to as (LN).	98
6.5	Training and testing sets including responses based on the 301 GMs in the SAS.	101
6.6	Noise levels and Equivalent Gaussian Standard deviation (EGS). In accordance with Figure 6.5.	104

6.7	Noise ratios and EGS that are to be used for the further analysis, using the SNR to define noise.	105
6.8	Accelerometer characteristics and SNR obtained from their datasheets [5, 25, 2, 1].	106
6.9	K-Fold validation for NN with different SNRs. Predictions of responses in node 42 given input from node 23. A total of 903 responses have been utilized related to the GMs in the SAS, LAS, and HAS load-sets.	107
6.10	Relative change in mean error and standard deviation error between a given SNR and the case with no noise from Table 6.9. All values are given as a percentage.	108
A.1	Selection of Newmark parameters based on algorithm.	132
B.1	Material properties for concrete.	135
B.2	The formulations of the material properties for concrete.	136
C.1	Material properties for concrete.	138
G.1	Testing sets for each of the K=10 folds. The training set for each fold includes the remaining responses not used in the testing set. In total are this set composed of 198 responses in the linear and non-linear respectively. The presented responses associated with the LDA load-set, which are all categorized as linear and are all having a load-factor=0.5.	154
G.2	Testing sets for each of the K=10 folds. The training set for each fold includes the remaining responses not used in the testing set. In total are this set composed of 198 responses in the linear and non-linear respectively. The presented responses associated with the NDS load-set, which are all categorized as non-linear and are all having a load-factor=1.5.	155

Symbols

Symbol	Description
Abbreviations	
SHM	Structural Health Monitoring.
ML	Machine Learning.
NN	Neural Network.
ANN	Artificial Neural Network.
LSHM	Long Short Term Memory.
MLP	Multilayer Perceptron.
CNN	Convolutional Neural Network.
KNN	K-Nearest Neighbour.
FE	Finite Element.
FEA	Finite Element Analysis.
GP	Gaussian Process.
RC	Reinforced concrete.
GM	Ground Motion
EOM	Equation of motion.
DOF	Degree of freedom.
SDOF	Single degree of freedom.
MDOF	Multiple degree of freedom.
RMSE	Root Mean Square Error.
SMSE	Standardized Mean Square Error.
TRAC	Time Response Assurance Criterion.
MSE	Mean Square Error.
SAS	Standard amplitude load-set.
HAS	High amplitude load-set.
LAS	Low amplitude load-set.
LF	Load-factor.
RT	Response type.
L	Linear.
N	Non-linear.
LDS	Linear data-set.
NDS	Non-linear data-set.

STD	Standard deviation.
SNR	Signal Noise Ratio.

Defined in Chapter 2

x	Input from the Training set S .
y	Output from the Training set S .
x*	Input from the Test set T .
y*	Output from the Test set T .
\hat{y}	Predicted value.
Δt	Time-step.
$z_{k,i}$	Sub-vector in relation to sensor k and time instant i .
l	Length of sub-vector $z_{k,i}$.
s	Step-size of sub-vector $z_{k,i}$.
$m(\cdot)$	Mean function .
$k(\cdot, \cdot)$	Covariance-function.
K	Kernel-Matrix.
σ_k^2	Variance for the k_{SE} covariance-function.
τ_k	Length-scale for the k_{SE} covariance-function.
σ_ε^2	Variance related to noise.
μ^*	Mean prediction related to GP.
Σ^*	Covariance-matrix related to the prediction of the GP.
f_{lr}	Learning-rate in relation to NN.

Defined in Chapter 3

$x(t)$	Displacement or rotation.
m	Mass.
c	Damping coefficient.
k	Spring stiffness.
$p(t)$	External force.
$(\dot{\cdot})$	First derivative in relation to time.
$(\ddot{\cdot})$	Second derivative in relation to time.
ω	Angular natural frequency.
ζ	Damping ratio.
X	Amplitude.
ψ	Phase.
ω_d	Damped natural frequency.
x	Displacement vector.
M	Mass matrix.
C	Damping matrix.
K	Stiffness matrix.
$\mathbf{P}(t)$	Force vector.
0	Zero-vector or matrix.
$(\cdot)_i$	Index that identifies the i -th mode.
n	Total number of DOFs / modes for a MDOF system.

α	Rayleigh Damping coefficient related to damping by motion.
β	Rayleigh Damping coefficient related to damping by deformation.
σ	Stress.
ε	Strain.
E_0	Linear relation between stress and strain. Also known as Young's Modulus.

Defined in Chapter 4

h	Column height of 3.5 m.
L	Beam length of 5.5 m.
$(\cdot)_s$	Parameter related to steel.
$(\cdot)_c$	Parameter related to concrete.
γ_s	Unit weight.
f_y	Yield strength.
E_0	Initial Young's Modulus.
b	Strain-hardening ratio.
R_0, cR_1, cR_2	OpenSees transformation parameters for Steel02.
γ_c	Unit weight.
$\gamma_{c,s}$	Unit weight for reinforced concrete.
f_c	Compressive strength.
ε_{c0}	Strain at maximum strength.
E_0	Young's Modulus in linear regime.
f_{cu}	Crushing strength.
ε_{cu}	Strain at crushing strength.
λ	Crushing slope ratio.
f_t	Tensile strength.
$E_{t,s}$	Tension softening stiffness.
g	Gravitational constant, $g = 9.81 \text{ m/s}^2$.
ω_i	Angular natural frequency for mode i .
f_i	Natural frequency for mode i .
T_i	Natural period for mode i .
E_G	Global energy.
Δ_{\max}	Maximal peak inter-story-drift.

CHAPTER 1

Introduction

Structural Health Monitoring (SHM) is the discipline that, through the acquisition and analysis of data from a structure leads to the assessment of its current and future integrity, it is fundamental to adequately monitor any type of structure such as bridges, buildings, offshore platforms, and wind turbines since the failure of these structures can lead to economic losses and/or human casualties. The techniques used in the SHM may provide early warnings of potential structural damages that are essential in the prevention of catastrophic failures.

The procedures used in SHM may involve the application of sensors, visual inspection, ultrasonic testing or other non-destructive techniques. However, the utilization of sensors seems to be the most practical solution. For example, thinking of the network of infrastructures present in a country, both the number of constructions and their physical size represents a challenge for SHM. Visual inspections coupled with other on-site tests cannot provide continuous monitoring and they become disadvantageous when the time required for these operations is considered. Therefore, sensors are commonly used in SHM because they are relatively inexpensive, easy to install and allow continuous monitoring. As with most other SHM applications, the primary sensors used for infrastructure health monitoring are accelerometers, since through the recorded quantities, it is possible to detect changes in the response of the structure. Thus, damage [27].

In the most general terms, damage can be defined as changes introduced into a system that adversely affect its current or future performance. In the context of structural systems, damage occurs when their material and/or geometric properties change. More precisely, the structure abandons the linear regime and starts responding in the non-linear regime that is characterized by non-linear material behaviour with permanent plastic deformations. An indication of a structure characterized by a non-linear state is the reduction of the system's stiffness as well as the accrual of plastic deformations. According to the given definition, the identification of damage implies a comparison with an initial state which is assumed to be an undamaged state [27]. The state of a point in the structure at a specific time, is given and can be described through different quantities such as displacement, strain, acceleration, temperature, and humidity. Therefore, the definition of the structural state over time, due to various loads and environmental conditions, can involve the use of sensors,

such as accelerometers, strain gauges, and other types of transducers.

Both the budget allocated for monitoring and its targeted damage types represent two of the elements that lead to the definition of the sensor's number located in a structure. In the specific case of bridges, most studies consider less than 100 sensors but there are bridges that are monitored continuously by over 1000 sensors [27]. In order to make the monitoring practical with a cost-effective number of sensors, some studies focused on the definition for the optimized layout of sensors [48, 41, 64]. The current project aims to use Machine Learning (ML) to extend the state recorded from sensors placed in some nodes of the structure to other locations that have not been provided with a sensor. This brings a reduction in the costs of the SHM program tailored for a structure and allows the monitoring of points that are not accessible. For example, in the case of offshore platforms, the corrosive saltwater environment can adversely affect the sensors and their wiring systems, thus, the elements placed below the water-line cannot be monitored [27].

The number of studies that try to accomplish damage detection and SHM through ML methods is significant. Dang et al. in [18] compared different types of Neural Networks (NN) such as long short-term memory (LSTM), multilayer perceptron (MLP), 1D and 2D convolutional neural networks (1DCNN and 2DCNN). All these methods were applied in the estimation of the section reduction in those points where sensors were recording the acceleration. The study involved structures with sizes and complexity: 1D simply supported beam, 2D steel frame and a bridge. Two other studies presented by Dan et al. [17] and Hamidian et al. [37] aimed to assess the global damage in the considered structures. The former study investigates the utilization of a neural network for the classification of the global damage state of a steel frame and of a bridge in four different categories: undamaged, moderate, mild or severe damage. The inputs used for such prediction were the acceleration signals provided by sensors uniformly distributed on the entire structure.

In the latter study, the focus was to estimate the global damage categories for a three-story steel frame. The considered ML methods of K-nearest neighbours (KNN), artificial neural network (ANN), and support vector machine (SVM), were inputted with one acceleration signal for each floor. However, in this study, the raw signals were processed and transformed in correlation functions, and then into entropy which provided information about the complexity and irregularity in a signal.

These studies represent the most relevant examples of ML application in SHM that have been analyzed during the literature review. The overall review led to the conclusion that different types of ML methods can be used to predict various measures of the structural state. However, no clear indications were made in relation to which methods are able to predict the structural state better than others. This was due to the fact that different ML methods were given different inputs and were then put to predict various outputs. Some outputs were then directly linked to a damage state,

whereas others were indications of stiffness reductions at various locations. Therefore, the great flexibility that the ML methods can attain in terms of the provided outputs with respect to other methods must be highlighted. The majority of the studies used acceleration signals for the estimation and/or localization of damage. This is a clear indication of the importance that the accelerometers play in the field of SHM.

For the reasons previously introduced, the present project aims to define a ML model that allows the prediction of acceleration signals in those points of the structure where sensors are not present. More precisely, the considered structure is subjected to an earthquake ground motion and the acceleration response signals are recorded in a few locations using sensors. The information collected from the sensors is then used to estimate the acceleration history in another location. In order to provide accurate estimations the ML model needs to be exposed to an adequate number of responses. In order to generate the responses used by the ML method to learn the pattern that links the input signals with the output signals, a Finite Element (FE) model of the considered structure is produced. The structure taken into account for the project consists of a reinforced concrete (RC) frame with 3 stories and 3 bays while the set of ground motions includes 301 different recordings. The selection and the main characteristics of the ground motions have been described in [46, 45]. The RC frame has been modelled with non-linear material properties, thus making the structure able to undertake damage which level depends on the characteristics of the excitation provided by the acting motion. The model evaluation is based on the true response in the same location that the ML method is to predict. These responses then correspond to a structure that is either in the linear or non-linear regime. The ML models that are to be used in the project are a Gaussian Process (GP) and a Neural Network (NN).

The present project can represent a novelty in the branch of the studies that pursue the application of ML in SHM. To the best of the authors' knowledge, a study that assesses the use of ML to predict acceleration responses given the accelerometers' recordings has not yet been conducted. Moreover, most of the studies that have been consulted during the literature review do not seek the combination of ML with non-linear FE analysis. When acceleration time histories are considered in the literature, the data is usually provided by benchmark and real structures or generated through FE analyses. However, in the instances that make use of a FEM model, the structural elements are modelled with linear material and the damage is introduced by reducing the cross-section or removing a limited number of elements - e.g. bracing elements.

The software and programs used in the thesis, including the FE model as well as the general frameworks of both the GP and NN, are available through the GitHub repository: 'Nonlinear State Estimation via Machine Learning' [54].

CHAPTER 2

Methodology

The present project investigates the possible application of finite element analysis coupled with Machine Learning for the prediction of linear and non-linear states in a structure due to external loads. The information used for the estimation of the structural state is provided by accelerometers that are able to record the acceleration in the three different spatial dimensions. However, this report only focuses on a single type of 2D frame structure thus, only the horizontal accelerations are relevant for the specific case. In this regard, it must be specified that the conclusions presented in the entirety of the report, are valid only for this specific considered structure. Different conclusions may occur when looking at structures either with different geometry or materials.

2.1 Project Methodology

The goal of machine learning is to use past experience, in the form of collected data, to learn how to accomplish a task in such a way that this learned ability generalizes to future situations of the same type [40]. The task assigned to the machine learning models used in this project consists of the estimation of acceleration signals in one or more locations of a structure, given the data recorded from one or more sensors placed at an adequate distance. In the present project, the nodal responses (both predicted and recorded) correspond to excitations that are generated by earthquakes applied to the structure through recorded ground motions. In the following analyses, the responses refer only to the structural accelerational responses.

Therefore, the past experience used to train the model (learning or training phase), consists of a data-set that is a collection of observations.

Since for each of the considered ground motions a finite element analysis (FEA) is run, each observation of the training phase includes both the observed data \mathbf{x} that is, the acceleration signals recorded by the sensors, and the data \mathbf{y} corresponding to the acceleration signal in a different node where the predictions are to be made. Since the model has then been trained and 'learned' the pattern between input and output data, in the following phase - i.e. the testing phase - will the model be fed only with the records given by the sensors \mathbf{x}^* in order to then predict the signal $\hat{\mathbf{y}}$.

It is fundamental to highlight the importance that the data-set holds in the project

since any ML models would not exist without a data-set. Therefore, the first focus was the creation of a data-set including a wide range of observations with input recorded accelerations \mathbf{x} and correspondent output signal \mathbf{y} . In the first stage of the project, there were no limitations regarding the number of sensors or their position therefore, it was important to generate and save the acceleration signals for all the nodes corresponding to each different ground motion. In order to classify the responses as either; responses generated by a structure in an undamaged state - i.e. still in the linear regime -, or those corresponding to a damaged structure -i.e. in the nonlinear regime -, both the global dissipated energy and the maximum inter-storey drift correspondent to each ground motion have been defined. The initial number of seismic events was 301 but it has been increased to 903 by scaling the initial ground motions with scaling factors. The acceleration signals, together with the dissipated energy and the maximum inter-storey drift, have been obtained through FE simulations run in the software **OpenSees**. For each of the 903 loads, a simulation has been run and an ID has been associated with each of them. Therefore, each ID is linked to a ground motion, a load factor, several acceleration responses (for sensors and output nodes), a value of global dissipated energy, and a maximum inter-storey drift.

Once the data-set has been produced, the focus was moved towards the selection of machine learning methods. For the selection of the models, it is fundamental to observe that the problem previously outlined is defined as a supervised regression problem. It lies within supervised learning since in the training phase the model is fed with the input data and the corresponding true output. Therefore, the goal of this phase is to find the best settings of the model that minimize the difference between the predicted output $\hat{\mathbf{y}}$ and the true output \mathbf{y}^* .

The acceleration is indeed a continuous variable: if it can take values a and b , then it can also take any value between a and b . Two models that are adequate for a problem with such properties and have been considered are the Gaussian Process (GP) and the Neural Network (NN). The aim of both models is the same: to learn the unknown function, that relates the input with the output. Therefore, given the training data points defined as \mathbf{x} and \mathbf{y} the two models are fitting a function to the data. Both models have been implemented in **Python** scripts through the modules **GPy** and **PyTorch** designed for Gaussian Processes and Neural Networks, respectively.

2.2 Machine Learning Methodology

The ground motions are to be grouped into training and testing sets, where each set includes only the responses for given ground motions. For instance, a given training set S may include five responses related to the ground motion (GM) with the IDs $[0, 1, 2, 3, 4]$, whereas a test set T is composed of the responses related to the GMs with IDs $[5, 6, 7]$. All the responses associated with the ground motions $S = [0, 1, 2, 3, 4]$ are then in the training set, and the responses associated with the ground motions

$T = [5, 6, 7]$ are in the training set.

The sets are then used to train or test the ML models. The models are able to include multiple input nodes - i.e. sensors - but only one output node which is the node at which the response is predicted. For example, given the training- and testing set S and T from before, if there are three sensors placed at the nodes $R_i = [n_1, n_2, n_3]$, these are used as inputs while the node $R_o = [n_4]$ is used as output. This means that given the responses in the nodes R_i , the model predicts the response in node R_o . For the training set S , the responses for the input nodes R_i are then denoted as \mathbf{x} where the outputs are denoted as \mathbf{y} . Similarly for the testing set T are the responses used as inputs denoted \mathbf{x}^* where the true outputs are \mathbf{y}^* .

The problem has been introduced as supervised thus, in the training phase the model takes the input with the correspondent real output responses, i.e. \mathbf{x} and \mathbf{y} . In this way, it is possible to compare the predicted signal with the real signal and adjust the model settings - i.e. the model is learning. Then in the testing-phase the model is given the inputs reactions \mathbf{x}^* for the testing set T , in order to predict the output responses $\hat{\mathbf{y}}$. These predicted responses can then be compared with the true response output \mathbf{y}^* .

Note that the training- and testing-phases are using responses associated with different GMs. Meaning that the model predicts responses it has never encountered before in the training-phase.

2.2.1 Input and Output

Each of the ground motions applied as excitation to the structure has been recorded with different stations with time-steps Δt , either being equal to 0.005 s, 0.01 s, or 0.02 s. However, all the responses from the FEA have all been recorded with a time-step 0.02 s disregarding the time-step of the generating ground motion recording.

In the case of the training set $S = [0, 1, 2, 3, 4]$ where each response is measured with a time-step $\Delta t = 0.02$ s and all the five ground motions have a duration of 40 s, the total amount of data elements would be equal to $n = 10,000$ elements! In the following analyses, even larger data-sets are to be considered. These large number of data-elements may later cause a problem in relation to computational time, since especially the GP does not scale well in terms of training data. The total number of elements is then to be lowered, for faster computations. Especially the data-elements used in the training set are to be lowered.

A way to reduce the total number n , is to only include a certain amount of the data e.g. every second, third, or fourth data-point. This would leave out some of the data points from a given response. However, this solution allows the inclusion of a larger amount of different responses, therefore, of more diverse data than including all the

data points from a fewer number of responses. This reduction in the data-size may be done in such a way, that the information preserved is still adequate to sufficiently train the models.

The presented solution can be further optimized by grouping the input responses into sub-vectors that corresponds to a single output data-point. Let both $\mathbf{y} = [y_1, \dots, y_n]$ and $\mathbf{x}_k = [x_{k,1}, \dots, x_{k,n}]$ be signals corresponding to the same motion of length n , where $k = 1, \dots, p$ is the indexation of the sensors. For each input signal provided by the p sensors, the sub-vectors $z_{k,i}$ are defined and the underlying function f is sought such as:

$$y_i = f(\underbrace{z_{1,i}, \dots, z_{p,i}}_{\mathbf{w}_i}) \quad (2.1)$$

where the subscript i is the index of the predicted time-instance. The sub-vectors that provide the input for the prediction of y_i are defined as:

$$z_{k,i} = [x_{k,i}, x_{k,i-1}, \dots, x_{k,i-l+1}] \quad , \quad i \geq l \quad (2.2)$$

where l represents the length of the sub-vector. With the presented definitions, only the value y_i would be predicted. However, this prediction is based on sub-vectors that include the time instance i as well as the $l - 1$ previous time instances. The prediction is then based on time-instances from the past. An illustration of how the sub-vectors are created is seen in Figure 2.1.

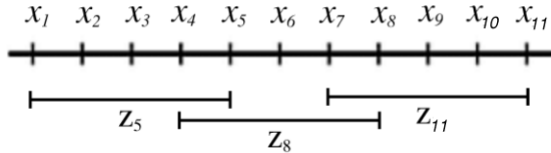


Figure 2.1: Visualization of sub-vectors z_i with length $l = 5$ and step-size $s = 3$.

In this case, the sub-vector z_5 would include the first five values and it would be used to determine only the one value y_5 . The sub-vectors then have a 'memory' of the past right before the predicted value. This further means that if a sub-vector has a length $l > 1$, the first $l - 1$ values are not able to be predicted since these have no associated sub-vectors. In the figure, the first value to be predicted is then y_5 followed by the predicted values y_8 and y_{11} , in fact, are only every third sub-vector shown, thus skipping z_6 and z_7 . This skipping of sub-vectors is introduced with the step-size s that indicates how many steps are skipped between two subsequent sub-vectors.

In the presented project the length of the sub-vectors l has been fixed to 25 while the stepping sizes s equal to 5 and 1 have been considered for the training and testing

phase respectively. This only leads to the exclusion of some data-points from the training phase with the aim of making the learning process faster. However, in the testing-phase all sub-vectors are to be included, such that the prediction includes all points, except for the first $l - 1$ values.

2.2.2 Evaluation of the output

The accuracy of the model in predicting the output signal in R_o is carried out by comparing the estimated signal $\hat{\mathbf{y}}$ with the true signal \mathbf{y}^* . In machine learning exist two different error measures which are based on the concept of training and test sets, namely:

- **Train error:** after the training phase, the model \mathcal{M}_s is inputted again with the training set and it estimates the output. Therefore, the training error is defined as:

$$E_{\mathcal{M}}^{\text{train}} = \frac{1}{N^{\text{train}}} \sum_{i \in \mathcal{D}^{\text{train}}} L(\mathbf{y}_i, f_{\mathcal{M}}(\mathbf{x}_i)) \quad (2.3)$$

- **Test error:** after the training phase, the model \mathcal{M}_s is inputted with the test set and it estimates the output. Therefore, the testing error is defined as:

$$E_{\mathcal{M}}^{\text{test}} = \frac{1}{N^{\text{test}}} \sum_{i \in \mathcal{D}^{\text{test}}} L(\mathbf{y}_i, f_{\mathcal{M}}(\mathbf{x}_i)) \quad (2.4)$$

The training error can give an entirely misleading picture of the model's performance because it is based on the estimation of the same signals that have been used for training the model. On the other hand, the testing error provides a reliable estimation of the model performance since it is evaluated upon data that the model has never seen before. Thus, it estimates how well the models generalize to new data.

In the previous equations, L stands for loss function that can be defined in several different ways. The loss functions used in this study are: Root Mean Square Error (RMSE), Standardised Mean Square Error (SMSE), and the Time Response Assurance Criterion (TRAC), which are defined in Equations (2.5), (2.6), and (2.7) respectively. The TRAC does not return an indication of error introduced in the estimated signal \mathbf{y}^* , instead, it indicates the correlation with the real signal.

The **RMSE** measure is commonly used in ML regression, which measures the standard deviation of the prediction errors, i.e. the residuals. The RMSE is then the spread of the residuals, with the same unit as the responses. A large RMSE is linked with deviations and thus a poor prediction, whereas a RMSE=0 is a prediction that is equal to the true response.

$$\text{RMSE}(\mathbf{y}, \hat{\mathbf{y}}) = \sqrt{\frac{1}{N} \sum_{i=1}^N (y_i - \hat{y}_i)^2} \quad (2.5)$$

The **SMSE** is closely related to the RMSE, in the sense that it is the ratio between the variance of the residuals ad the variance of the true response. The SMSE is then unit-less, with a value of 0 representing a predicted response equal to the actual response. A relatively large SMSE value then indicates a poor prediction.

$$\text{SMSE}(\mathbf{y}, \hat{\mathbf{y}}) = \frac{\frac{1}{N} \sum_{i=1}^N (y_i - \hat{y}_i)^2}{\text{var}(\mathbf{y})} \quad (2.6)$$

At last is the **TRAC**, which indicates how similar the shapes are between the two responses. This measure does not give an indication of amplitude and is unit-less. The value ranges between 0 and 1, where a value of TRAC=1 indicates that the two responses have the same shape [66].

$$\text{TRAC}(\mathbf{y}, \hat{\mathbf{y}}) = \frac{[\hat{\mathbf{y}}^\top \cdot \mathbf{y}]^2}{[\mathbf{y}^\top \cdot \mathbf{y}] \cdot [\hat{\mathbf{y}}^\top \cdot \hat{\mathbf{y}}]} \quad (2.7)$$

Each loss function is evaluated for each of the predicted signals. Since the number of signals involved in this study is 903, box-plots will be used to show the distribution of the errors over the entirety of the signals. The box-plots are generated using the **boxplot**-command in the Python module 'matplotlib.pyplot' [53], which shows the upper- and lower whiskers, the 25-th quartile (Q_1) and 75-th quartile (Q_3), the median (Q_2) as well as 'outliers'.

The difference between Q_3 and Q_1 is the inter-quartile range (IQR) such that $\text{ICR} = Q_3 - Q_1$. The upper- and lower whisker is defined such that they have a distance of 1.5IQR from Q_3 and Q_1 respectively. Note that in some cases the whiskers are not depicted with an equal length. This is due to the fact that the box-plot command extends the upper-whisker to the last datum less than the $Q_3 + 1.5\text{IQR}$. Where the lower-whisker is extended to the fist datum greater than $Q_1 - 1.5\text{IQR}$. This means that the whiskers seen are the largest datum within the range of the true whisker distance. It is then possible to have two depicted whiskers with a difference in length. If any datum is existing outside the range for the whiskers, these are indicated with circles mentioned as outliers.

2.3 The Gaussian Processes

One of the machine learning models evaluated during the presented project provides the application of a Gaussian Process (GP) to the regression problem. The interesting points about the employment of Gaussian Processes in regression problems can be summarized as:

- For a set of input/training points, there are an infinite number of functions that can fit these points. The Gaussian Processes are the extensions of the multivariate Gaussian distributions over random functions. Therefore, due to its capability of modelling arbitrary functions of the input points, the Gaussian process regression is a non-parametric model [20]. For the reported reasons, Gaussian Processes are able to assign a probability to each of the possible underlying functions. The probability distribution can be fully described through the mean value and the covariance function. The former represents the most probable characterization of the data while the latter incorporates insights about the confidence of the predictions [59].
- The distributions over functions can be used in the framework of Bayesian regression therefore, the Gaussian Processes are able to make predictions about data by incorporating prior knowledge [59].

2.3.1 Theory

The GP is a stochastic process such that any finite sub-collection of random variables has a multivariate Gaussian distribution¹. A collection of random variable $\{f(x) : x \in X\}$ is then said to be drawn from a Gaussian process with mean function $m(\cdot)$ and covariance function $k(\cdot, \cdot)$ if the elements $x_1, \dots, x_n \in X$ are associated with the random variables $f(x_1), \dots, f(x_n)$ described by the distribution:

$$\begin{bmatrix} f(x_1) \\ \vdots \\ f(x_n) \end{bmatrix} \sim \mathcal{N} \left(\begin{bmatrix} m(x_1) \\ \vdots \\ m(x_n) \end{bmatrix}, \begin{bmatrix} k(x_1, x_1) & \dots & k(x_1, x_n) \\ \vdots & \ddots & \vdots \\ k(x_n, x_1) & \dots & k(x_n, x_n) \end{bmatrix} \right) \quad (2.8)$$

which is described using the notation:

$$f(\cdot) \sim \mathcal{GP}(m(\cdot), k(\cdot, \cdot)) \quad (2.9)$$

The function $f(\cdot)$ can then be thought drawn from a Gaussian process prior as a high-dimensional vector drawn from a high-dimensional multivariate Gaussian distribution.

¹A stochastic process is simply a collection of random variables, which are indexed by elements in a given set X .

The mean function $m(\cdot)$ can in general be described by any real-valued function, whereas the covariance function $k(\cdot, \cdot)$, must be true that for any elements $x_1, \dots, x_n \in X$. The resulting matrix \mathbf{K} in Equation (2.10) is a valid covariance matrix corresponding to some multivariate Gaussian distribution.

$$\mathbf{K} = \begin{bmatrix} k(x_1, x_1) & \dots & k(x_1, x_n) \\ \vdots & \ddots & \vdots \\ k(x_n, x_1) & \dots & k(x_n, x_n) \end{bmatrix} \quad (2.10)$$

This is valid for kernel functions that can be used as covariance functions, which makes the GP a kernel-based probability distribution [20]. The kernel then determines which functions can be drawn from the correspondent GP. Thus, which functions are likely under the GP. To get an intuition for how the Kernel determines the shape of the sample functions is considered a simple GP with zero-mean:

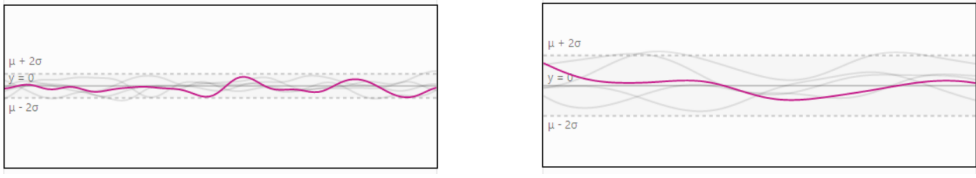
$$f(\cdot) \sim \mathcal{GP}(0, k(\cdot, \cdot)) \quad (2.11)$$

The kernel function $k(\cdot, \cdot)$ is chosen as one of the most commonly used functions, namely the Squared Exponential (SE) kernel function, also known as the Radial Basis Function (RBF) kernel function. The reason for the RBF kernels popularity is due to its properties of being universal and every function in its prior has infinitely many derivatives [22]. The SE kernel function is defined as ²:

$$k_{SE}(x, x') = \sigma^2 \cdot \exp\left(-\frac{1}{2 \cdot \tau^2} \|x - x'\|^2\right), \quad \tau^2 > 0 \quad (2.12)$$

with its two hyper-parameters σ^2 and τ being the variance and length-scale respectively. The variance determines the average distance of a given function away from its mean and it is usually found in front of every kernel - i.e. it's a scale factor. The length-scale determines the 'smoothness' of a given function, such that a larger length-scale results in smoother behaviour, whereas lower values yield more rapid amplitude changes in the functions. A graphical example of how the hyper-parameters affect the prior distribution is seen in Figure 2.2. Here it is seen that a larger variance, results in a larger amplitude of the sampled functions, as well as a larger length-scale results in a smoother function.

²Note that if two inputs are similar, the covariance will be high, i.e. $\|x - x'\| \approx 0$ results in $k_{SE} \approx 1$. Whereas for two vastly different inputs the covariance will be low, i.e. $\|x - x'\| \gg 0$ results in $k_{SE} \approx 0$.

(a) $\sigma^2 = 0.4, \tau = 0.5$.(b) $\sigma^2 = 1.0, \tau = 1.4$.**Figure 2.2:** Samples from zero-mean GP priors with k_{SE} as covariance function [34].

Other examples of kernel function may include the Linear Kernels and the Periodic Kernel, represented by linear or periodic functions respectively. The selection of the kernel functions is dependant on the behaviour of the data that is to be investigated since the kernel determines almost all the generalization properties of a GP model. Kernel composition, referring to adding or multiplying kernel functions together, may be utilized in order to obtain more complex functions to describe the behaviour of the data. The composition can be based on physical considerations or personal expertise [14].

2.3.2 Gaussian Process Regression

Since the Gaussian process is able to model probability distributions over functions, it is possible to use the GP in the framework of Bayesian regression. Let $S = \{(x_i, y_i)\}_{i=1}^n$ be a training set of independent variables distributed according to an unknown distribution. The GP regression model is then defined as:

$$y_i = f(x_i) + \varepsilon_i \quad , \quad i = 1, \dots, n \quad (2.13)$$

where the noise $\varepsilon \sim N(0, \sigma_\varepsilon^2)$ varies with a Gaussian distribution. Then consider a test set of points $T = \{(x_i^*, y_i^*)\}_{i=1}^{n^*}$ that is drawn from the same distribution as S . Let it be known that the two sets are assumed mutually exclusive, i.e. $S \cap T = \emptyset$. For the sake of notation simplicity are the following vectors are defined:

$$\begin{aligned} \mathbf{X} &= \begin{bmatrix} -x_1 - \\ \vdots \\ -x_n - \end{bmatrix} \in \mathbb{R}^{n \times d} & \mathbf{f} &= \begin{bmatrix} f(x_1) \\ \vdots \\ f(x_n) \end{bmatrix}, \quad \boldsymbol{\varepsilon} &= \begin{bmatrix} \varepsilon_1 \\ \vdots \\ \varepsilon_n \end{bmatrix}, \quad \mathbf{y} &= \begin{bmatrix} y_1 \\ \vdots \\ y_n \end{bmatrix} \in \mathbb{R}^n \\ \mathbf{X}^* &= \begin{bmatrix} -x_1^* - \\ \vdots \\ -x_n^* - \end{bmatrix} \in \mathbb{R}^{n^* \times d} & \mathbf{f}^* &= \begin{bmatrix} f(x_1^*) \\ \vdots \\ f(x_n^*) \end{bmatrix}, \quad \boldsymbol{\varepsilon}^* &= \begin{bmatrix} \varepsilon_1^* \\ \vdots \\ \varepsilon_n^* \end{bmatrix}, \quad \mathbf{y}^* &= \begin{bmatrix} y_1^* \\ \vdots \\ y_{n^*}^* \end{bmatrix} \in \mathbb{R}^{n^*} \end{aligned}$$

In order to define the prior distribution over functions $f(\cdot)$, a zero-mean Gaussian Process with a valid covariance function $k(\cdot, \cdot)$ is considered. Since the function $f(\cdot)$ is drawn from a zero-mean Gaussian process prior with a covariance function $k(\cdot, \cdot)$, the marginal distribution over any set of inputs is a joint multivariate Gaussian distribution [59]. This holds especially for the training and testing data, such that the joint distribution is defined as follows:

$$\begin{bmatrix} \mathbf{f} \\ \mathbf{f}^* \end{bmatrix} \mid \mathbf{X}, \mathbf{X}^* \sim \mathcal{N} \left(\mathbf{0}, \begin{bmatrix} \mathbf{K}(\mathbf{X}, \mathbf{X}) & \mathbf{K}(\mathbf{X}, \mathbf{X}^*) \\ \mathbf{K}(\mathbf{X}^*, \mathbf{X}) & \mathbf{K}(\mathbf{X}^*, \mathbf{X}^*) \end{bmatrix} \right) \quad (2.14)$$

The introduction of noise, which is also following a Gaussian distribution, is immediate since the sum of Gaussian distributions is also Gaussian. The formulation of the prior joint distribution then becomes:

$$\begin{bmatrix} \mathbf{y} \\ \mathbf{y}^* \end{bmatrix} \mid \mathbf{X}, \mathbf{X}^* \sim \mathcal{N} \left(\mathbf{0}, \begin{bmatrix} \mathbf{K}(\mathbf{X}, \mathbf{X}) + \sigma_\varepsilon^2 \mathbf{I} & \mathbf{K}(\mathbf{X}, \mathbf{X}^*) \\ \mathbf{K}(\mathbf{X}^*, \mathbf{X}) & \mathbf{K}(\mathbf{X}^*, \mathbf{X}^*) + \sigma_\varepsilon^2 \mathbf{I} \end{bmatrix} \right) \quad (2.15)$$

The essential idea of Bayesian inference is to update the current hypothesis according to the observed data. Therefore, a posterior distribution is defined by restricting the joint prior distribution over functions to include only those functions that agree with the training set S . In other words, this corresponds to the conditioning of the distribution defined in (2.15) on the observed data. Therefore, using the rule of conditioning for Gaussian distributions, it results in [20]:

$$\mathbf{y}^* | \mathbf{y}, \mathbf{X}, \mathbf{X}^* \sim \mathcal{N}(\boldsymbol{\mu}^*, \boldsymbol{\Sigma}^*) \quad (2.16)$$

with the predicted mean function $\boldsymbol{\mu}^*$ and covariance matrix $\boldsymbol{\Sigma}^*$ being determined as:

$$\begin{aligned} \boldsymbol{\mu}^* &= \mathbf{K}(\mathbf{X}^*, \mathbf{X}) [\mathbf{K}(\mathbf{X}, \mathbf{X}) + \sigma_\varepsilon^2 \mathbf{I}]^{-1} \mathbf{y} \\ \boldsymbol{\Sigma}^* &= \mathbf{K}(\mathbf{X}^*, \mathbf{X}^*) + \sigma_\varepsilon^2 \mathbf{I} - \mathbf{K}(\mathbf{X}^*, \mathbf{X}) [\mathbf{K}(\mathbf{X}, \mathbf{X}) + \sigma_\varepsilon^2 \mathbf{I}]^{-1} \mathbf{K}(\mathbf{X}, \mathbf{X}^*) \end{aligned} \quad (2.17)$$

From these parameters, the mean predicted values can be obtained as the elements in $\boldsymbol{\mu}^*$ and the variances for each prediction can be estimated from the diagonal of $\boldsymbol{\Sigma}^*$ [59, 20].

In Figure 2.3 is an example given of a GP regression, where $n = 10$ and $n = 20$ training inputs have been used in order to train the model, further is the 95% confidence region shown. As the number of training data increases the prediction becomes better. Note that the 95 % confidence range is smallest near the input values and increases in the areas without any training data.

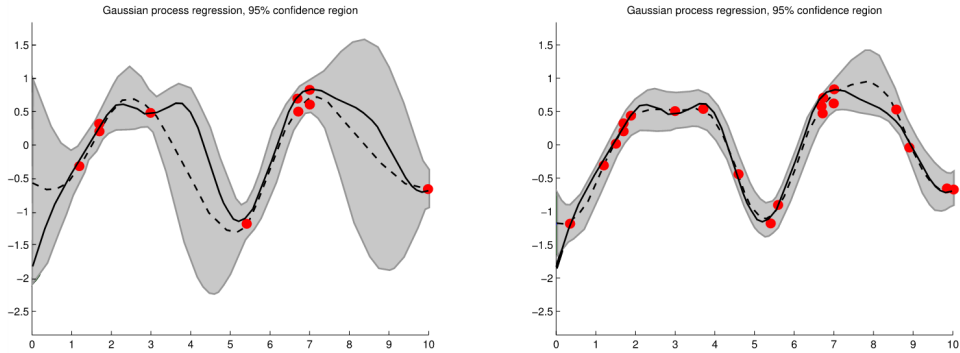


Figure 2.3: Gaussian process regression using zero-mean GP prior with k_{SE} as covariance function. With noise level $\sigma_\varepsilon^2 = 1$ and a) $n = 10$, and b) $n = 20$ training examples x_n indicated with dots. The true function is given in a solid line (—), whereas the prediction is given in a dashed line (- -). The 95 % confidence range based on the matrix Σ^* is shaded [20].

In general, the GP is more suited for relatively small data-sets, since the process uses the formulation of the inverse covariance matrix in order to make the prediction. The computational cost of training the GP model is then of complexity $\mathcal{O}(n^3)$ [58]. This complexity then results in the GP not being able to scale well in terms of training data, since the input data is scaled with an exponent of three.

Due to the introduced complexity of the GP the maximum number of responses used for training the model is restricted to 20 in the present project. Depending on the number of data-points in the training responses - i.e. the duration of the correspondent seismic event -, such limitation allows completing the training of the model without the occurrence of errors due to the drain of RAM memory.

However, the model uses the approach of determining a posterior using prior knowledge about the data, which provides well-calibrated uncertainty output such as the variance of the prediction. The GP further require an insight in the behaviour of the data in order to determine the kernel function to be used, which makes it possible for the user to understand more about the premise of the predictions.

2.3.3 Formulation of Kernel & Optimization

Since the model should be able to take multiple input-responses from different nodes, the kernel is to be composed as a sum-kernel with terms representing each input-node. The formulation of the sum-kernel used for the presented GP makes use of the definitions introduced for the k_{SE} kernel function and of the sub-vectors in Equation (2.12) and Equation (2.2), respectively. The sub-vectors provided by all the p sensors for a specific time-instant are stored in the vector \mathbf{w}_i given in Equation (2.1). Therefore,

considering two different time instants corresponding to the indices s and t , each element of the covariance matrix is a function of w_s and w_t . How a single component of the sum-kernel matrix is constructed in terms of the sub-vector inputs is given in Equation (2.18).

$$k(\mathbf{w}_s, \mathbf{w}_t) = \sum_{k=1}^p \sigma_k^2 \cdot \exp\left(-\frac{1}{2 \cdot \tau_k^2} \|z_{k,s} - z_{k,t}\|^2\right) \quad (2.18)$$

Note that the summation occurs over the sensors' index k . Initially, the distances between the sub-vectors provided by the same k sensor are computed taking into account also the correspondent factors σ_k and τ_k . The contribution from the different sensors is then summed over $k = 1, \dots, p$ thus, the Kernel can be seen as a matrix with p different layers that are combined. Each layer is a function of the information provided by one sensor. This means that each sensor $k = 1, \dots, p$ - i.e. input - is now associated with a set of parameters, namely σ_k^2 and τ_k representing the scale-factor and the length-scale. Thus, the global kernel matrix is a function of $2p$ hyper-parameters as well as the noise variance σ_ε^2 .

A scale-factor σ_k^2 equal to zero, indicates that the data recorded from sensor k is not relevant for the demanded prediction.

In order to model the GP the framework **GPy** is used in Python [35]. The framework allows for the creation of a sum-kernel as formulated in Equation (2.18). For the initialization of the GP are all hyper-parameters as well as error set equal to 1. GPy further provides a method to optimize the hyper-parameters, which makes it possible to optimize how the response of each input-node is weighted in relation to the output-node providing an indication of the most relevant input locations for the estimation process. The optimization process in GPy is done by maximizing the likelihood of the model [36].

2.4 Neural Networks

The second ML method used in the presented project is a Neural Network (NN), more precisely, a feedforward neural network. It represents a powerful approach for regression problems which allows for the prediction of the acceleration time histories for the considered structure.

Neural networks are a type of machine learning algorithm that is modelled after the structure and function of the human brain. The main element that defines a neural network is its architecture which consists of layers of interconnected 'neurons', that process and transmit information. These models are trained using a data-set, and by adjusting the strengths of the connections between neurons the NN is able to recognize patterns and make predictions.

The advantage of Neural Networks is their ability in working with large data-sets. For this reason, are they widely used in image and speech recognition, natural language processing, and many other applications. The reason for such ability can be found in the nature of these algorithms since they fall into the category of parametric models. The approach of this type of model consists of making assumptions about the functional form of the underlying function. In the specific case of Neural Networks, the functional form is defined by the architecture of the network.

This procedure allows the Neural Networks to explicitly build the underlying function during the training phase by adjusting the parameters that regulate the connections between the neurons. Thus, unlike the GP, they do compute a model before the prediction is required. The same is used for the entirety of future predictions. However, due to the singular defined function, the output of these models consists of the returned value without any additional information.

2.4.1 Theory & Architecture

It is possible to distinguish different types of neural networks because of the different ways to process the given input and the architecture. The most simple type of NNs is the feedforward neural network, where the given information flows through the network in only one direction, namely from the input to the output layer, without looping back. Therefore, the input is processed through the multiple layers of neurons and the output from one layer is used as input for the next layer [32]. The Figure 2.4 shows how the neurons of a simple NN that includes the input layer, one hidden layer and the output layer are connected: each neuron located either in the hidden layer or in the output layer is inputted with a combination of the output values provided from the units placed in the previous layer.

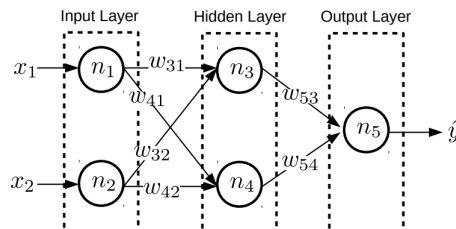


Figure 2.4: Example of a NN architecture with 1 hidden layer including 2 neurons [40].

Before being inputted into a given neuron, the previous outputs are multiplied by a weight w and are then added together along with the bias. In the context of neural networks, the *activation function* is the function that each neuron applies to the given

input. Given an input vector $\mathbf{x} = [x_1, x_2, \dots, x_M]^\top$ to the NN, the whole procedure can be described as follows [40]:

- The input to the NN is defined as:

$$\tilde{\mathbf{x}} = [1 \ x_1 \ x_2 \ \dots \ x_M]^\top$$

Each neuron i in the input layer returns the correspondent x_i component. In the previous equation, the first unit value represents the bias. It allows the neurons to adjust the input's net sum independently of the input and to shift the activation function to the left or right, changing the range of output values produced by the neuron.

- Neuron j in the hidden layer is given input $a_j^{(1)} = \tilde{\mathbf{x}}^\top \mathbf{w}_j^{(1)}$ that is just a real number. Each of the H hidden inputs are transformed using a nonlinear activation function h to give $z_j^{(1)} = h(a_j^{(1)})$. The output values can be collected in the vector:

$$\mathbf{z}^{(1)} = [z_1^{(1)} z_2^{(1)} \dots z_H^{(1)}]^\top$$

- Output neuron k is given an input of $a_k^{(2)} = (\tilde{\mathbf{z}}^{(1)})^\top \mathbf{w}_k^{(2)}$ that is transformed using a function $h^{(2)}$ to give $z_j^{(2)} = h^{(2)}(a_k^{(2)})$. The estimated value $\hat{\mathbf{y}}$ of the neural network (output) is:

$$\hat{\mathbf{y}} = \mathbf{f}(\mathbf{x}) = [z_1^{(2)} \ z_2^{(2)} \dots z_D^{(2)}]^\top$$

Therefore, if M is the number of neurons in the input layer and D is the number of output neurons, a Neural Network can be defined as a mapping:

$$\mathbf{f} : \mathbb{R}^M \rightarrow \mathbb{R}^D$$

which can be specified as

$$f_k(\mathbf{x}, \mathbf{w}) = h^{(2)} \left(\sum_{j=1}^H W_{kj}^{(2)} h^{(1)} \left(\tilde{\mathbf{x}}^\top \mathbf{w}_j^{(1)} \right) \right) \quad (2.19)$$

where

$$W^{(1)} = [\mathbf{w}_1^{(1)} \mathbf{w}_2^{(1)} \dots \mathbf{w}_H^{(1)}] \quad \text{and} \quad W^{(2)} = [\mathbf{w}_1^{(2)} \mathbf{w}_2^{(2)} \dots \mathbf{w}_D^{(2)}] \quad (2.20)$$

are the matrices that define the weight terms of the network. The weights and bias corresponding to each neuron make up the parameters of the considered network and they change as the network learns. The NN that has been introduced is a nice simple

example of a feedforward network since it includes only one hidden layer but it is sufficient to give a complete overview of the process. It is indeed the basis of many applications and it has been used for the prediction of ground time history responses by Derbal et al. [19]. Therefore, the architecture of the NN used in the present project is based on the NN presented in the cited study however, it is fundamental to specify the dimension and the activation functions of the layers. Most of the following definitions are due to the input and output structure defined in Section 2.2. Therefore, the architecture of the NN is outlined with the following information:

- The acceleration signals used in the NN are processed in the same way as in the Gaussian Process, described in Section 2.2: each signal is divided into sub-vectors of 25 elements (sample rate was fixed at 0.02s) with stepping size of 5 for the train set and 1 for the test set. Therefore, M is equal to 25.
- The hidden layer includes 20 neurons thus, the weight matrix $\mathbf{W}^{(1)}$ that multiplies the inputs of the hidden layer includes 20x25 elements. Moreover, the activation function $h^{(1)}$ used for the neurons in the hidden layer is a Rectified Linear Unit (ReLU) function defined as:

$$h^{(1)} : \text{ReLU}\left(\tilde{\mathbf{x}}^T \mathbf{w}_j^{(1)}\right) = \max \left[0, \tilde{\mathbf{x}}^T \mathbf{w}_j^{(1)} \right] \quad (2.21)$$

- The output of the NN corresponds to one point that is, the last acceleration value of each sub-vector. The activation function of each output neuron is a linear transformation that does not change the given input $(\tilde{\mathbf{z}}^{(1)})^T \mathbf{w}_k^{(2)}$. The second weight matrix $\mathbf{W}^{(2)}$ includes 20x1 elements.

2.4.2 Optimization

As previously mentioned the learning process of the NN consists of adjusting the weights that regulate the connections between the neurons. The change that must be introduced in the value of the parameters is evaluated through the estimation of the Mean Squared Error (MSE) for each predicted data-point. The MSE is defined as:

$$\text{MSE}(\mathbf{y}, \hat{\mathbf{y}}) = \frac{1}{N} \sum_{i=1}^N (y_i - \hat{y}_i)^2 \quad (2.22)$$

The optimization corresponds to the training phase therefore, it is performed by using only the train set. The procedure begins with the forward pass of the sub-vectors through the layers of the network which leads to a first estimation of the outputs for a batch of the training set. This leads to the definition of an error function that depends on the predicted value thus, on the weights (see Equation (2.19)). In order to optimize the algorithm the error function must be minimized. Therefore, the back-propagation and the descendent gradient algorithms are used to compute the gradient

of the error function with respect to the weights and to minimize it respectively [19]. More precisely, the gradient of the error is defined by the backward propagation of the error function that has been defined in the output layer, and then is propagated layer by layer moving towards the input layer. The described procedure is iterative and is regulated by some parameters that constitute the hyper-parameters of the NN. The NN and its optimization have been set in Python by using the module **PyTorch**. The hyper-parameters can be defined as follows [56]:

- **Number of Epochs:** the number of times to iterate over the whole data-set. The optimization is run n times over the same training data-set to minimize the error.
- **Batch Size:** the number of data samples propagated through the network before the parameters are updated - i.e. the number of sub-vectors upon the error function is built.
- **Learning Rate:** how much to update model parameters at each batch/epoch. Smaller values yield slow learning speed, while large values may result in unpredictable behaviour during training.

The selection of the described parameters can impact the convergence rates of the model towards lower error values affecting the computational cost of the operations. A brief study about the value of these hyper-parameters has been conducted. However, the optimization of the hyper-parameters has been neglected since the present report is intended to evaluate the possible utilization of NNs in the prediction of acceleration signals.

The final selected values are 30 Ephocs, batches including 25 sub-vectors and a learning rate equal to $f_{lr} = 4 \cdot 10^{-5}$. Apart from the maximum number of iterations (Ephocs), the training phase is stopped when the difference in the error between two adjacent iterations is lower than 1 %.

2.4.3 Over-fitting and cross-validation

The NN is not affected by limitations in terms of the size of the testing and training sets therefore, a deeper evaluation of the model has been carried out. The algorithm used for such evaluation is known as cross-validation and it is based on the definition of a new error. Apart from the training and testing errors introduced in Section 2.2.2, the generalized error is defined in the context of machine learning.

The evaluation of the training and test error is still relevant to assess if the model is over-fitting the data. The model might indeed start to memorize or capture random fluctuations in the training data rather than the underlying patterns. This would lead the model to perform well on the training data but to provide highly erroneous

predictions for not before seen test data. The over-fitting of the data can be identified by comparing the training and the testing data. An over-fitted model will indeed present a low training error but a high testing error. In neural networks, over-fitting is often related to the complexity of the model. A more complex model, such as a deep neural network with many layers and neurons, has the capacity to fit the noise in the training data.

This complexity of a neural network can be determined by several factors, such as the number of layers, the number of neurons in each layer, and the type of activation function used [33].

During the process of defining the architecture of the considered NN, some preliminary simulations were run varying both the number of neurons and other parameters such as the learning rate. In Figure 2.5 the training MSE and the testing MSE curves are reported for the NN with 20 hidden neurons and a fixed learning rate at the definitive final value of $f_{lr} = 4 \cdot 10^{-5}$.

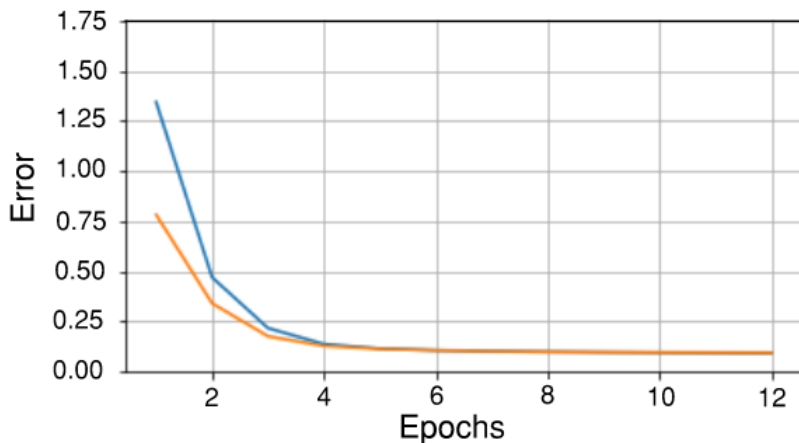


Figure 2.5: NN: — training MSE curve, — testing MSE curve. Simulation with 20 hidden-neurons and learning rate fixed at $f_{lr} = 4 \cdot 10^{-5}$. GMs: 301. Input: node 23. Output: node 42.

The model is not over-fitting the data since the training error in the final epochs is never sensible higher than the test error.

The generalized error is introduced also to solve the issue relative to the arbitrary choice of the test set. It is based on the assumption that the data amount is infinite. If one assume that the distribution $p(\mathbf{x}, \mathbf{y})$ of the test observations is known, then the generalized error is defined as [40]:

- Train the model \mathcal{M} on the full data-set available \mathcal{D} to give a prediction rule $f_{\mathcal{M}}$.
- The generalization error of model \mathcal{M} is:

$$\begin{aligned} E_{\mathcal{M}}^{\text{gen}} &= \mathbb{E}_{(\mathbf{x}, \mathbf{y})} [L(\mathbf{y}, f_{\mathcal{M}}(\mathbf{x}))] \\ &= \int L(\mathbf{y}, f_{\mathcal{M}}(\mathbf{x})) p(\mathbf{x}, \mathbf{y}) d\mathbf{x} d\mathbf{y} \end{aligned} \quad (2.23)$$

Therefore, the generalized error gives the best evaluation of the model since it is trained upon the whole data-set returning the average loss on all future data. It is clear that such a definition is not applicable since the real distribution of the test set is not known however, the cross-validation algorithm allows the estimation of the generalized error. In particular, in the present project, the K-fold cross-validation algorithm with 10 folds is considered.

The idea behind the method consists of including each observation - i.e. each signal - at least once in the test set. Therefore, in the 10-folds cross-validation algorithm, the first step is to split the entire data-set into 10 subsets:

$$\mathcal{D} = \mathcal{D}_1 \cup \mathcal{D}_2 \cup \dots \cup \mathcal{D}_k \cup \dots \cup \mathcal{D}_{10},$$

The following step is to run 10 different simulations: in each of these simulations, the test set changes and it corresponds to one of the \mathcal{D}_k sets while the remaining nine sets form the training set. In this way, the testing error is defined for each of the 10 subsets and each response. The last step is the estimation of the generalized error which corresponds to the weighted average of the test errors:

$$E_{\mathcal{M}}^{\text{gen}} \approx \sum_{k=1}^K \frac{N_k^{\text{test}}}{N} E_{\mathcal{M}, k}^{\text{test}} \quad (2.24)$$

where N_k^{test} is the number of observations in the \mathcal{D}_k test set while N is the total number of signals in the data-set.

CHAPTER 3

Structural Dynamics

Structural dynamics is a branch of engineering that deals with the analysis and/or design of structures subjected to dynamic loads¹, such as those caused by earthquakes, wind, or waves. It involves the study of the responses of structures to these dynamic loads and can include the design such that these structures are able to withstand or mitigate their effects. The discipline is an important area within structural engineering in order to ensure the safety and capabilities of modern infrastructure.

In structural dynamics, engineers use mathematical models to represent the behavior of structures under dynamic loads. These models may include equations of motion, which describe how the structure moves and deforms in response to the applied loads, as well as constitutive equations, which describe the material properties of the structure and how it deforms under load. The formulations of these equations of motion are to be described for both a single degree of freedom system, as well as the more general case of a multiple degree of freedom system.

To analyze the behavior of a structure under dynamic loads, engineers may use a variety of analytical techniques, including modal analysis, which involves identifying the natural frequencies and modes of vibration of the structure, and time-history analysis, which involves simulating the response of the structure to a specific dynamic load over time. These are all measures that will be used in order to get an understanding of the structure, and how it responds with different loads.

3.1 Degrees of Freedom

In terms of a mechanical system, the degrees of freedom (DOF) are the number of independent variables needed to define a system. These DOFs or parameters are, within the usage of structural engineering, represented by the displacement or rotation

¹The main difference between a dynamic load and a static load (which are used in structural statics) is the duration over time. Where static loads may have a slow and gradual application of force, dynamic loads are varying in intensity over time. This means the occurrence of non-zero velocity and acceleration, leading to internal damping- and inertia forces respectively, which are considered in dynamic problems. These parameters are negligible in static problems.

of the system. In this way, the DOF can either describe a translation in a straight line or a rotation around an axis.

3.1.1 Single degree of freedom

It is common to make the distinction between a single degree of freedom (SDOF) system and a multiple degrees of freedom (MDOF) system. Where the SDOF system is a simplified model that can move or vibrate in only one direction. This is due to the fact that the system is described by only one independent displacement or rotation. Note that both displacement, velocity and, acceleration can be used to describe the same SDOF system, since velocity and acceleration are derivatives of the same displacement. It is therefore, the same *single* independent variable that can be differentiated and/or integrated to get several quantities.

Examples of a SDOF system can be used to represent the motion of a simple pendulum or a mass-spring system, as seen in Figure 3.1.

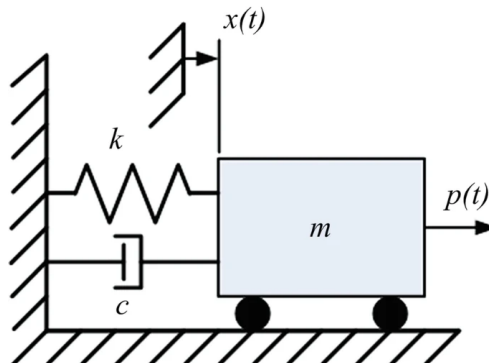


Figure 3.1: Schematic of an internal damped mass-spring, with a single degree of freedom [62].

This mass-spring system is composed of a mass m , a mass-less spring with stiffness k , and a mass-less dash-pot with a damping coefficient of c . The system is further experiencing an external force $p(t)$, and the SDOF system is described by the displacement $x(t)$.

The dash-pot is analogous to a viscous damper, that extracts energy from the system, and in this way, it dampens the system thus reducing the displacement. The damping coefficient is proportional to the viscosity of the liquid in the dash-pot. If no damper was included, i.e. $c = 0$, and the spring-mass system was then set in motion, the system would never stop vibrating since no energy would be extracted. By introducing an internal damping coefficient $c > 0$, energy is drawn out of the system, eventually

bringing the mass to a halt.

The behavior of the SDOF system can be associated with a differential equation which describes the motion of the system under the influence of the external force $p(t)$ and constraints of the system. This equation is also known as the equation of motion (EOM) of the system and can be derived using principles of classical mechanics, such as Newton's laws of motion. By the second law of motion, it is possible to establish an expression for the system in Figure 3.1 such that it is in equilibrium. This expression is the EOM for the system:

$$m\ddot{x}(t) + c\dot{x}(t) + kx(t) = p(t) \quad (3.1)$$

where $x(t)$, $\dot{x}(t)$, and $\ddot{x}(t)$ are the displacement, velocity and acceleration of the system respectively. The first term represents the inertial force of the system, the second term is the damping force, and the third term is the elastic (stiffness-related) force.

The equation of motion given by Equation (3.1), can be normalized by the mass in such a way that the equation is characterized by the natural frequency of the system ω , and the damping ratio ζ . This formulation is seen in Equation (3.2).

This new formulation of the EOM allows for non-dimensional parameters that are more generalized than the physical parameters. Especially the damping ratio ζ is a well-known parameter for several types of civil structures, with levels of magnitude that range between 0.01 and 0.05 [50, 51, 39].

$$\ddot{x}(t) + 2\zeta\omega\dot{x}(t) + \omega^2x(t) = \frac{1}{m} \cdot p(t) \quad \text{where} \quad \begin{cases} \omega^2 = \frac{k}{m} \\ \zeta = \frac{c}{2\sqrt{km}} \end{cases} \quad (3.2)$$

The natural frequency ω , is the frequency at which the system will vibrate when it is disturbed from its equilibrium position, i.e. resonate. The natural frequency is also known as the eigenfrequency. The damping ratio ζ is an indication of how damped the system is with respect to critical damping $c_{crit} = 2\sqrt{km}$. The damping ratio is split into three categories; under-damped $0 < \zeta < 1$, critically damped $\zeta = 1$, and over-damped $\zeta > 1$, where a higher damping ratio results in more damping of the system.

The three categories of damping can be seen in Figure 3.2.

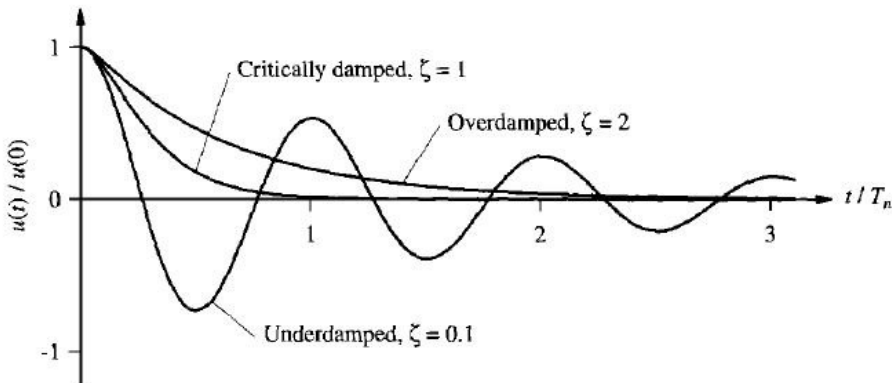


Figure 3.2: Free vibrations of under-damped, critically damped, and over-damped systems [63].

Most of the structures within civil engineering are described as under-damped, where the damping of an oscillator causes the structure to return to equilibrium with the amplitude gradually converging towards zero [4, 43].

Given that a system only has a single degree of freedom, only one natural frequency is associated with the system. A system of multiple degrees of freedom hence have more associated natural frequencies. In fact, the system will have as many natural frequencies as degrees of freedom.

3.1.2 Behaviours of the SDOF system

The single DOF systems can demonstrate a variety of behaviours, including free harmonic motion, free damped oscillation, and forced vibration [62]. Where the 'free' refers to the special case where no external force is applied to the system, i.e. $p(t) = 0$. The following behaviours are all based on the EOM of the SDOF system given by Equation (3.2).

In the case of a **free harmonic motion**, no external force nor damping is applied to the system, i.e. $p(t) = 0, \zeta = 0$. This means that the EOM reduces to only include the inertial force as well as the elastic force, with a right-hand side equal to zero. The solution, describing the displacement, to the EOM then becomes:

$$x(t) = x(0) \cos(\omega t) + \frac{\dot{x}(0)}{\omega} \sin(\omega t) \quad (3.3)$$

The displacement is seen to be harmonic with two terms including a cos and a sin term respectively, with the frequency being equal to the natural frequency of the

system. Since no damping is introduced, the system will oscillate indefinitely and never come to a halt. The solution can further be re-written in terms of amplitude X and phase ψ :

$$x(t) = X \cos(\omega t - \psi) \quad \text{where} \quad \begin{cases} X = \sqrt{x^2(0) + \left(\frac{\dot{x}(0)}{\omega}\right)^2} \\ \tan(\psi) = \frac{\dot{x}(0)}{x(0)\omega} \end{cases} \quad (3.4)$$

In the case of a **free damped oscillation**, the system will have no external force but there will be damping, i.e. $p(t) = 0, \zeta > 0$. Given that most civil structures are under-damped, i.e. $0 < \zeta < 1$ this is the solution of the EOM that is of most interest:

$$x(t) = e^{-\zeta\omega t} \left[x(0) \cos(\omega_d t) + \frac{\dot{x}(0) + \zeta\omega x(0)}{\omega_d} \sin(\omega_d t) \right] \quad , \quad \omega_d = \omega\sqrt{1 - \zeta^2} \quad (3.5)$$

where ω_d is the damped natural frequency, and relates the undamped natural frequency ω with the damping ratio. Further note if the damping ratio is equal to zero, the formulation of the displacement returns to the displacement of the undamped case seen in Equation (3.3).

The third case is the **forced vibration**, where an external force is applied to the system, i.e. $p(t) \neq 0$. Given this case, there is no explicit solution to the EOM, since the force $p(t)$ can be any function varying in time, amplitude, frequency, etc. However, a common solution to this, is to assume the load to be composed of impulses. Since the solution can be found with an external force taking the form of an impulse, this can be generalized with the use of Duhamel's integral [62]:

$$x(t) = \frac{1}{m\omega_d} \int_0^t p(\tau) e^{-\zeta\omega(t-\tau)} \sin[\omega_d(t-\tau)] d\tau \quad (3.6)$$

Overall, single DOF systems are simple mechanical systems that are useful for understanding the basic principles of structural dynamics and for modeling the behavior of more complex systems. However, if a system is to be made where more complex movement is possible, a MDOF system is needed.

3.1.3 Multiple degrees of freedom

Since a SDOF system does not truly exists in reality, often more complex models are needed in order to model more realistic systems which have multiple degrees of freedom. The principles are however similar to the SDOF system. Note that the MDOF system is still an approximation to reality since the assumption is that the system has a finite number of freedoms. In reality, a system will be composed of an infinite number of freedoms. However, simply including enough finite degrees of

freedom is often an acceptable approximation. Therefore the MDOF approach is a key tool for modelling complex systems.

Instead of having only one equation to describe the system as for the SDOF system, the MDOF system has multiple equations that describe the overall motion and the interaction between mass, damping, and stiffness for the different freedoms. A schematic of a multiple MDOF system with two degrees of freedom is seen in Figure 3.3.

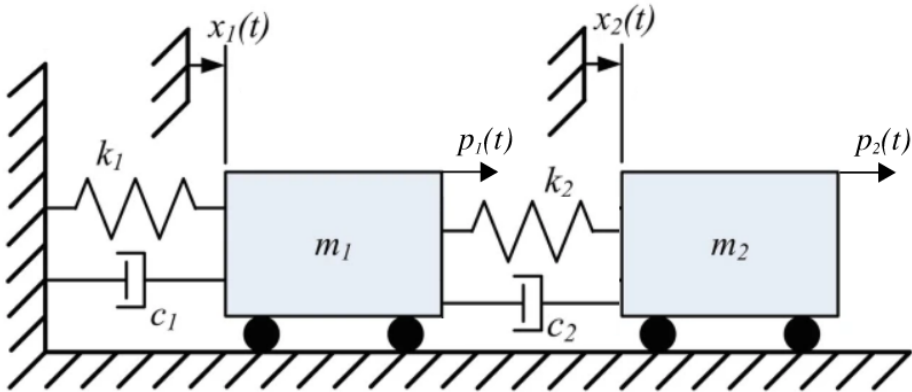


Figure 3.3: Schematic of a 2 degrees of freedom system [62].

This system is once again composed of masses $m_{1,2}$, springs with stiffness $k_{1,2}$, and damping coefficients $c_{1,2}$. However, instead of only one parameter of each, this system has one of these parameters per degree-of-freedom, which leads to a total number of two equations to describe this system:

$$\begin{aligned} m_1 \ddot{x}_1(t) + (c_1 + c_2) \dot{x}_1(t) - c_2 \dot{x}_2(t) + (k_1 + k_2)x_1(t) - k_2x_2(t) &= p_1(t) \\ m_2 \ddot{x}_2(t) - c_2 \dot{x}_1(t) + c_2 \dot{x}_2(t) - k_2x_1(t) + k_2x_2(t) &= p_2(t) \end{aligned} \quad (3.7)$$

This can easily be expressed using matrices and vectors:

$$\begin{bmatrix} m_1 & 0 \\ 0 & m_2 \end{bmatrix} \begin{bmatrix} \ddot{x}_1(t) \\ \ddot{x}_2(t) \end{bmatrix} + \begin{bmatrix} c_1 + c_2 & -c_2 \\ -c_2 & c_2 \end{bmatrix} \begin{bmatrix} \dot{x}_1(t) \\ \dot{x}_2(t) \end{bmatrix} + \begin{bmatrix} k_1 + k_2 & -k_2 \\ -k_2 & k_2 \end{bmatrix} \begin{bmatrix} x_1(t) \\ x_2(t) \end{bmatrix} = \begin{bmatrix} p_1(t) \\ p_2(t) \end{bmatrix} \quad (3.8)$$

In compact general notation, this EOM can be written as:

$$\mathbf{M}\ddot{\mathbf{x}}(t) + \mathbf{C}\dot{\mathbf{x}}(t) + \mathbf{K}\mathbf{x}(t) = \mathbf{P}(t) \quad , \quad \mathbf{x}(t)^\top = [x_1(t) \quad x_2(t) \quad \dots \quad x_n(t)] \quad (3.9)$$

were \mathbf{M} , \mathbf{C} , and \mathbf{K} are known as the mass-, damping-, and stiffness-matrix respectively, and $\mathbf{P}(t)$ is the force vector. In the general case, the system has n DOFs, whereas in the example $n = 2$. The general matrix formulation resembles that one defined for the SDOF systems from Equation (3.1), however, now formulated with matrices instead of scalars. Once more the first term represents the inertial forces applied to the system while the second and third term corresponds to the damping and elastic forces respectively.

Since the EOM is described with matrices and vectors, a different approach is needed in order to determine the natural frequencies and mode shapes for the MDOF system. This is done by investigating the free undamped response of the system i.e. $\mathbf{P}(t) = \mathbf{0}$, $\mathbf{C} = \mathbf{0}$, which leaves only the two terms related to the mass-, and stiffness-matrices:

$$\mathbf{M}\ddot{\mathbf{x}}(t) + \mathbf{K}\mathbf{x}(t) = \mathbf{0} \quad (3.10)$$

The solution for the free undamped response is known from the SDOF system, here written in terms of amplitude and phase:

$$\mathbf{x}(t) = \mathbf{X} \cos(\omega t - \psi) \quad (3.11)$$

Substituting Equation (3.11) into Equation (3.10) then gives the eigenvalue-problem:

$$(\mathbf{K} - \mathbf{M}\omega^2) \mathbf{X} = \mathbf{0} \quad (3.12)$$

Which only has non-trivial solutions if the determinant is equal to zero:

$$\det(\mathbf{K} - \omega^2 \mathbf{M}) = 0 \quad (3.13)$$

The roots of Equation (3.13) are the eigenvalues, which are the squared natural frequencies of the system. An eigenvalue ω_i^2 comes always with an associated eigenvector X_i which represents the mode-shape for the given mode i . Given an n -degree-of-freedom system, there will then be n sets of eigenfrequencies and associated mode-shapes.

3.2 Defining Matrices

In the previous section, examples of how to extract information regarding eigenfrequencies and mode-shapes from a general system with multiple DOFs have been seen. However, how the matrices are defined still needs to be understood. The method and principles are the same as described in the previous sections. Therefore, the definition of the matrices is based on specific degrees of freedom which correspond to the local DOFs for one element. These are the basic principles of Finite Element (FE) modelling, where *finite elements* are defined in order to create matrices. A finite element can correspond to an entire beam or be limited to a specific portion of the

beam. However, each of these defined elements can be associated, for example, with two local degrees of freedom at each end e.g. one translational motion and one rotational. An example of how a FE model is made and how the correspondent matrices are defined is further described in Appendix A.

The simplest matrices to retrieve are the mass- and stiffness-matrix, \mathbf{M} and \mathbf{K} . In case of the mass matrix, the components are the associated masses for a given DOF or element, which can be estimated given the geometry and density of a given element. A local mass-matrix can then be created, based on the each specific type of element. The same principle takes place for the stiffness-matrix. However, instead of masses the local stiffness are to be estimated. These are based on the geometry and shape of the element, as well as the elastic-stiffness which can be used to estimate parameters for the local stiffness matrix. These parameters may include the moment of inertia, cross-sectional area and Young's Modulus for a given material. Based on these local matrices and how the elements are oriented with respect to each other, the global matrices can then be created.

3.2.1 Damping Matrix & Rayleigh Damping

The damping matrix \mathbf{C} is, however, more complicated to create on a local element basis, even though this is still a possible solution. Instead, other approaches such as Rayleigh damping is often utilized since this method creates the damping-matrix based on damping ratios associated with the global structure. Since the damping ratios of specific structures are well-known in the literature and Structural Codes, this approach is widely used [16]. Rayleigh damping further utilizes the known mass- and stiffness-matrix to create the damping matrix as seen from Equation (3.14).

$$\mathbf{C} = \alpha\mathbf{M} + \beta\mathbf{K} \quad (3.14)$$

where the α -term represents damping by motion e.g. interaction with external factors such as wind, water, or soil, and the β -term represents damping by deformation e.g. internal factors such as yielding, damage, and friction. In this way, the damping matrix is constructed from the two known matrices of mass and stiffness.

By utilizing Rayleigh Damping, each mode i of the structure is being associated with a damping ratio ζ_i , such that each mode is analyzed as an independent SDOF system. These damping ratios for each mode are then determined using the two parameters α , and β as well as the associated natural frequency ω_i , for different modes:

$$\zeta_i = \frac{1}{2} \left(\frac{\alpha}{\omega_i} + \beta \omega_i \right), \quad i = 1, 2, \dots, n \quad (3.15)$$

The relation between the damping ratios and the associated natural frequencies is seen in Figure 3.4. Note that the natural frequencies and damping ratios are normalized.

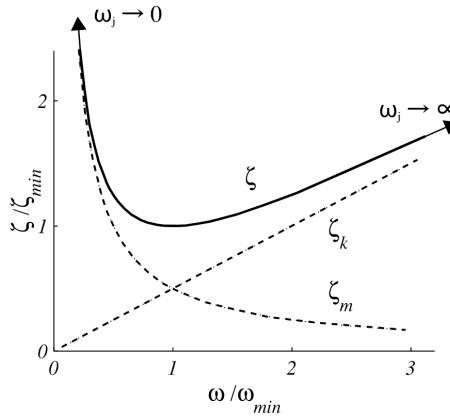


Figure 3.4: Rayleigh damping including components of α - and β -terms.

3.2.2 Calibration of Rayleigh Damping

As stated before, the damping ratio for a given structure is well known within the literature. It is then possible to determine the Rayleigh damping coefficients given a damping ratio and an associated eigenfrequency. In the case where two frequencies ω_i and ω_j are to have the same damping ratio such that $\zeta_i = \zeta_j = \zeta$. The coefficients are then to be estimated as:

$$\alpha = \frac{2\zeta\omega_i\omega_j}{\omega_i + \omega_j} \quad , \quad \beta = \frac{2\zeta}{\omega_i + \omega_j} \quad (3.16)$$

This formulation makes it possible to determine α and β for a given damping ratio ζ in a frequency range. The damping ratios outside the frequency range will increase, whereas the damping ratios inside the range will be lower than ζ , as can be seen in Figure 3.5(a). This method can further ensure that critical damping is avoided for relevant mode shapes.

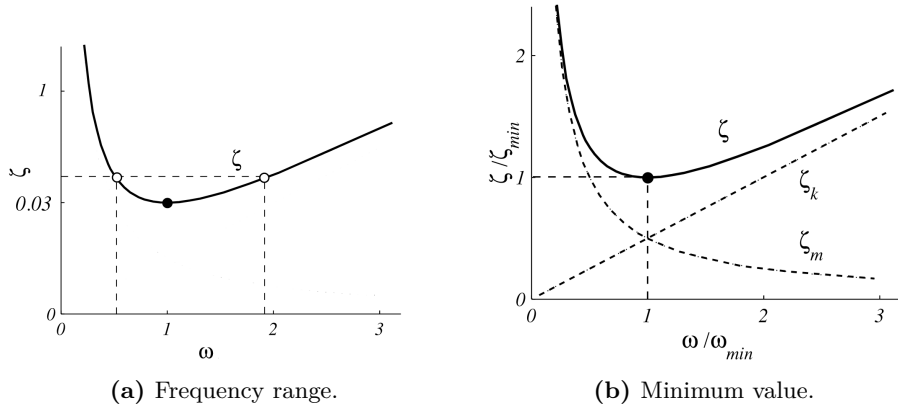


Figure 3.5: Damping ratio as a function of natural frequency using two methods of Rayleigh Damping.

Another method is where a minimum damping ratio ζ_{min} is to be associated with a given eigenfrequency ω_{min} , the damping coefficients are then estimated as:

$$\alpha = \zeta_{min}\omega_{min} \quad , \quad \beta = \frac{\zeta_{min}}{\omega_{min}} \quad (3.17)$$

This formulation insures a lower-bound damping ratio for a specific eigenfrequency, where all other eigenfrequencies are associated with a larger damping ratio, as can be seen in Figure 3.5(b).

3.3 Non-linearity

Until now, the parameters describing mass, damping, and stiffness have been constant and have not changed over time. However, in some cases, these parameters do vary over time due, for example, to changes in the material properties. To keep the analogy of elastic springs, the change could happen if the spring has been stretched to such an extent that permanent deformations occur, and the spring, therefore, does not return to its original state of deformation. This is a material property known as non-linearity, which occurs in structural materials such as concrete and steel. The case where the stiffness remains constant is known as linear.

In Figure 3.6 are the stress-strain curves for steel and concrete respectively.

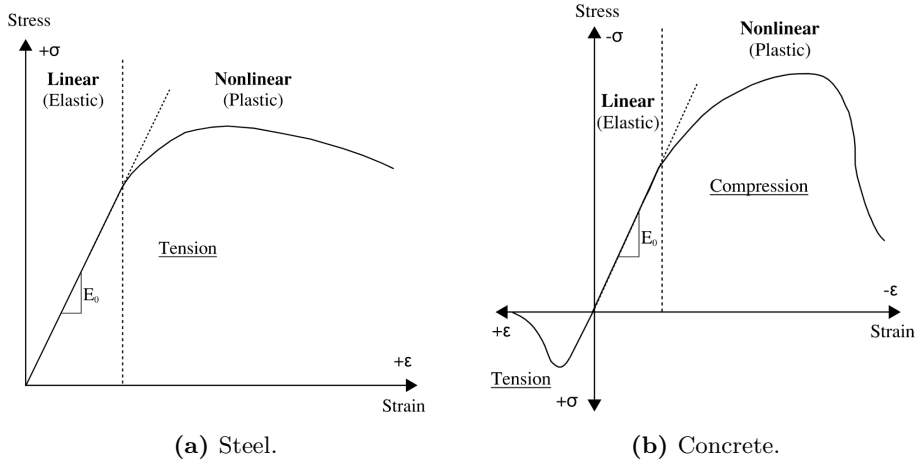


Figure 3.6: Strain-stress curves for a) steel and b) concrete.

It can be seen from Figure 3.6 that both materials have a phase where the stress-strain relationship is linear, this is known as the linear regime of the material. In this case, the relation between stress σ , and strain ε is given by a constant:

$$\underbrace{\sigma = E_0 \varepsilon}_{\text{Stress-Strain-Relation}} \quad (3.18)$$

where E_0 is the constant stiffness, namely known as Young's modulus, in the linear regime of the material. Equation (3.18) holds when the stress-strain² curves at a cross-sectional scale are considered. However, at a global scale, i.e. when considering the whole structure, the stiffness k relates to force and deformation, instead of stress and strain. It is possible to determine displacement and forces given strains and stresses thus, an analogous relation valid still in the linear regime, can be defined:

$$\underbrace{p = kx}_{\text{Force-Deformation-Relation}} \quad (3.19)$$

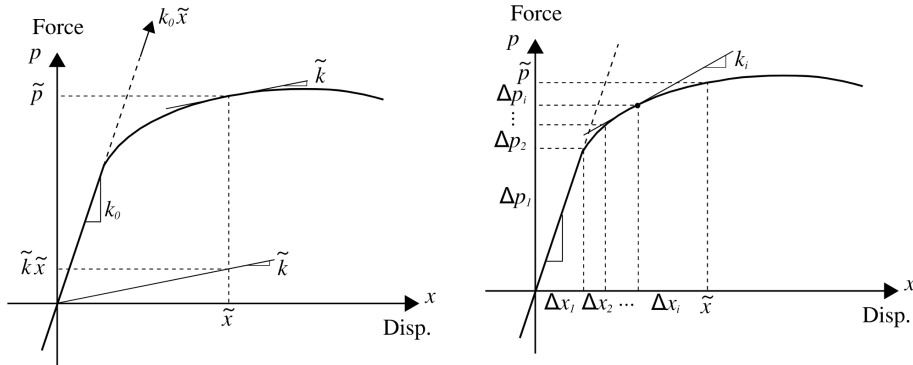
In the linear regime, no permanent strains or deformations occur, meaning that the material will return to its original deformations state once the stress or force has been removed. Deformations taking place in this regime therefore also referred to as elastic deformations.

The linear relation remains until the strains, or deformations exceed a limit. After this limit has been reached, the material is in the non-linear regime. Here permanent

²Stress, σ is the force applied to a specific cross-sectional area: $\sigma = p/A_0$, where strain ε is the change in deformation divided by the original length: $\varepsilon = \Delta L/L_0$.

strain/deformations occur, meaning that the material will not return to its original deformation state when the stress/force has been removed. Deformations in the non-linear regime are also referred to as plastic deformations. When in the non-linear regime, it is simply not sufficient to estimate the force-deformation relation as in Equation (3.19), since the relation is no longer linear. This means that the stiffness is now a function of deformation, i.e. $k(x)$.

In order to determine a stress or force in the non-linear regime, the method often used is instead to divide the curve into smaller sections in order to approach the curve, also known as the equilibrium path. The approach given for the deformation-force relation is seen graphically in Figure 3.7.



(a) Using only one stiffness-parameter.
Linear approach.

(b) Divide the curve into smaller sections.
Nonlinear approach.

Figure 3.7: Approaches to determine constitutive relation between force and deformation using a) linear approach and b) non-linear step approach.

Given a point (\tilde{x}, \tilde{p}) is to be determined in the non-linear regime. If only one linear stiffness relation is to be used the force estimated is not equal to the desired force \tilde{p} . This is true when using either the stiffness in the linear regime k_0 or the tangential stiffness \tilde{k} . Since when using these, the estimated force will either be over-estimated or under-estimated in relation to the desired force. This approach is seen in Figure 3.7(a), which states:

$$k_0\tilde{x} \neq \tilde{p} , \quad \tilde{k}\tilde{x} \neq \tilde{p}$$

However, as in Figure 3.7(b) if smaller steps are to be made including multiple tangential stiffnesses, an approximation to the desired force can be reached:

$$\tilde{p} = \sum_i \Delta p_i \simeq \sum_i k_i \Delta x_i \quad \text{since} \quad \Delta p_i \simeq k_i \Delta x_i$$

In this case one can reduce the steps, i.e. $\Delta x_i \rightarrow 0$, in order to change the sum to an integral such that: $\tilde{p} = \int k(x) dx$. This method is the bases of many commonly used iteration approaches such as the Newton-Raphson iteration, which utilizes iteration in order to minimize the error associated with the approximation.

This further states that the EOM for the non-linear case changes in relation to Equation (3.9), where the elastic force is defined as $\mathbf{Kx}(t)$. Instead the non-linear step-approach is implemented and formulated as:

$$\mathbf{M}\ddot{\mathbf{x}}(t) + \mathbf{C}\dot{\mathbf{x}}(t) + \int \mathbf{K}(\mathbf{x}(t)) d\mathbf{x} = \mathbf{P}(t) \quad , \quad \mathbf{x}(t)^\top = [x_1(t) \quad x_2(t) \quad \dots \quad x_i(t)] \quad (3.20)$$

where the integral represents the step-wise change in force. It is noted that the solution to the EOM in Equation (3.20) has to be done using direct integration, since the stiffness- and damping-matrices are not constant. A common method of direct integration is the Newmark integration scheme.

CHAPTER 4

Finite Element Model

In the following section, the structure used in the present project and its (FE) model are presented. **OpenSeesPy** has been used for the FE simulations, which is a Python interpreter of OpenSees and makes it possible to utilize the FE-program OpenSees within the framework of Python. OpenSees is a software framework for simulating the seismic response of structural and geotechnical systems [26]. The software has advanced capabilities for modelling and analyzing the nonlinear response of systems using a wide range of material models, elements, and solution algorithms.

4.1 Structure

The FE structure to be analysed is a two-dimensional reinforced concrete (RC) frame with three bays and three storeys. The semi-complex geometry of the system is to ensure that the responses are not too predictable, which could be the case for a two-bay two-story frame structure. Further, the semi-complex geometry makes the computational simulation and modelling relatively simple, by not choosing a more complex geometry or a three-dimensional structure. The general geometry, as well as element- and node-indications, is seen in Figure 4.1, with columns height $h = 3.5$ m and beams length $L = 5.5$ m. Note that the design of the structure and its elements has not been executed in accordance with any specific design code. The dimensions and material properties of the structural elements are chosen to such an extent, that they can represent realistic structural characteristics.

Since the model is in two dimensions, the structural elements will have three DOFs per node i.e. horizontal and vertical transnational DOFs as well as one rotational DOF for each of the two node-ends of the element. With a total of 21 elements, 12 columns and 9 beams, the structure has 16 nodes and 48 DOFs given three DOFs per node. The four nodes 10 to 13 are acting as fixed supports of the structure, which means that these nodes are not able to have any deformation nor rotation in any of their DOFs. This results in only 36 out of the 48 DOFs are free-DOFs since the remaining 12 DOFs are pre-determined due to the fixed supports.

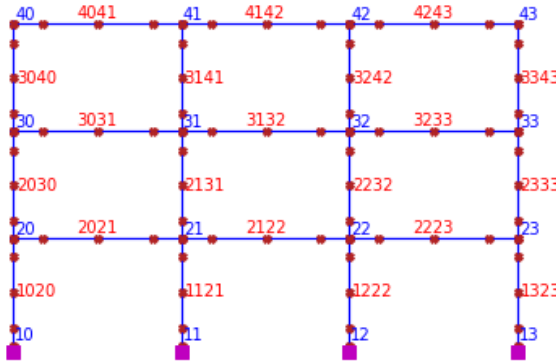


Figure 4.1: FE model of the RC frame structure. Column height of $h = 3.5$ m and beam length of $L = 5.5$ m. Nodes (in blue) are two digits located at intersections of structural elements, and elements (in red) are four digits composed of two node-ends.

The way OpenSees is able to model the structure is by structural elements which are defined mainly from the end-nodes and the *cross-section*. The latter can be composed of one or more materials. The structural element can for instance be a beam- or column-elements. The elements can be interpreted as a group that holds information about multiple sections. These sections are then defining the geometry of the element and are holding information about the materials that make up the given sections.

4.1.1 Elements

The elements considered in the present structure are made up of 9 beams and 12 columns, which are all modelled as **forceBeamColumn** elements in OpenSees. This element type is non-linear which is able to encompass distributed plasticity with a variety of integration methods [29].

The method of distributed plasticity makes it possible to obtain yielding at any given integration point along the length of the element. The most common integration method is the 'Gauss-Lobatto' integration. This is due to the fact that this method places integration points at each end of the element, where bending moments are the largest [60]. Other integration methods the element is capable of may include the Gauss-Legendre integration which is more accurate than the Gauss-Lobatto integration, but does not include integration points at the ends of the elements, and Newton-Cotes integration which places integration points uniformly along the element including the end-points. For the given structure the Gauss-Lobatto Integration is to be utilized with a total of five integration points along the length of each element, including one at each end of the element. The integration points are seen indicated

with red circles along the elements in Figure 4.1

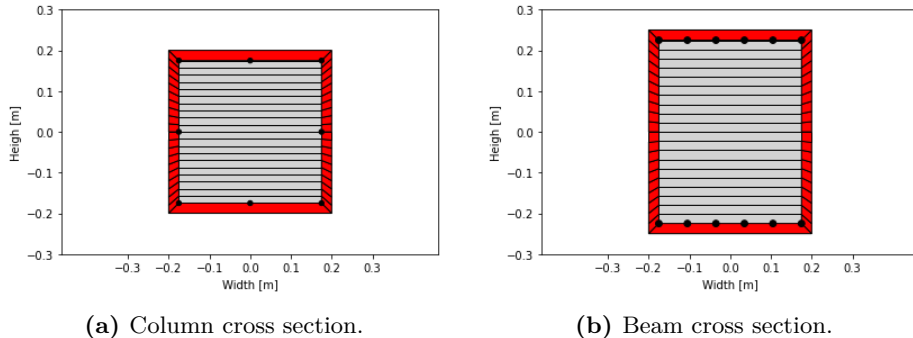
For the forceBeamColumn elements it is possible to specify the geometric transformation, which is used to transform the local elements' stiffness and forces to the global system, i.e. it transforms the local coordinates to global coordinates. Whether geometric non-linearities are considered, is dependent on the type of geometric transformation. OpenSees is using the three geometric transformations: linear, PDelta, and corotational, where the linear transformation does not account for any non-linearities. The PDelta transformation does only take the second-order effects associated with the lateral translation of the element into account, but not effects associated with the element curvature - i.e. the PDelta transformation includes $P-\Delta$ but not $P-\delta$ effects. The corotational transformation can be used in large-displacement-small-strain problems [30]. For the given structure the linear transformation is used for all beam elements whereas the PDelta transformation will be used for all column elements. A summary of how the structural elements are modelled in OpenSees is given in Table 4.1.

Table 4.1: Modelling of structural elements, including element type in OpenSees, integration method, and geometric transformation.

Structural element	Columns	Beams
Element type	forceBeamColumn	forceBeamColumn
Integration method	Gauss-Lobatto	Gauss-Lobatto
Number of int. points	5	5
Geometric trans.	PDelta	Linear
Length	3.5 m	5.5 m

4.1.2 Sections

Each of the two different types of elements - i.e. beams and columns - has its own cross-section and geometry. The cross-section of the column is double-symmetrical squares with eight longitudinal reinforcement bars, where the beams are symmetrical rectangles with 12 longitudinal reinforcement bars equally distributed at the top and bottom of the cross-section. The designed sections for both elements are seen in Figure 4.2.



(a) Column cross section.

(b) Beam cross section.

Figure 4.2: Cross sections for the structural elements. Both cross sections are equipped with longitudinal reinforcement (black) and equal stirrups reinforcement, resulting in an inner confined concrete (gray), and an outer un-confined concrete (red).

Both sections have stirrup reinforcement, which is not directly visible in the figure, due to them being placed in parallel with the sectional plane. However, the stirrups have an effect on the concrete which is either confined by the stirrups or un-confined in the cover layer. The two types of concrete are seen in Figure 4.2 as either the grey confined area of concrete or the red un-confined concrete cover. Since confined concrete has different material properties in relation to the un-confined concrete [52], the cross-section consists of three materials: longitudinal reinforcement steel, confined concrete, and un-confined concrete.

The sections are modelled as **FiberSection** in OpenSees, with each fiber being a **UniaxialMaterial** [28]. There are 22 fibers along the height of the sections, 20 along the confined concrete and one for each of the outer non-confined cover layers. Note that the cover of the side edges is represented with 22 fibers along their height. Since the model is two-dimensional, the width of the sections does not need subdivisions into fibers. The fibers are defined as quadratic polynomials, where the fiber-limits are seen in Figure 4.2 as horizontal lines. In Table 4.2 are a summary of the sectional properties for the two elements.

Table 4.2: Modelling of cross sections.

Structural element	Columns	Beams
Height [mm] x Width [mm]	400x400	500x400
Cover [mm]	25	25
Longitudinal reinforcement	8Ø16	12Ø16
Stirrups	Ø12/100	Ø12/100
Section type	Fiber	Fiber
Number of fibers (vertical)	22	22

4.1.3 Materials

Given the three materials in the sections - i.e. steel, and two concrete materials - these are to be defined before composing the sections. All materials are simulated as a **UniaxialMaterial**, which are objects that presents uni-axial stress-strain (or force-displacement) relationships [68]. The steel reinforcement is modelled as a **Steel02** material which is a uni-axial Giuffré-Menegotto-Pinto steel material object with isotropic strain hardening [65]. Whereas the two types of concrete are modelled as **Concrete02** materials, having linear tension softening [13].

4.1.3.1 Steel material

Since only one type of steel is used, the material properties can be estimated given common values for generic reinforcement steel. The chosen parameters are then listed in Table 4.3, given the material is modelled with no isotropic hardening.

Table 4.3: Material properties given for the steel material, modelled as a Steel02 material in OpenSees.

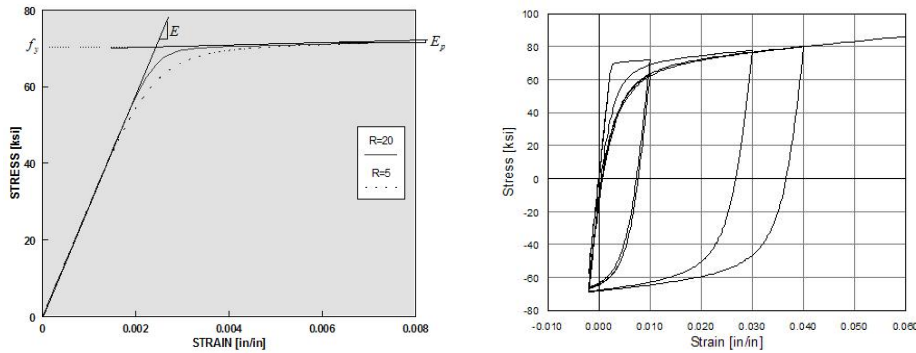
Material	Steel
Unit weight, γ_s	78.5 kN/m ³
Yield strength, f_y	410 MPa
Initial Young's Modulus, E_0	210 GPa
Strain-hardening ratio ¹ , b	0.02
R_0	18
cR_1	0.925
cR_2	0.15

where R_0 , cR_1 and cR_2 are parameters to control the transition from elastic to plastic branches. The recommended OpenSees values of these parameters are such that:

¹The strain-hardening ratio, b is the ratio between post-yield E_p tangent and initial elastic tangent E_0 such that $b = E_p/E_0$.

$10 \leq R_0 \leq 20$, $cR_1 = 0.925$ and $cR_2 = 0.15$.

In Figure 4.3 is seen the material relation between stress and strain and how the control parameter R_0 affects this relation, as well as the materials hysteretic behaviour given the material has no isotropic hardening.



(a) Material parameters of stress-strain relation.

(b) Hysteretic behavior of material without isotropic hardening.

Figure 4.3: Material behaviour of Steel02 material with the stress-strain relation effected by R_0 and behaviour without isotropic hardening [65].

4.1.3.2 Concrete Material

Given that two different concrete materials need to be defined, it is essential to state that the properties of the confined concrete are based on the parameters of the un-confined concrete. A summary of the material concrete parameters, for both the un-confined and confined case, are given in Table 4.4. The basis for the estimation of the confined material parameters is seen in Appendix B, where the un-confined and confined materials are assumed to follow a Todeschini Parabolic Model and a Mander Model respectively [7, 52].

Material properties given for the concrete materials both modelled as a Concrete02 in OpenSees.

Table 4.4: Material properties for concrete.

Material	Un-confined	Confined
Unit weight , γ_c	24 kN/m ³	24 kN/m ³
Unit weight (reinforced), $\gamma_{c,s}$	25 kN/m ³	25 kN/m ³
Compressive strength, f_c	20 MPa	29 MPa
Strain at maximum strength, ε_{c0}	0.30 %	0.44 %
Initial Young's Modulus, E_0	13 GPa	13 GPa
Crushing strength, f_{cu}	4.0 MPa	5.8 MPa
Strain at crushing strength, ε_{cu}	1.00 %	2.18 %
Crushing slope ratio ² , λ	0.1	0.1
Tensile strength, f_t	2.8 MPa	4.06 MPa
Tension softening stiffness ³ , $E_{t,s}$	1.4 GPa	1.4 GPa

In Figure 4.4 is seen the stress-strain relation of the Concrete02 material with corresponding stress-strain-pairs. Further is a comparison between the hysteretic behavior of the concrete material Concrete02.

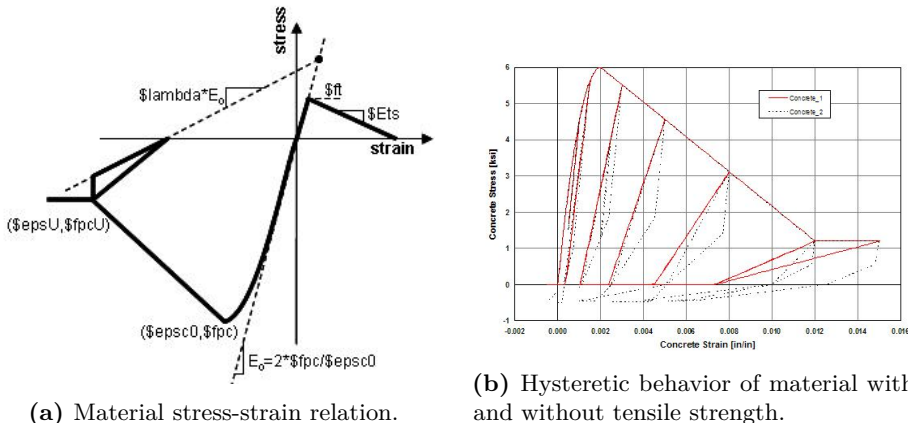


Figure 4.4: Material behaviour of Concrete02 material for the stress-strain relation and behaviour with and without tensile strength [13].

²The crushing slope ratio λ is the ratio between unloading slope at ε_{cu} and initial slope E_0 .

³The tension softening stiffness $E_{t,s}$ is the slope of the linear tension softening branch.

4.1.4 Balanced concrete sections

As mentioned earlier, the materials nor sections are designed after any design code, but the dimensions are such that the elements have structural characteristics that resemble a true structure. To this extent, the sections are to be investigated whether they are normal-reinforced.

In concrete design a reinforced concrete section can be within three categories: 1) over-reinforced, 2) normal/balanced-reinforced, and 3) under-reinforced, where the balanced case is preferred.

An over-reinforcement occurs when too much reinforcement is placed in the section, which leads to a compressive failure of the concrete before yielding takes place in the reinforcement. An under-reinforced concrete section is where too little reinforcement is placed, which leads to a tensile failure in the reinforcement before crushing in the concrete. A balanced section is where enough reinforcement has been placed in the section, leading to the crushing of the concrete at the same time as yielding in the reinforcement.

The calculations are given in Appendix C, from where it is shown that both sections are normal-reinforced with reinforcement degrees of $\omega_c = 7\%$ and $\omega_b = 11\%$ for the columns and beams respectively.

4.2 Preliminary analyses

From Section 4.1 the general model and its components have been described, including the topics of the overall structure's geometry, structural elements, cross sections and materials. Before the model is used for analysis, loads and masses are to be imposed on the structure. The model will then be used for both static and dynamic analysis. Specifically, in this preliminary study, the model will be used for two types of analysis: 1) a static gravity analysis, and 2) a modal analysis.

4.2.1 Static Loads & Masses

In reality, the structural elements have mass and thus impose a load on the entire structure, which is also known as dead-load. Other loads imposed on a structure do not come from the mass of the elements but are imposed by the expected objects in a given space, such as desks and people in an office space, or vehicles on a parking level. These loads are known as live-loads. Other loads may be caused by nature, such as wind-loads or snow-loads. These different types of loads can either be expressed in terms of mass or force since these two properties are coupled through the gravitational constant g . Given that the model will be used for both static and dynamic analyses, the forces and masses that are applied to the structure, are to be computed as both

evenly distributed line loads and lumped nodal loads. The representation of the four line loads p_i , and the four nodal loads M_i are seen in Figure 4.5.

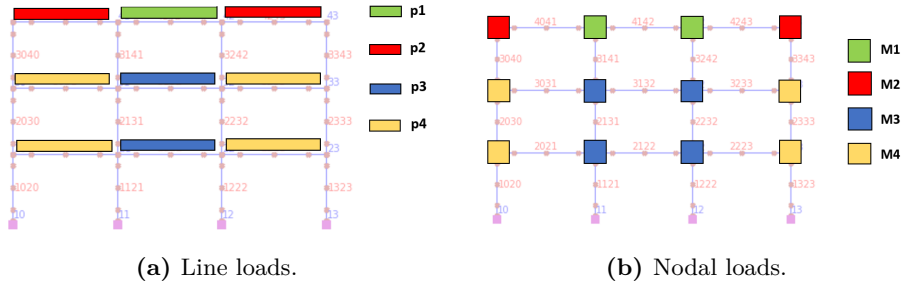


Figure 4.5: Static loads and masses structure represented as line- and nodal loads. Line loads p_i are given force where nodal loads M_i are given in mass. There are four load scenarios for each load type, i.e. $i = 1, 2, 3, 4$.

The line loads seen in Figure 4.5(a) are to be used for the preliminary static analysis, which is a gravity analysis. These line loads are given as forces and are composed of both imposed loads and masses that affect the structure. The forces are then distributed over the horizontal beam elements of the structure.

The nodal loads seen in Figure 4.5(b) are to be used for the dynamic analysis of the structure since this is the only allowable load input for the forceBeamColumn elements in OpenSees. These nodal loads contain the same forces and masses as the before mentioned line loads, however, where the nodal loads are given as masses.

The unit weight of reinforced concrete is given as 25 kN/m^3 cf. EN1992-1-1 §3.1 [12], and are listed in Table 4.4 along the remaining parameters for concrete. This together with the material properties for steel in Table 4.3, and geometry of the cross sections in Table 4.2, can be used to estimate the dead-loads of the elements per unit length. Further live-loads of 2.0 kN/m are applied only to the floor beams, with no snow- or wind-loads applied to the structure. The loads affecting the structure are summarized in Table 4.5.

Table 4.5: Dead-loads and live-loads applied to the structural elements. All values are in kN/m .

Structural element	Beams		Columns
	Roof	Other stories	All
Dead loads	5.0	5.0	4.0
Live load	-	2.0	-

For the beam elements, the dead-loads are added to the associated live loads. Further are the dead-loads of the columns split equally between the beams, in such a way that the loads p_1 and p_3 are distributed with the equivalence of one column, and the loads p_2 and p_4 are distributed with the equivalence of 1.5 columns. The nodal loads are estimated on the basis that the load on each beam is equally distributed between the two end-nodes. The horizontal influence length of loads M_1 and M_3 are therefore the full length of the beam, whereas the loads M_2 and M_4 are influenced by half the beam length. For both load estimations, the load of a column element is added to the upper node/connection of the column. The line- and nodal loads for all four cases are listed in Table 4.6.

Table 4.6: Line- and nodal loads for elements corresponding to Figure 4.5. Line loads are given in [kN/m], whereas nodal loads are given in $10^3 \cdot [\text{kg}]$.

Index, i	1	2	3	4
Line load, M_i	7.5	8.7	9.5	10.7
Nodal load, p_i	4.2	2.8	5.3	3.3

4.2.2 Gravity analysis

The gravity analysis is a static analysis, that utilizes the linear loads from Table 4.6, which are distributed over the horizontal beam elements of the structure. This analysis ensures that the structure is experiencing the gravity loads, such that initial deformations and forces are present in the structure. The analysis further returns the deformed shape of the structure after gravity has been applied, see Figure 4.6, which gives an indication of the interaction of the structural elements and if these are modelled to behave as intended.

The static gravity analysis is made with a linear time-series and a plain load pattern. The command **eleload** along with the **beamUniform** type applies the uniform loads to specific beam elements. How the analysis is created for static analysis, is further described in Appendix D.

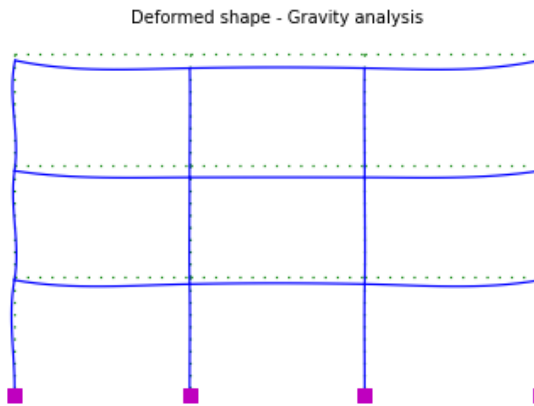


Figure 4.6: Deformed structure due to gravity analysis.

From Figure 4.6 it can be seen that the frame is having beam and column elements that are able to transfer moments in the frame-corners. This is based on the rotating corners, since all the connecting elements are rotating along with it. The frame structure does then behave as intended.

4.2.3 Eigenvalue Analysis & Applied Damping

After the gravity analysis is performed, the eigenfrequencies and mode shapes of the initial frame structure are determined with an eigenvalue analysis. The initial structure refers to the structure only with gravity loads, before any dynamic ground motions have been applied.

The eigenvalue analysis is based on the eigenvalue formulation from Equation (3.12), meaning that damping of the structure and external excitations are neglected, i.e. $\mathbf{C} = \mathbf{0}$, $\mathbf{P}(t) = \mathbf{0}$ [23]. By solving the eigenvalue problem both the mode shapes and the natural frequencies of the structure can be determined. These are seen and listed in Figure 4.7 and Table 4.7 respectively.

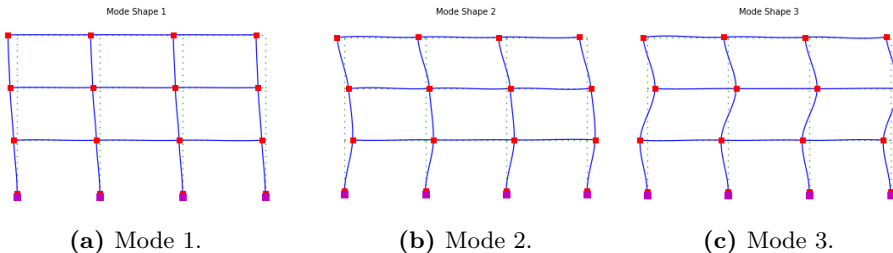


Figure 4.7: The first three mode shapes for the RC frame structure. The mode shape are associated with the natural frequencies in Table 4.7.

The mode shapes of the structure are typical shapes, that resemble the ones from a cantilever beam. It is further noticed, that the fixed supports of the structure behave as interned with no rotation.

Table 4.7: The first three natural frequencies and -periods of the RC frame structure. The natural frequencies are associated with the mode shapes in Figure 4.7.

Mode <i>i</i>	Ang. frequency, ω_i [rad/s]	Frequency, f_i [Hz]	Period, T_i [s]
1	17.0974	2.7211	0.3675
2	50.9920	8.1156	0.1232
3	79.8010	12.7007	0.0787

The natural frequencies ω_i are given in the unit [rad/s] and are also known as the angular frequency. Other representations may include the natural frequency f_i given in the unit [Hz] as well as the natural period T_i , which is given in the unit [s]. The relation between these formulations of natural frequencies and periods are given in Equation (4.1).

$$f_i = \frac{\omega_i}{2\pi} , \quad T_i = \frac{1}{f_i} \quad (4.1)$$

Once the natural frequencies are estimated, damping can be applied to the structure in the form of Rayleigh Damping. The damping is applied in such a way that the first and third modes are associated with a damping ratio of $\zeta = 0.03$. The damping matrix \mathbf{C} is then computed based on the damping associated with the entire structure, instead of the individual elements. The damping coefficients are then estimated using Equation (3.16), which are listed in Table 4.8.

Table 4.8: Calibration of Rayleigh damping coefficients given a frequency range and a damping ratio of $\zeta = 0.03$. Utilizing Equation (3.16).

Damping ratio ζ [–]	Eigenfrequencies		Damping coefficients	
	ω_1 [rad/s]	ω_3 [rad/s]	α [rad/s]	β [s/rad]
0.03	17.0974	79.8010	0.8448	0.0006

Given that these analyses are preliminary and performed before any transient analyses, which apply ground motions as loading, this is the initial state of the structure. To make sure that all the subsequent transient analyses are performed with the basis of the initial structure, the state is saved using the **database** and **save** commands in OpenSees. Before each transient analysis, this initial state of the structure is then loaded using the **restore** command.

4.3 Investigations of Dynamic loads

In the previous sections, the FE model has been defined and some preliminary analyses have been carried out, with the objective of defining the dynamic properties of the structure as well as verifying the overall functionality of the model. In the following section, the dynamic loads are to be selected and investigated to further understand how these might influence the structure. These dynamic loads will in turn be used as ground excitations on the structure, from where responses of the structure are obtained.

4.3.1 Dynamic Loads

To obtain responses for a given structure, external forces/loads must be applied to the structure. For the future states' prediction, a selection of 301 strong ground motions has been used as loads on the structure described in Section 4.1. The selection of ground motions has been carried out by E. Katsanos et al. [46, 45], where the number of recordings is to ensure a diverse representation of loads, including differences in: peak ground acceleration, duration, magnitude, and graphical location.

When selecting ground motions (GMs) to apply to a structure, it is common practice that these are selected based on either a site-specific hazard scenario or recorded ground motions. This selection is often based on standardized design codes, where the process of the selection is described. Given that this project aims to predict responses based on a different set of ground motions not related to a specific site-location, a broad selection of ground motion records with different characteristics is to be utilized. For this purpose, a selection of 301 seismic ground motion recordings has been formed based on the following rules [46]:

- The ground motions must include worldwide events, to avoid a dominance of recordings from specific areas with common seismotectonic features.
- The maximum number of recordings from the same earthquake event is limited to 15% of the total ensemble.
- The selection is based on a wide range variety within magnitude, peak ground acceleration, and soil profile.

The selection is summarized in Table 4.9, where the recordings were retrieved by the PEER-NGA Database [9].

Table 4.9: Earthquake events used in the study and relevant information. All events with load-factor = 1. Data retrieved from PEER-NGA Database [45, 9]. Minimum PGA = 0.1001 g from LOMAP, maximum PGA = 0.4964 g from MANJIL.

ID	Earthquake name	Number of recordings	Peak ground acceleration [g]	
			PGA _{min}	PGA _{max}
000	BIGBEAR	1	0.2253	-
001	BORREGO	1	0.1301	-
002-004	CAPEMEND	3	0.1140	0.3854
005-008	CHALFANT	4	0.1750	0.3997
009	CHICHI03	1	0.4732	-
010	CHICHI04	1	0.3229	-
011	CHICHI05	1	0.1039	-
012-015	CHICHI06	4	0.1292	0.4688
016-054	CHICHI	39	0.1175	0.4837
055-076	COALINGA	22	0.1121	0.4471
077	CORINTH	1	0.2960	-
078-081	COYOTELK	4	0.2109	0.4339
082-083	DUZCE	2	0.1066	0.2574
084	El Centro	1	0.1433	-
085	ERZIKAN	1	0.4955	-
086	FRIULI	1	0.3513	-
087-090	HECTOR	4	0.1017	0.3368
091-108	IMPVALL	18	0.1601	0.4798
109	KERN	1	0.1267	-
110-119	KOBE	10	0.1576	0.3148
120-128	KOCAELI	9	0.1080	0.3579
129-134	LANDERS	6	0.1094	0.2840
135	LIVERMOR	1	0.1545	-
136-177	LOMAP	42	0.1001	0.4810

(To be continued)

(Continued)

ID	Earthquake name	Number of recordings	Peak ground acceleration [g]	
			PGA _{min}	PGA _{max}
178-184	MAMMOTH	7	0.2188	0.4837
185	MANAGUA	1	0.4213	-
186-187	MANJIL	2	0.2087	0.4964
188-192	MORGAN	5	0.1943	0.3477
193	NCALIF	1	0.1892	-
194	NEWZEAL	1	0.2555	-
195-227	NORTHR	33	0.1393	0.4930
228	NWCHINA3	1	0.2737	-
229-230	PALMSPR	2	0.2182	0.4922
231-233	PARKF	3	0.2726	0.4416
234	SANSALV	1	0.4064	-
235-239	SFERN	5	0.1445	0.3658
240	SMADRE	1	0.4476	-
241-263	SMART1	23	0.1064	0.2423
264	SPITAK	1	0.1751	-
265-267	SUPERST	3	0.2072	0.2583
268-269	TABAS	2	0.1066	0.4061
270-271	TRINIDAD	2	0.1341	0.1561
272	VICT	1	0.1495	-
273-275	WESTMORL	3	0.1551	0.3682
276-300	WHITTIER	24	0.1509	0.4568
-	-	301	0.1001	0.4964

In the table is presented an ID which will be used as a reference both for the ground motion and all the correspondent acceleration responses throughout the report. Further is listed the name of the motion given by the PEER-NGA Database, the number of recordings for the given motion, as well as minimum and maximum peak ground acceleration (PGA).

The PGA is simply the maximal absolute value measured for a given recording. Therefore, it is related to the amplitude of the recording and, if not accompanied with at least a distance to the focus⁴, it does not give a direct insight for the severity or the magnitude of the earthquake. Some motions may be recorded from different locations of the earthquake, this makes it possible to have multiple recordings of the same earthquake. Note that these recordings may occur with different distances, which leads to differences in measured amplitude thus PGA.

⁴The focus is the underground location from where the ground motions originate.

Distributions of the selected ground motions are illustrated in Figure 4.8, in terms of characteristics such as moment magnitude, source-to-site distance, PGA, and mean period. From the distributions, it is noted that the characteristics of the selected motions are well-varied.

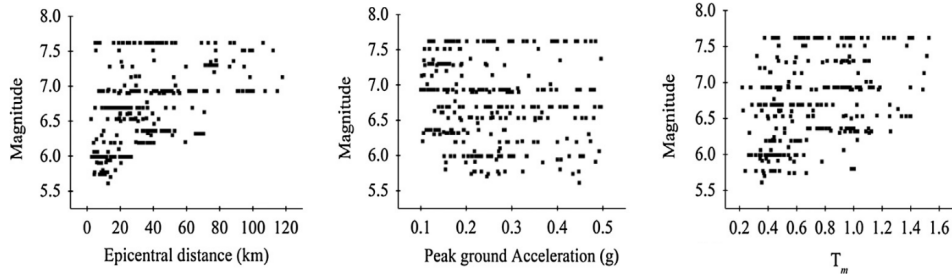


Figure 4.8: Distribution of the selected ground motions, based on the characteristics of moment magnitude M_w , source-to-site distance, PGA, and mean period T_m [45].

The moment magnitude scale M_w is a measure of the size of an earthquake. More commonly known is the Richter scale, which is also known as the local magnitude M_L . The moment magnitude is simply a more uniformly applicable scale measure of earthquakes [69]. The magnitude is then the characteristic value for a given earthquake, whereas the PGA can vary for the same earthquake measured at different locations.

The mean period T_m is derived by weighting the amplitudes over the specified range of the Fourier Amplitude Spectrum (FAS) [21]:

$$T_m = \frac{\sum_i C_i^2 \frac{1}{f_i}}{\sum_i C_i^2} , \quad 0.25 \text{ Hz} \leq f_i \leq 20 \text{ Hz} \text{ with } \Delta f \leq 0.05 \text{ Hz} \quad (4.2)$$

In Figure 4.9 are the ground motion recordings of CHICHI-HWA033-N and CHICHI-TCU074-N seen, with both motions having a duration of approximately 90 seconds. The corresponding IDs used for these ground motions are GM23 and GM41 respectively. Both figures are showing the ground motion as a function of time, and with values of acceleration given in g.

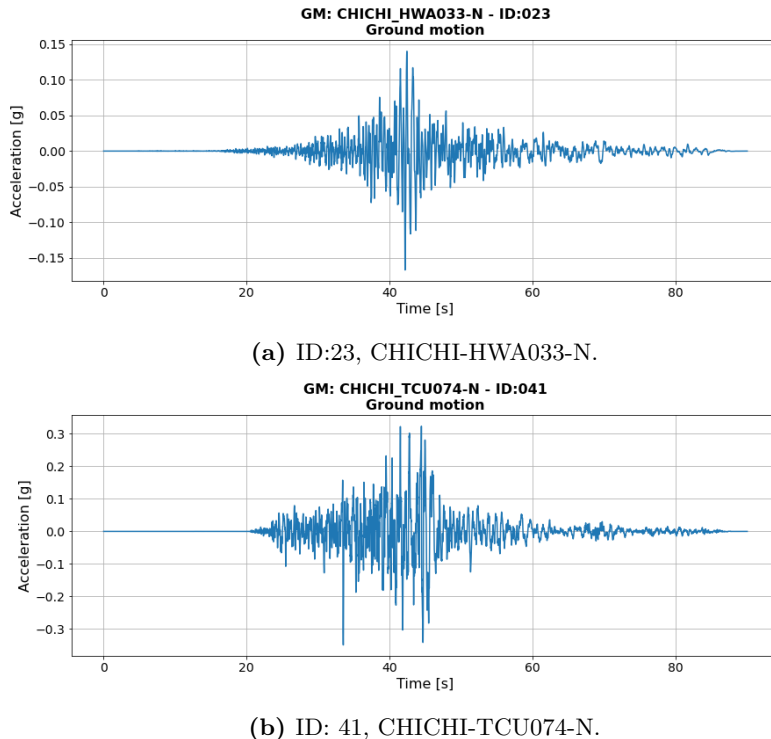


Figure 4.9: Ground motions as a function of time, acceleration units is g.

From the figures, it can be seen that the PGA, does not necessarily define the overall amplitude of the motion but only the largest absolute value measured. Given Figure 4.9(a) the overall amplitude of the measurement is below 0.05 g but with an intense impulse of over 0.15 g which is the PGA. However, for both recordings, the intensity increases and decreases over time, with a distinct section around $t = 40$ seconds, where the peak accelerations occur. Note that this behaviour of an increase and decrease in amplitude over time is somewhat general for ground motion recordings, even though these have a difference in duration, amplitude and when the peak occurs.

General investigations about the 301 ground motions are to be made, to get a further understanding of the characteristics of these ground recordings and how they might influence the structure. The remanding ground motions have been investigated in a similar manner.

4.3.1.1 Wavelet transform

Since the ground motions are dynamic excitations, these are composed of a variety of frequencies. The frequencies are of interest since the structure itself has natural frequencies, where the structure resonates. If an excitation has a frequency matching the natural frequency of the structure, this could result in large deformation and in the worse cases damage or collapse of the structure. In order to determine these frequencies the Fourier Transform could be applied to the motions, which transforms the motion into the frequency domain. However, this transformation only gives information about the dominating frequencies, but not when these frequencies occur. For this is wavelet transform used, to evaluate the frequencies as a function of time.

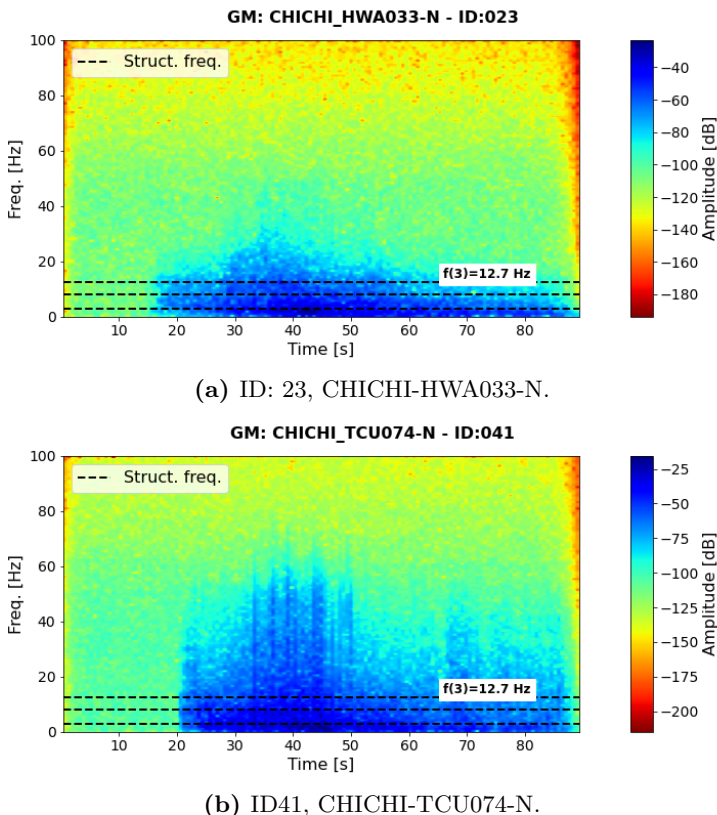


Figure 4.10: Wavelet transform for ground motions. The horizontal lines referrers to the natural frequencies of the structure.

The ground motions have then been evaluated with the wavelet transform from where it has been possible to identify which frequencies a specific ground motion is composed of as a function of time, and therefore throughout a seismic event. The wavelet trans-

form is further dependent on the time-step Δt that the recordings have been measured with, where the most common being $\Delta t = 0.02$, $\Delta t = 0.01$, or $\Delta t = 0.005$ seconds from using the PEE-NGA Database. This results in different ranges of frequency from where information about the ground motion can be obtained. The functions for the two ground motions GM23 and GM41 are seen in Figure 4.10. Both recordings were made with a time-step of $\Delta t = 0.005$ seconds, resulting in a frequency range of the wavelet transform from 0 Hz to 100 Hz.

In the figure, the horizontal dashed lines represent the natural frequencies of the structure listen in Table 4.7. It is seen that the highest frequency amplitudes of the ground motions are occurring near the time of the largest acceleration amplitudes from Figure 4.9, around $t = 40$ seconds. It is further seen that the frequencies do indeed change over time, meaning that the ground motions are composed of different frequencies at different times. Also, the frequencies of the ground motion overlap all three natural frequencies of the structure. This means that the ground motions may induce resonance in the structure. Especially the large frequency amplitudes of the ground motions are close to the lowest frequencies of the structure. Under such circumstances, if the frequency amplitude of the ground motion is extensive enough, the excitation will generate a response of the structure that is characterized by large accelerations and forces, which may lead to damage or collapse. The same analysis has been executed for the remanding ground motions from where the same tendencies are observed.

4.3.1.2 Response spectrum

In seismic engineering, the response spectrum is a commonly used method to investigate ground excitations. The response spectrum of a ground motion defines the corresponding peak response in terms of either acceleration, velocity, or displacement, for a series of possible SDOF systems with varying natural periods. It is further possible to factor the damping of these SDOF systems into the response spectrum [42]. Such analysis is useful since it includes information regarding both the ground motion and the structure showing the effect that the signal has on a specific structure and its natural period. In Figure 4.11 the response spectra for the two ground recordings CHICHI-HWA033-N and CHICHI-TCU074-N are shown, in the period range from 0 s to 4 s.

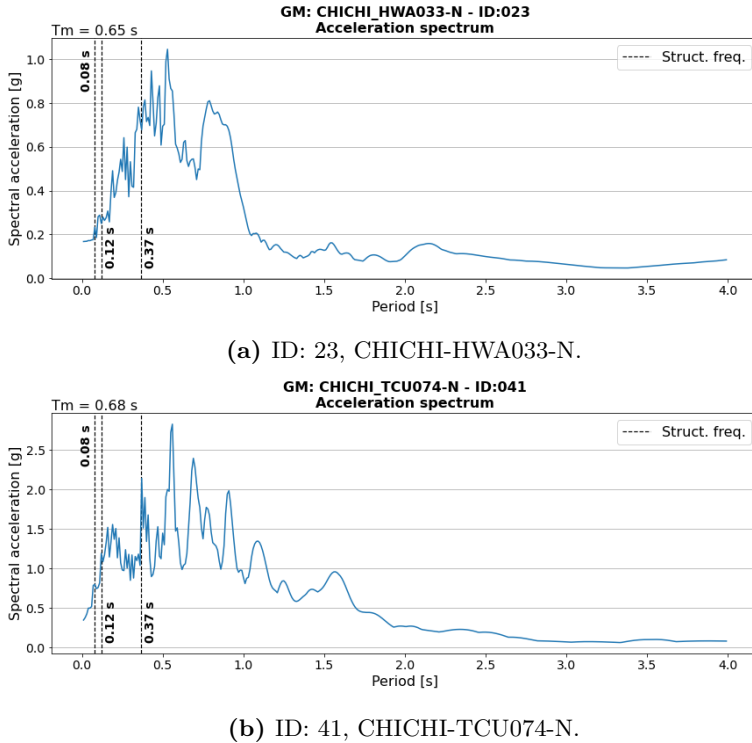


Figure 4.11: Response spectra for ground motions. The vertical lines represents the natural periods of the structure.

The response spectra show that both ground motions have a relatively high acceleration in correspondence with the first natural period of the structure. However, it must be highlighted that the ground motion GM23, has a lower overall spectral acceleration than GM41. For instance, for the first natural period of the structure of 0.37 s, the GM23 has a spectral acceleration of 0.8 g, whereas GM41 has a spectral acceleration of 2.1 g. Since the spectral acceleration is higher may GM41 excite the first mode of the structure more. Moreover, GM41 is having a significantly larger spectral acceleration for the period of 0.08 s, of approximately 1 g. This is the third natural period of the structure, meaning that GM41 is able to also influence the third mode of the structure, as well as the first two modes. GM23 is not able to excite the third motion to the same extent, given a spectral acceleration of 0.2 g associated with the third period of the structure. For these reasons it is expected that the consequences brought to the structure by GM41 will be more severe than those caused by GM23.

4.3.2 Dynamic Analysis

Now that the dynamic loads have been selected and investigated, these can be used as ground motion excitation in the FE model. Since the ground motions are time series, transient/dynamic analyses are to be carried out in OpenSees. Given these excitations, the associated responses of the structure can be obtained.

To excite the structure with a ground motion in OpenSees, the command **timeSeries** is used to specify that the excitation is a time series. The ground motion in the form of an acceleration time series is then loaded into OpenSees, along with a constant factor of $f_{LF} \cdot g$. Here f_{LF} is a load-factor which acts as a scaling parameter of the ground motions. The gravitational constant g is used in order to transform the accelerations into the unit of m/s². The time-step Δt for the ground motion recordings is further inputted into the **timeSeries** command. Considering the created acceleration series, the command **pattern** is used to create a load pattern 'UniformExcitation' which applies the load uniformly to the entire structure, acting in one direction. This means that all the fixed supports of the structure are experiencing the applied ground motion. OpenSees is capable of other patterns such as 'Plain' or 'MultipleSupport' excitations which are further described in Appendix D.

4.3.3 Extension of ground motion excitations

In the previous sections, the selection of the 301 GMs was justified in order to ensure a larger variety of the types of excitations used on the structure. One of the objectives of the thesis is further to evaluate the structure and its responses within both the linear and non-linear regimes - i.e. scenarios with an undamaged and a damaged structure respectively.

To ensure that analyses are to be carried out for an adequate number of both scenarios, the initial set of 301 GMs is then extended such that a total of 903 GMs are available as excitations. This extension is done using three different load-factors for each of the 301 initial GMs. In this way, one GM generates three load cases, one for each of the three load-factors being 1.0, 0.5, and 1.5. With a load-factor of 1.0, the original GM recording is used, however when using the factors of 0.5 and 1.5 the GM is scaled with these parameters respectively. A scaling of 0.5 then returns a lower amplitude whereas a scaling of 1.5 returns a larger amplitude. The frequency content of the three excitations is then the same, where only the amplitude changes. However, even though only the scaling is affected, the responses may be different for the three excitations, since the scaling may influence whether the structure is within the linear or non-linear regime. In Table 4.10 the GM IDs for each of the three load-factor sets are listed, where the initial set with load-factor equal to 1 are having the IDs from 000 to 300.

Table 4.10: Ground motion IDs and associated load-factor. The linear and non-linear behaviour is based on a threshold of the global energy dissipation of 1.5 kNm.

Loads-sets	GM IDs	Load factor	Linear	Non-linear
Standard-amplitude (SAS)	000 - 300	1.0	77	224
Low-amplitude (LAS)	301 - 601	0.5	222	79
High-amplitude (HAS)	602 - 902	1.5	26	275
000 - 902			325	578

The table further describes how many ground excitations result in the structure being associated with linear or non-linear behaviour. This is based on a threshold of 1.5 kNm of global dissipated energy, which is to be explained in the following section.

4.3.4 Model Outputs

Now that the FE model has been established and the excitations selected, the structural responses can be obtained for each of the ground motions. These responses of the structure can be a wide variety of measures, such as the moment or curvature in each section in an integration point or acceleration and velocity time series obtained in the structural nodes. The main purpose of these dynamic analyses is to obtain both the measures that quantify either the structural state and the acceleration responses of the structure, related to each ground motion. The state measures are specifically used to quantify if the structure is damaged and to which extent as well as to determine if the entire structural response is in the linear or non-linear regime.

4.3.4.1 Structural response

The response of the structure will be in the form of acceleration time histories, which are to be recorded at each free node of the structure shown in Figure 4.1. These recorded response accelerations will later be used as both training and test sets for the machine-learning models. These recordings are made using the **recorder** command in OpenSees. In this command is it specified that the recordings are of all nodes in the structure, all in the same direction. Further is all acceleration recordings done with the time increment of $\Delta t_{\text{rec}} = 0.02$ seconds.

The acceleration responses are recorded as absolute acceleration signals. In comparison the responses could be recorded in terms of the relative responses, meaning the response relative to the ground. The absolute response is then measuring the accelerations as a real accelerometer would and does therefore mimic that the recordings come from a measurement on a real structure and not a FE simulation. In reality, a machine learning model would be given real response measurement, from where the predictions are to be made. The investigations in this thesis, are then to resemble a

real application case from where the methods are investigated.

4.3.4.2 Quantities for state estimation

For the quantities used to estimate the state of the structure, during or after a seismic event, many can be used to estimate various damage measures. These damage measures are then trying to quantify to which extent the structure has experienced damage. For the later state estimations, the global dissipated energy is used, alongside the maximal inter-story drift. These parameters are then to be obtained from the FE simulations.

In Section 4.1.3 the strain-stress curves have been shown for the materials of steel and concrete, from where it can be determined if the material is behaving linearly or non-linearly. Further, it was discussed that when a material is within the non-linear regime permanent strains have occurred in the material which could be an indication of damage. The same non-linear behaviour can further be extended from a material scale to a sectional or even a structural scale.

In the case of a section, the behaviour is governed by the relation between the moment and curvature. And in the case of the structure, the behaviour is governed by forces and displacements. For a frame structure, it is common to use the total base shear force and the roof displacement for such relation [44]. For a specific dynamic analysis of a structure, these relations can be generated by using measurements recorded during the entire analysis. When the yielding point has been reached and the behaviour is non-linear, so-called hysteresis loops can be seen when plotting the functions associated with such relations. These loops are then enclosing an area equal to the amount of energy that the section or structure has dissipated.

In the linear case, the area would be equal to zero, since no permanent deformations have occurred. This means that the energy can be used as an indication of the structure behaving in either the linear or non-linear regime. In Figure 4.12 the behaviour between the total base shear and the roof-displacement is shown for GM23 and GM41 respectively. Here it is seen that GM41 has larger loops, which indicates more energy has been dissipated.

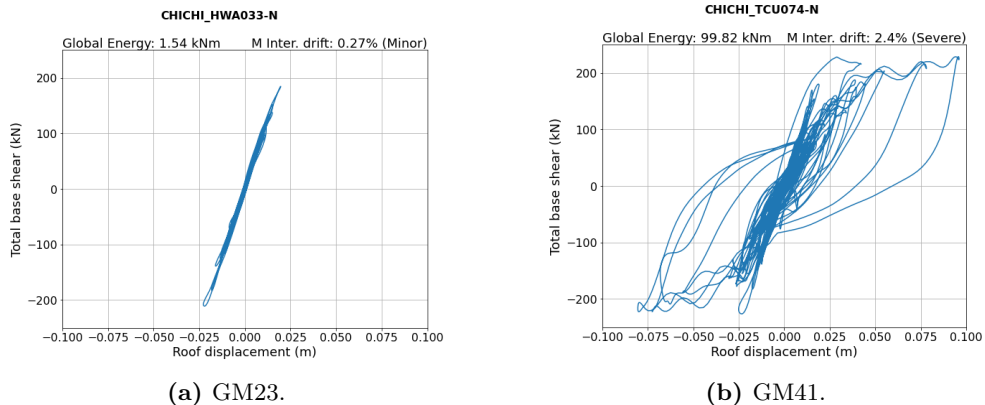


Figure 4.12: Hysteresis loops for the investigated frame structure. The area enveloped by the loops is an indication of the global energy dissipated.

The existing relation between the energy and the linear or nonlinear behaviour can be used to define energy-based damage measures. Some studies have shown that such damage measures can provide a good estimation of damage due to seismic actions. Specifically, the global dissipated energy which is based on the total base shear and top deformation has been utilized as a basis of a damage measure such as the Park-Ang index [44]. Figure 4.12 shows how the different ground motions are associated with different levels of global energy, where Figure 4.12(b) is showing non-linear behaviour with permanent plastic deformations, whereas Figure 4.12(a) shows more linear behaviour.

In the following analyses only the global energy (GE) will be estimated for each ground excitation based on the total base shear and the roof deformation of the frame structure. Note that the GE is not associated directly with a damaged state. This means that given a GE value from an excitation, one cannot translate this into whether the structure is minor or severely damaged. The GE thus only corresponds to the behaviour of the structure, i.e. if permanent deformations have occurred.

A measure that however is used to classify the structural state in relation to damage, is the maximal peak inter-story drift. This measure is used in design codes such as SEAOC Vision 2000, FEMA-273 as well as FEMA-356 both used in the US [70, 15, 11]. Here the performance level as well as the damage state of the structure is based directly on the maximal inter-story drift as listed in Table 4.11. These limits define four different performance levels and the criteria defined in FEMA-356 for reinforced concrete buildings.

Table 4.11: Performance levels, corresponding damage state and maximal peak drift limits [31, 8].

Drift Limits, Eq. (4.3) %	Damage State	Performance Level	Interpretation
0.0 - 0.2	No damage	Fully operational	Sporadic occurrence of cracking.
0.2 - 0.5	Minor	Operational	Minor cracks; Partial crushing of concrete in columns.
0.5 - 1.5	Moderate	Life safety	Extensive large cracks; Spalling of concrete in weaker elements.
1.5 - 2.5	Severe	Near collapse	Extensive crashing of concrete; Disclosure of buckled reinforcement.
>2.5	Collapse	Total collapse	Partial or total collapse of building.

These drift limits are based on the maximal peak inter-story drift Δ_{\max} defined as in Equation (4.3) [61].

$$\Delta_{\max} = \max_i (\Delta_{p,i}) \quad \text{where} \quad \Delta_{p,i} = \max_t \left(\frac{D_i(t) - D_{i-1}(t)}{h_i} \right) \quad (4.3)$$

Here the peak inter-story drift, $\Delta_{p,i}$, is defined as the maximal inter-story drift that occurs between two adjacent floors. The drift is then determined based on the deformations $D_i(t)$ and $D_{i-1}(t)$ of the i -th floor, as well as its story height h_i . In the case of the frame structure, all storey heights are the same such that $h_i = 3.5$ m. The maximal peak inter-story drift is then the maximal value for all the peak drifts.

In the literature, as well as in the design codes, there are different definitions of the inter-storey drift, both in terms of the maximal peak inter-story drift as seen in Equation (4.3), as well as the residual inter-story drift. The difference is that the residual is not dependent on the time, but simply determines the drift based on the residual deformations between the two adjacent floors. The residual drift then has the advantage that it can be measured directly on the real structure after a seismic event, whereas the peak drift is dependent on knowing the deformation throughout the event. Therefore, a dynamic FE analysis is required to determine the peak drift. In the coming analyses, only the maximal peak inter-story drift is used. The introduced quantities - i.e. GE and maximum inter-storey drift - are listed for GM23 and GM41 in Table 4.12.

Table 4.12: Global dissipated energy and maximum inter-storey drift for GM23 and GM41.

GM ID	GM Name	Global Energy	Δ_{\max}	Damage State
23	CHICHI-HWA033-N	1.54 kNm	0.27 %	Minor
41	CHICHI-TCU074-N	99.82 kNm	2.40 %	Severe

Here it is seen that both GMs are classified as non-linear based on the GE, however where GM23 is close to the threshold of 1.5 kNm. Both GMs are also classified as being non-linear in relation to the maximal drift, where GM23 is classified as being Minor and GM41 is classified as being Severe.

4.3.4.3 Estimation of structural state

Since the global energy and the maximal peak inter-story drift can be both defined for each ground motion, these quantities can be related. A total of 903 ground excitations have been analysed using the FE model, and their respective energy and drift values are seen in Figure 4.13.

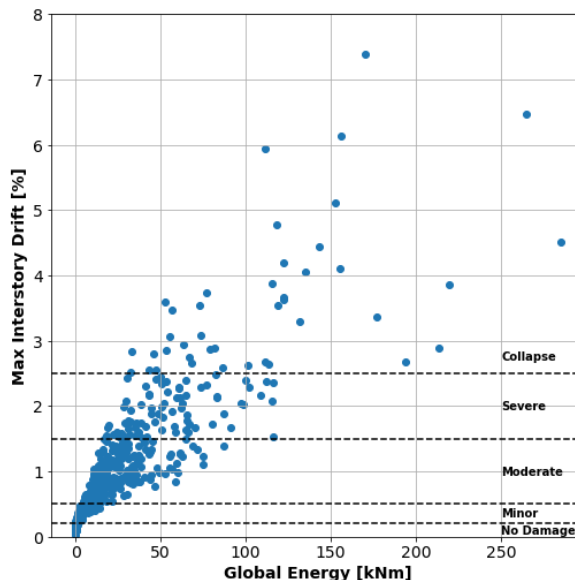


Figure 4.13: Correlation between Global Energy and maximal peak inter-story drift, given 903 ground motion excitations.

The figure shows that there is a linear dependency between the two quantities. This means that a ground motion that dissipates a large amount of global energy is associated with a large maximal inter-story drift. In order to depict the damage states, the figure further shows the drift limits given in Table 4.11. However, a single energy level can fall within multiple damage states. For instance, given that the structure has dissipated 50 kNm of energy, this can either be classified as either Moderate, Severe or Collapse in terms of the damaged state. However, when looking at Figure 4.14 where only low-energy dissipations within the range of 0 kNm to 6 kNm are considered, a closer relation between the global energy and inter-story drift is seen.

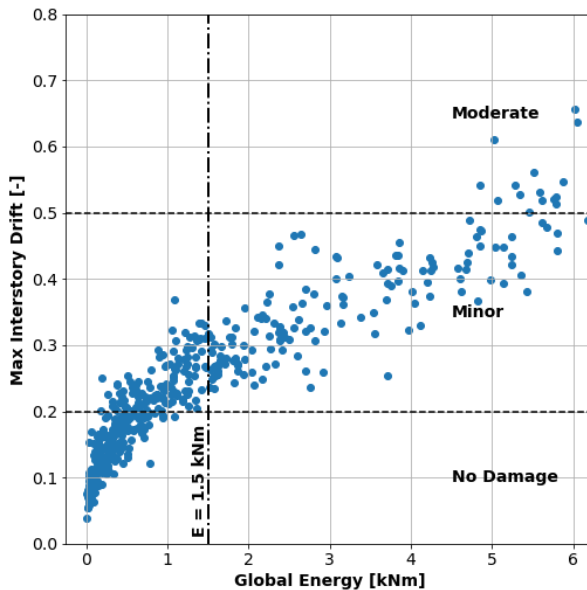


Figure 4.14: Correlation between Global Energy and maximal inter-story drift in the range between 0 kNm and 6 kNm, given 903 ground motions.

Here it is noticed that for the arbitrary value of 1.5 kNm, all states of the structure is within the Minor category of damage state. Further are no Non-Damaged state to be found above this threshold. Given the assumption that a linear behaviour is related to no damage, the threshold of 1.5 kNm may be used to distinguish between linear and non-linear responses of the structure. This assumption seems to be plausible since beyond this threshold of dissipated energy *all* the responses are classified as being damaged.

Through the threshold of 1.5 kNm that has been introduced, the present report will label the structural responses and the associated GMs as linear or non-linear such that:

- **Linear:** are the responses and the associated GMs whose excitation leads the structure to dissipate an amount of global energy that is lower than or equal to 1.5 kNm.
The structure is within the undamaged state, and therefore still operates in the *linear* regime.
- **Non-linear:** are the responses and the associated GMs whose excitation leads the structure to dissipate an amount of energy more than 1.5 kNm.
The structure is categorized within one of the four different damage stages: Minor, Moderate, Severe or Collapse. Therefore, the structure is within the

non-linear regime. The corresponding performance level and interpretation of each damage state is listed in Table 4.11.

According to the given threshold between linear and non-linear behaviour of the structure, it is found that the set of 903 ground motions consists of 325 linear ground motions and 578 which are classified as nonlinear. The overview of these classifications is given in Table 4.10. Here the number of linear and non-linear responses are listed for the three subsets of GMs according to their load-factors of either 1, 0.5, or 1.5.

Another relation to be investigated is between the global energy and the PGA measured from the ground motion. This relation is shown in Figure 4.15. Here it can be seen that a large amount of dissipated energy is in general related to a large PGA of the ground motion. Note though that for lower values of energy, the PGA range is larger. For instance, when having an energy level of 150 kNm, the associated PGAs are within the range of 0.56 g and 0.72 g, whereas for an energy level of 50 kNm is the range of PGAs between 0.2 g and 0.72 g. The lower limit of the range is then the only one to vary.

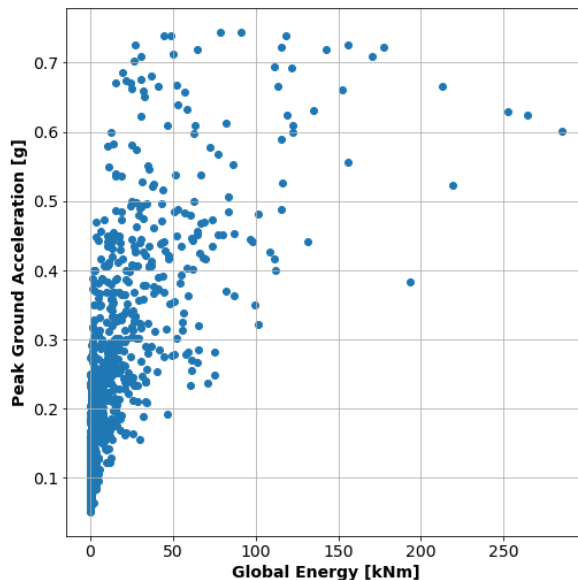


Figure 4.15: Peak ground acceleration of GM compared with global energy.

This could be caused by the fact the PGA is a measure only of the peak amplitude. It would then be possible to have a large PGA associated with motions whose frequencies do not coexist within the natural frequencies of the structure. This would mean that the excitation is having a small impact on the structure, leading to a low-energy dissipation. However, when large PGA events cause the structure to resonate, the

excitation then has a large impact on the structure that would dissipate more energy. On the other hand, excitations with a low PGA would have difficulties making the structure dissipate large amounts of energy since the amplitude is not large enough. This could be true even if the excitation makes the structure resonate.

4.3.5 Non-linearity of the structure

With the FE model made and the ground motions selected and implemented, the structure is investigated in terms of whether it operates in the linear or nonlinear regime. In Section 4.3.4.2 a threshold were proposed based on the global energy dissipated of the structure. However, investigations are to be made to verify that the structure is indeed able to behave in the non-linear regime.

In Section 3.3 it was mentioned that an element is either in a linear or non-linear regime, dependent on the level of deformations. If the material is in the linear regime, a linear constant stiffness relates the forces and the deformations. However, if this stiffness is no longer constant, the material is then in the non-linear regime. The FE model is able to record the history of the whole stiffness matrix \mathbf{K} that is composed of all the local stiffness contributions for the elements of the structure. Meaning that if the stiffness matrix is constant, all the elements are in the linear regime, whereas if the stiffness matrix changes over time specific elements are in the non-linear regime. This indication of linearity or non-linearity is then used to estimate if the structure and therefore the responses are linear or non-linear.

Since this analysis is made using a FE model, the EOM must be numerically evaluated through methods that are appropriate for nonlinear systems. For the analysis and modelling the Newton-Raphson iteration method stiffness has been used to evaluate the constitutive law of the materials, while Newmark integration is used to determine the time histories in terms of displacement, velocity and acceleration. The specific algorithm of 'average acceleration' is used for the Newmark integration with the parameters of $\gamma = 1/2$ and $\beta = 1/4$. This method is of particular relevance since it is unconditionally stable regardless of the time step used for the analysis [10]. This means that the method converges no matter the stepping size selected for the integration.

In Figure 4.16 and Figure 4.17 the stiffness matrix for the GM23 and GM41 are shown respectively, at different times. The reported values represent the difference between the stiffness matrix at a time t and the initial time instant of the earthquake $t = 0$. I.e. the figures showcase $\mathbf{K}_{t,0}(t) = |\mathbf{K}(t) - \mathbf{K}(0)|$.

During the initial part of the seismic events where the measured amplitudes are low, the difference in the stiffness matrix $\mathbf{K}_{t,0}(t)$ is relatively small since these small acceleration amplitudes are not large enough to force the structure into the non-linear

regime. Figure 4.16(a) and Figure 4.17(a) show the difference in stiffness matrix at the time $t = 20$ s, where only small differences are to be seen. For time instants where the acceleration reaches higher amplitudes, it is expected to see a large difference between the initial and current stiffness matrices since the elements are more likely to be in the non-linear regime. This is the case for Figure 4.16(b) and Figure 4.17(b) where the difference is seen at time $t = 43$ s and $t = 46$ s respectively. These are the times when the largest difference is to be seen.

The accelerations associated with the matrices are shown in Figure 4.9. In Section 4.3.1.2 it has been stated that GM41 is expected to generate more severe consequences on the structure than GM23. This is clearly shown in Figure 4.16(b) and Figure 4.17(b) since the variation caused by GM41 in the stiffness matrix, is higher than in the case of GM23. Such a high variation indicates that the structure is indeed behaving non-linearly and that damage has occurred. More precisely, it can be seen that the highest variation of stiffness corresponds with the first DOFs which are related to the column elements between the ground floor and the first floor. These elements are usually the most damaged when an earthquake takes place.

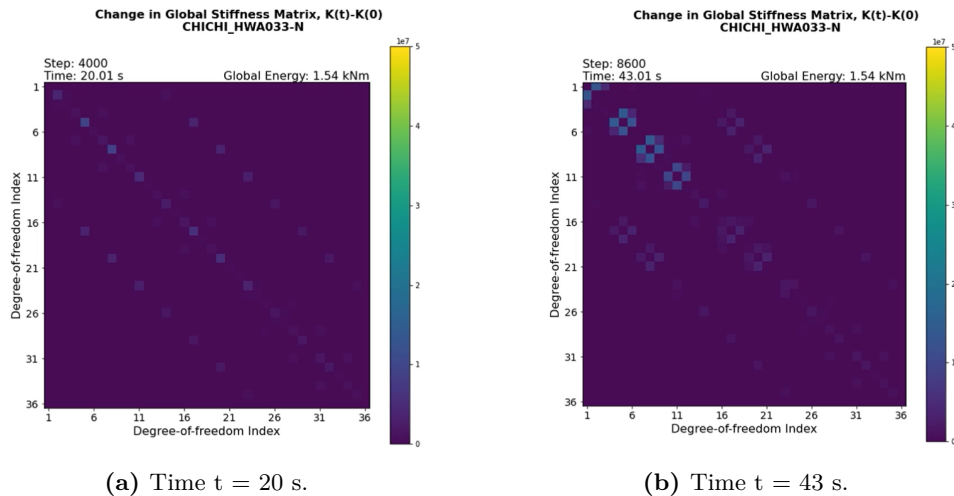


Figure 4.16: Stiffness matrix evolution for GM 23 CHICHI-HWA033-N.

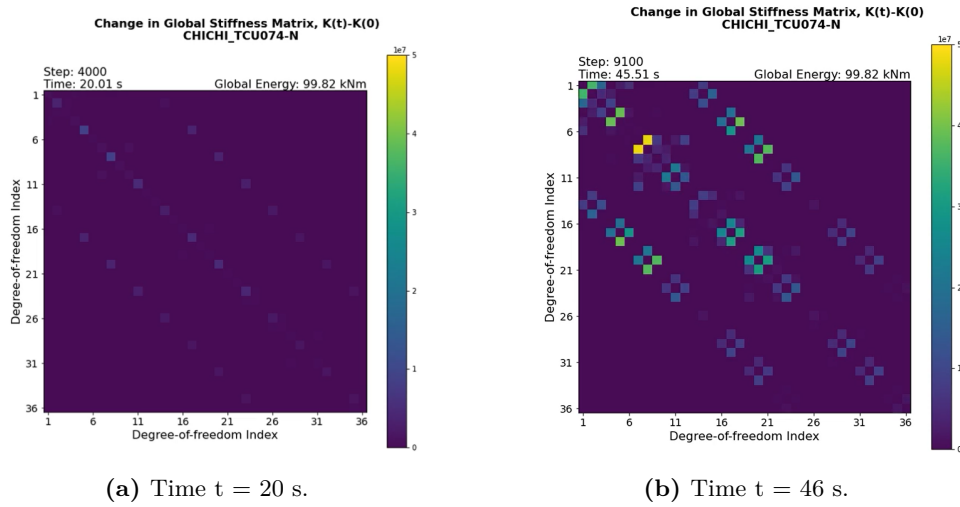


Figure 4.17: Stiffness matrix evolution for GM 41 CHICHI-TCU074-N.

CHAPTER 5

Results: Gaussian Process Regression

In the following chapter, the Gaussian Process (GP) is to be used to predict structural responses only in the form of acceleration time histories. Therefore, the utilization of the GP in the described task is evaluated.

The reported results are related to two different studies: preliminary analyses and overall assessment. The two approaches differ both in the number of responses included in the analyses and in their objectives.

Most of the preliminary analyses made use of seven different ground motions and the associated responses to show the effects of the hyper-parameter's optimization, and how the performance of the model changes for different sensor layouts. On the other hand, for the evaluation of GP with respect to the entire data included in the project, the overall assessment is based either on all responses related to the whole Standard-amplitude set (SAS) or on responses within the combination of the 3 sets presented in Table 4.10.

5.1 Preliminary study

The results presented in the following, aim to illustrate the changes in the model's performance due to the optimization of the Kernel's hyper-parameters and different sensor layouts. The idea behind the designed simulations is also to show simple examples of the applications of the GP. Hence, for each of the introduced cases, the simulation is carried out by considering only a few responses both in the training phase and in the testing phase. However, both the layout of the input and output nodes together with the utilization / non-utilization of optimization algorithms will vary along with the considered cases.

In each case, the model will be trained and tested on responses that correspond to the same selection of GMs, if not otherwise specified. The GP will be trained on responses corresponding to five ground motions while the testing is based on predicting

responses associated with two different ground motions. The five signals used for the training have been randomly selected from the SAS load-set, while the two signals considered in the test phase correspond to the seismic events already introduced in Section 4.3.1. Therefore, the prediction of the signals related to GM23 and GM41 will be presented, with varying output nodes. The formed ID corresponds to the earthquake whose label is CHICHI-HWA033-N while the latter response is generated by CHICHI-TCU074-N. In Table 5.1 is an overview of the training and testing sets used in the preliminary analyses of the GP. The sets only include accelerational responses with response IDs that are associated with the GM IDs.

Table 5.1: Train set used in the preliminary study.

Set label	Response IDs	Number of responses
Train-1	052, 086, 149, 182, 247	5
Test-1	023, 041	2

Note that the acceleration responses have been recorded at each node of the structure. However, during the training phase, the model is fed only with those signals corresponding to the nodes provided with a sensor. The sensors' number and position will be specified for each of the presented cases together with the location of the output node - i.e. where the response is predicted. The collection of the input sensors and of the output nodes defines the layout used for each of the considered cases.

For conciseness, the following sections show the results only for the responses with ID 041, while the results for the responses with ID 023 are given in Appendix E. Moreover, the plots in the time and frequency domain as well as the response spectra for the ground motions that generated the responses of the set Train-1 listed in Table 5.1, are also included in Appendix E.

Finally, one more general analysis is presented in the context of the preliminary analyses. The study tries to extend the investigation of the sensor layout by considering all responses related to the SAS load-set, in order to consider all the possible sensors' positions.

5.1.1 Case 1: Effects of optimization

In order to present how the optimization changes the Kernel's hyper-parameters and the correspondent GP output, two different simulations have been performed.

In both cases the training and testing sets correspond to the set Train-1 and Test-1 introduced in Table 5.1. The main settings of the simulations are reported in Table 5.2 while the values of the other parameters have been set in Section 2.2. These are summarized as: sub-vector length $l = 25$, stepping size of the sub-vectors $s = 5$ for

training and $s = 1$ for testing, the variance σ_ϵ of the model's noise is set to 1 and lastly, the Kernel's hyper-parameters σ_k^2 and τ_k are both initially set to 1.

Table 5.2: Case1: Settings of the simulations used to present the effects of the optimization.

Case index	Optimization	Input nodes	Output nodes	Ref. figure
C1.1	No	23, 33, 43	22	5.1(a)
C1.2	Yes	23, 33, 43	22	5.2(a)

Case 1 represents the first example of the estimation of the acceleration response at node 22 given the response of one sensor per each floor. Figure 5.1(a) shows the input and the predicted nodes, i.e. the position of the sensors, while Figure 5.1(b) illustrates the true signal as well as the prediction. Here, the upper plot consists of the comparison between the real acceleration signal at node 22 and the estimated signal from the GP.

If the prediction was exact, the two signals would be overlapping. Note that apart from the plots, Figure 5.1(b) reports also other information such as the GM label and the final value of the Kernel's parameters, i.e. variance and length-scale. More precisely, the value of the σ and τ is reported as an array where the first and the last value correspond with the sensor at the lowest and at the top floor respectively. This is due to the fact that the array of the input nodes displayed in the same figure follows the same order, i.e from node 23 on the first floor to node 43 on the top floor.

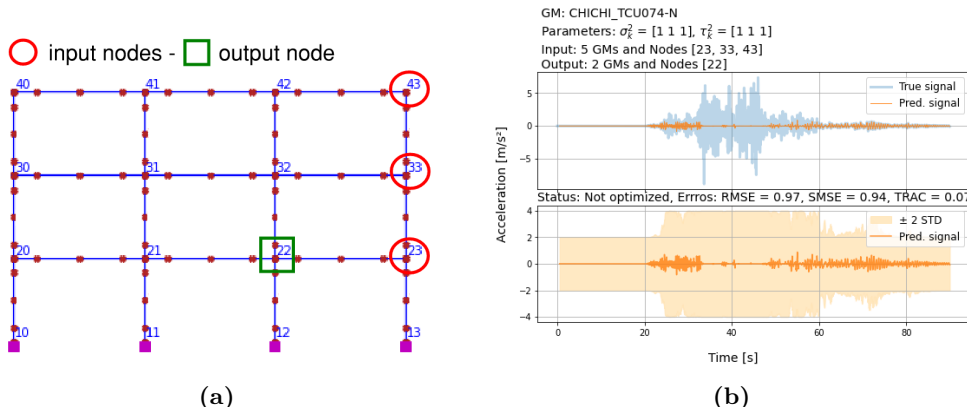


Figure 5.1: C1.1: Non-optimized GP, prediction of CHICHI-TCU074-N, ID 41. Input and output nodes (a) - results and errors (b).

In Case 1.1, the GP has not been optimized, hence the value of the Kernel's parameters remains equal to 1 which is the initial value. It can be noticed that the value

of the errors is high while the TRAC value is low. Those values suit the inexact prediction shown in the top plot of Figure 5.1(b). The incapability of the model in estimating the signal is proved also by the large credible interval, which are seen in the bottom plot of Figure 5.1(b). It is broad throughout the whole duration of the seismic event, but it is even wider where the true acceleration has its largest amplitudes.

The described trend can be seen as a larger uncertainty of the GP in predicting the largest amplitudes of the signal.

Figure 5.2 illustrates the results for Case 1.2, where the main difference from the previous simulation is that an optimization has been run. The optimization is in relation to the hyper-parameters of the Kernel, meaning the variances σ_k^2 and the length-scales τ_k . As can be seen in Figure 5.2(b), the final values of the Kernel's parameters are no longer equal to the initial values of $\sigma_k^2 = \tau_k = 1$.

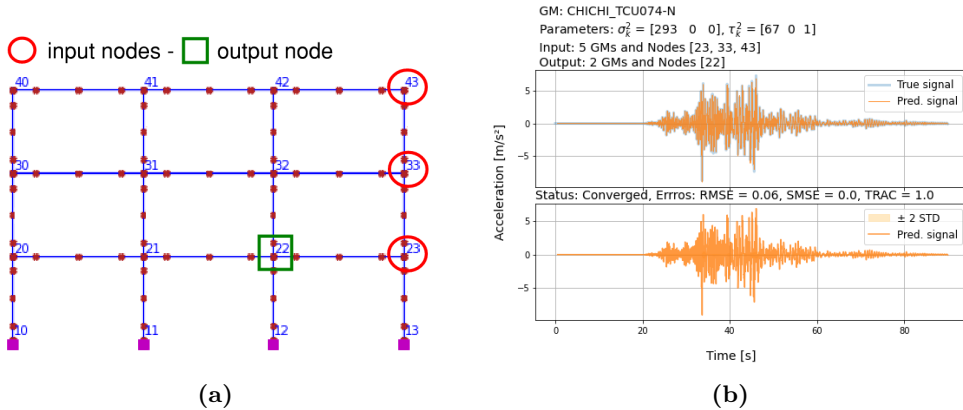


Figure 5.2: C1.2: Optimized GP, prediction of CHICHI-TCU074-N, ID 41. Input and output nodes (a) - results and errors (b).

Overall, it is clear that the GP has performed better when the hyper-parameters have been optimized, in relation to case C1.1. An interesting aspect that must be emphasised is the optimized values of the variance parameters at each level, which are listed in Table 5.3.

Table 5.3: Case 1: Input nodes and optimized variances for each node. C1.1 is not optimized, meaning the initial values are listed.

Case ID	C1.1			C1.2		
	23	33	43	23	33	43
Input node, n_k	23	33	43	23	33	43
Optimized variance, σ_k^2	1	1	1	293	0	0

Here it is seen that the only variance different than zero corresponds with node 23, which is located on the same floor as the prediction node 22; its magnitude is much higher than 1. This leads to a final Kernel matrix with individual elements of values also larger than 1.

As mentioned in Section 2.3, the variance for each input node represents a scale-factor for each of the terms in the sum-kernel.

In the case of C1.2, the optimization renders the inputs given by nodes 33 and 43 to be irrelevant, given both their scale-factors are equal to zero. The prediction of the response in node 22 is then only based on the given response in node 23.

In Figure 5.3 are the kernel matrices seen for both cases. It is seen that the non-optimized kernel in Figure 5.3(a) only shows a high value, i.e. a large correlation, between some of the inputs, whereas the optimized kernel matrix shows more correlation in general with larger values throughout.

Note the difference in scale between the two matrices; this is once more due to the difference in scale-factor.

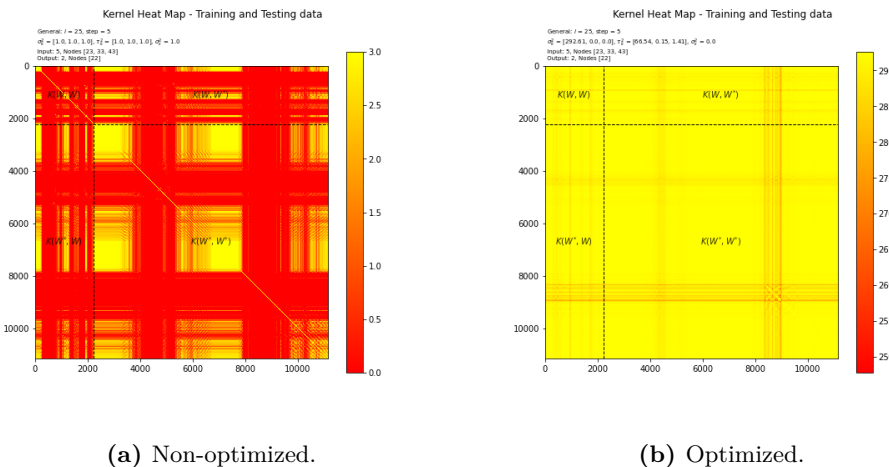


Figure 5.3: Comparison of Kernel matrix for GP, prediction of CHICHI-TCU074-N, ID 41. With optimized parameters (a) - without optimized parameters (b)

5.1.2 Case 2: Effects on sensors location

From the previous investigation, an important observation has been noted. In C1.2, where the optimization of the parameters was performed, the GP used only the sensor on the first floor while the data from the other sensors have been neglected. This might be a trivial conclusion since the predicted acceleration is related to a node placed on the same level. Whether it is trivial, is to be investigated in the present

section.

For the given case the training and testing sets, as well as the initial parameterization of the hyper-parameters are the same as in Case 1. Also, the same responses associated with the GMs in Table 5.1 are to be used.

Where the previous Case 1 focused on the prediction of an acceleration signal on the first floor, this case tries to predict accelerational signals on levels 2 and 3. The input and output nodes as well as the associated figures are listed in Table 5.4.

Table 5.4: Case 2: Settings of the simulations used to present the effects of the optimization.

Case index	Optimization	Input nodes	Output nodes	Ref. figure
C2.1	Yes	23, 33, 43	32	5.4(a)
C2.2	Yes	23, 33, 43	42	5.5(a)

In Figure 5.4 and Figure 5.5 the nodes used in C2.1 and C2.2 are shown, along with the prediction after the optimization. In C2.1 and C2.2 one sensor per each floor is taken into account and used as input nodes. In the former case, the node at which the acceleration signal is to be predicted is placed on the second floor, while for C2.2, the prediction node is placed on the third floor.

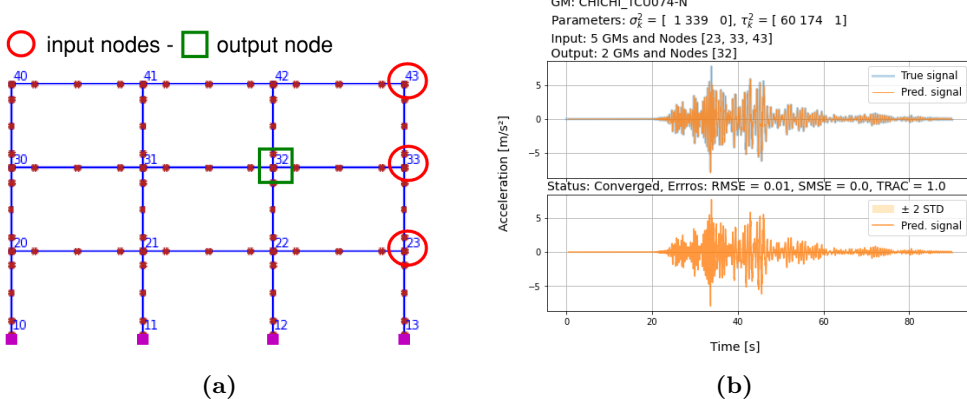


Figure 5.4: C2.1: Optimized GP, prediction of CHICHI-TCU074-N, ID 41. Input and output nodes (a) - results and errors (b).

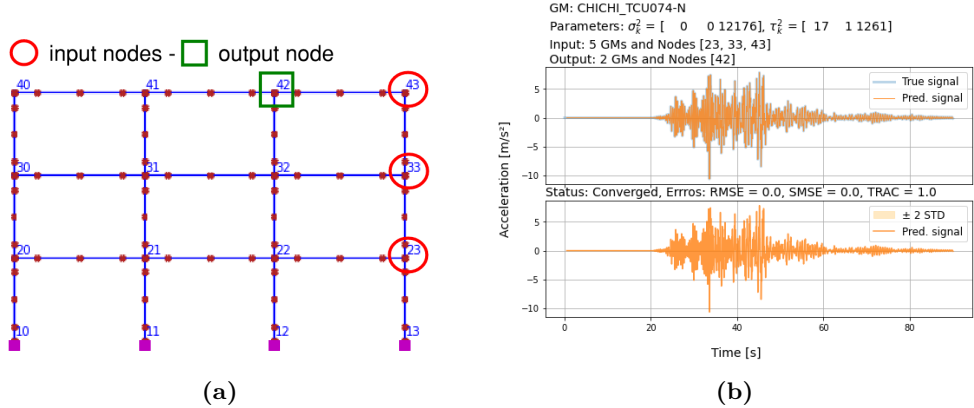


Figure 5.5: C2.2: Optimized GP, prediction of CHICHI-TCU074-N, ID 41. Input and output nodes (a) - results and errors (b).

For both cases, the predicted signals closely resembled the true signals for each of the nodes. This is due to the optimization of the hyper-parameters. The input nodes and their associated variances after optimization is listed in Table 5.5.

Table 5.5: Case 2: Input nodes and optimized variances for each node.

Case ID	C2.1			C2.2		
	23	33	43	23	33	43
Input node, n_k	23	33	43	23	33	43
Optimized variance, σ_k^2	1	339	0	0	0	12176

According to the optimized variances, the GP is using mainly the acceleration data recorded from the sensor placed on the same floor as the output node. This is the case for both C2.1 as well as C2.2.

In C2.1 the variance associated with the input node 23 is equal to 1. However, in relation to the variance of 339 related to the input node 33, node 23 only contributed an insignificant amount. It is then safe to assume that this contribution can be neglected.

In the C2.2, the only non-zero variance is once more the one associated with the same floor as where the prediction is to take place. Note the large variance of 12176 in comparison to C2.1 where the largest variance is 339. This increase in variance may be explained by the larger accelerations amplitudes seen for the prediction in C2.2.

This means that when predicting an acceleration response, only the inputs given from the same floor as the output node are made relevant by the GP.

This may be caused by the fact that the structure is a frame structure, where each floor functions as a stiff diaphragm. Therefore, responses generated from a node

are much more similar to responses of nodes placed on the same floor, than when considering a note on a different floor. This is also noted from the mode shapes of the structure, where each floor moves together as a whole.

If a different structure with a different geometrical layout were to be investigated, these conclusions may not be the same as for the given frame structure.

5.1.3 Case 3: Effects on distance

It is clear that the GP does prefer the data that is provided from the closest sensor. Yet, in the entirety of the considered cases, the adjacent sensor was always placed at the same level as the output node. The next investigation is to set up a simulation with the closest sensor placed at a different level than the output node, with a summary listed in Table 5.6.

Table 5.6: Case 3: Settings of the simulations used to present the effects of the optimization.

Case index	Optimization	Input nodes	Output nodes	Ref. figure
C3.1	Yes	20, 33, 40	30	5.6(a)

In the present case, the distance between the output node: 30 at level 2 and, the inputs nodes: 40 at level 3, and 20 at level 1, is equal to 3.5 m vertically. While the distance between node 30 and the input node 33 is 16.5 m horizontally. The location of the nodes as well as the predicted response is shown in Figure 5.6.

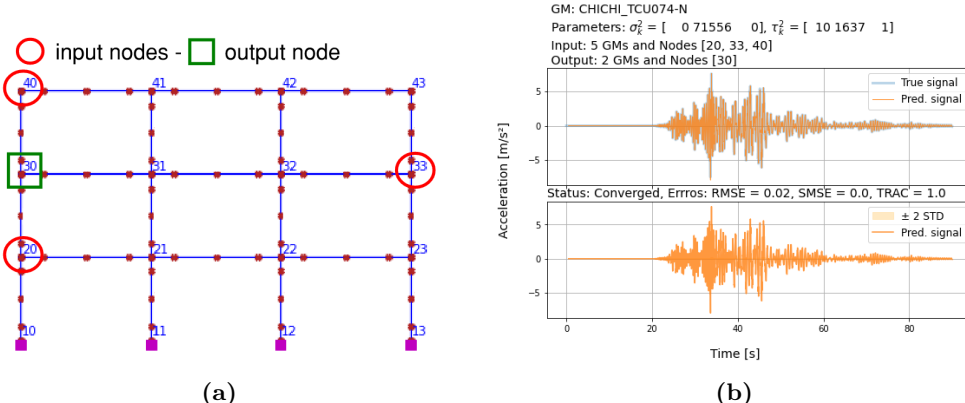


Figure 5.6: C3.1: Optimized GP, prediction of CHICHI-TCU074-N, ID 41. Input and output nodes (a) - results and errors (b).

Although node 33 is the input node with the largest physical distance to the output

node, after the optimization node 33 is the only one to have a variance different from zero, as listen in Table 5.7.

Table 5.7: Case 3: Input nodes and optimized variances for each node.

Case ID	C3.1		
Input node, n_k	20	33	40
Optimized variance, σ_k^2	0	71556	0

This means that the physical distance is not enough to make the model favour an input node from a different floor than one from where the predictions are to be made. For the given structure, the accelerational responses, given the same floor, are then too similar such that the optimization makes all other floors irrelevant when the predictions are to be made.

5.1.4 Case 4: Removal of most related inputs

The last cases demonstrated that the GP was able to provide an accurate estimation for the considered responses 023 and 041 when a sensor is placed on the same floor as the predicted node. It showcases that when the model is provided with additional information derived from sensors on other floors, these are neglected in favour of inputs on the same floor as where the prediction is to take place.

Further investigations have been conducted to evaluate the performance of the GP when the sensor is placed on the third or first level with respect to the predicted node being located on the second level. The base case for the following study is C2.1 reported in Table 5.4 and Figure 5.4. C2.1 shows that the GP provides a precise estimation of the acceleration signal in node 32 by considering only node 33 - i.e., it is the only sensor with a scaling factor different from zero. The overview of the performed analyses is reported in Table 5.8

Table 5.8: Case 4: Settings of the simulations used to present the effects of the optimization.

Case index	Optimization	Input nodes	Output nodes	Ref. figure
C4.1	Yes	43	32	5.7(a)
C4.2	Yes	33	32	5.8(a)

In the following analyses, the only data inputted in the GP is generated from a sensor placed either on the third floor (node 43) or on the first floor (node 23), where the prediction is for node 32 on the second floor. The results for the former case are reported in Figure 5.7(b) while the plots for the latter case are shown in Figure 5.8(b).

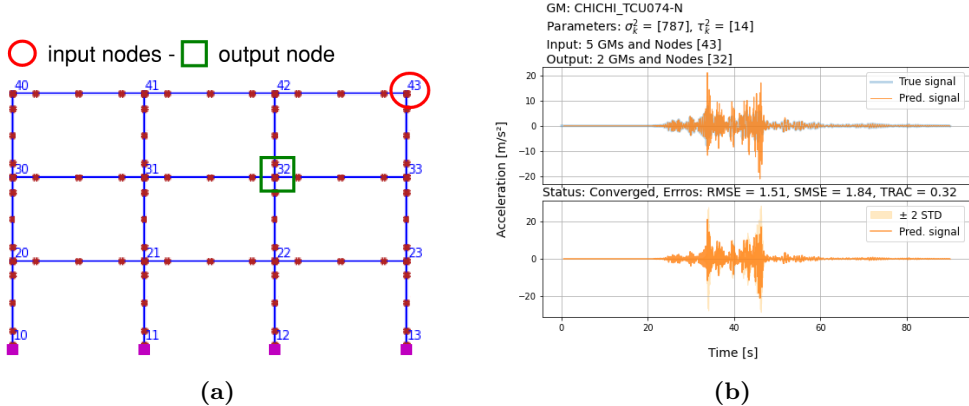


Figure 5.7: C4.1: Optimized GP, prediction of CHICHI-TCU074-N, ID 41. Input and output nodes (a) - results and errors (b).

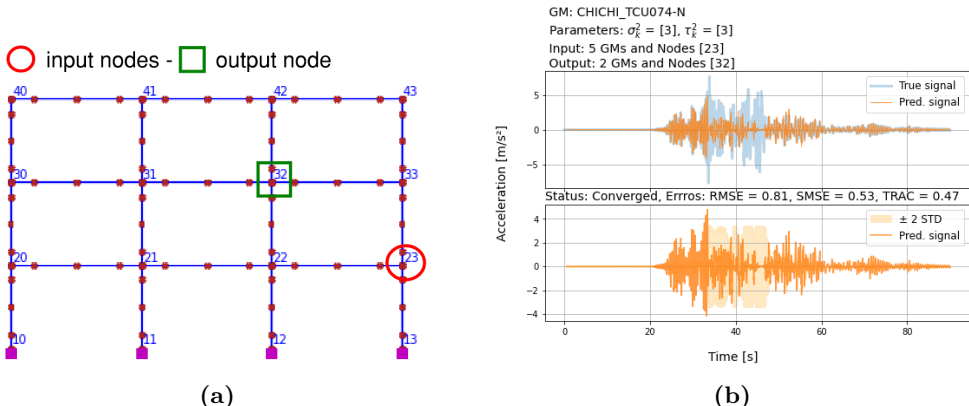


Figure 5.8: C4.2: Optimized GP, prediction of CHICHI-TCU074-N, ID 41. Input and output nodes (a) - results and errors (b).

The reported plots show that the performance of the GP drops in comparison to all the cases previously introduced since the predicted response does not follow the true signal as well. In the case of C4.1 the predicted signal is larger than the true signal, whereas points predicted in C4.2 are lower than the true ones. Note that for C4.2, for those time instants where the predicted values differ the most from the true response, the uncertainty is largest as represented by a larger standard deviation of the prediction.

In order to assess the performance of the prediction the error measures and TRAC are used. In Table 5.9 are listed the error values for the cases discussed in the last

paragraphs for response 041, GM CHICHI-TCU074-N.

Table 5.9: Error and TRAC values for GP predicting signal in node 32, given different input nodes. Response 041, GM CHICHI-TCU074-N

Case index	RMSE	SMSE	TRAC
C2.1	0.01	0.0	1.0
C4.1	1.51	1.84	0.32
C4.2	0.81	0.53	0.47

In Case 4, where the inputs were given from different floors than the output node, the error measures are larger while the TRAC results in a lower value. The worst estimation has been attained in C4.1 and it is clearly displayed in the Figure 5.7(b). The true signal corresponding to the considered motion is characterized by a rugged shape. Therefore, it is of interest to notice that the results reported in Figure 5.9 and in Appendix E for the response with ID23 associated with GM CHICHI-HWA033-N, show better estimations.

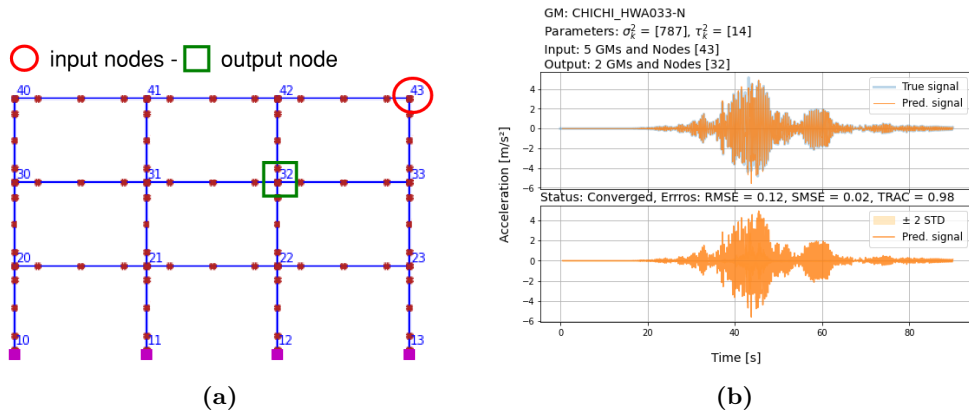


Figure 5.9: C4.1: Optimized GP, prediction of CHICHI-HWA033-N, ID 23. Input and output nodes (a) - results and errors (b).

Here the true signal has a more regular shape. Some of the error and TRAC values relative to response 023, GM CHICHI-HWA033-N are illustrated in Table 5.10. The prediction is more or less exact in C2.1, but also in C4.1 and C4.2 where the estimations are sufficiently accurate.

Table 5.10: Error and TRAC values for GP predicting signal in node 32, given different input nodes. Response 023, GM CHICHI-HWA033-N

Case index	RMSE	SMSE	TRAC
C2.1	0.0	0.0	1.0
C4.1	0.12	0.02	0.98
C4.2	0.18	0.04	0.97

The whole observations included in the present section hold only for the GM CHICHI-TCU074-N and CHICHI-HWA033-N. The aim of the following sections will be to generalize the evaluation of the Gaussian Process.

5.1.5 Generalization: Sensor location

Based on the previous investigation, it is seen that the model is able to predict responses in a node when it is provided with responses recorded in a node from a different floor. However, it has been noted a significant difference in the prediction's accuracy that depends on the amplitude of the response. Further, it has been investigated that if given multiple input-nodes, the model will optimize, such that only the node on the same floor is used for the prediction. This raises the question of how the model is able to perform given one input node in order to predict the response at a different location.

This case utilizes a training set of five responses and a training set that includes the remaining 296 responses, all associated with the SAS load-set¹. One node is then used as an input node in order to predict the responses at one output node. This procedure is repeated for all the combinations of input/output nodes, from where the error measures for these input/output pairs can be obtained.

In Figure 5.10 are the mean values of the TRAC measure shown for each input/output node pair. The mean value is estimated based on all the 296 measures for each response. This mean value is then representing the generalized tendency for these node-pairs.

¹The training set is composed as defined in Table 5.1.

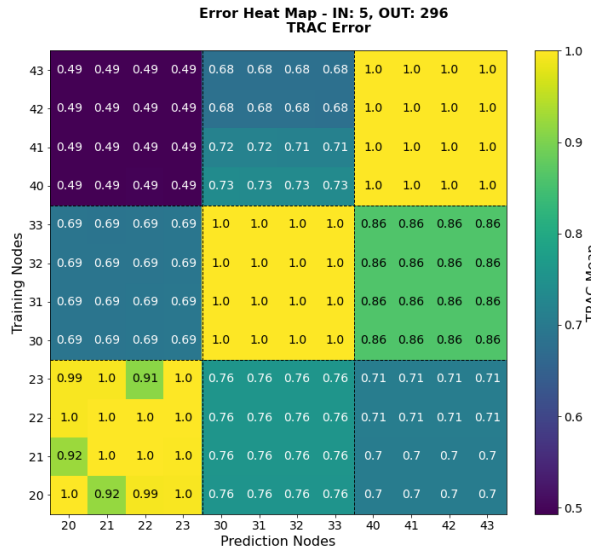
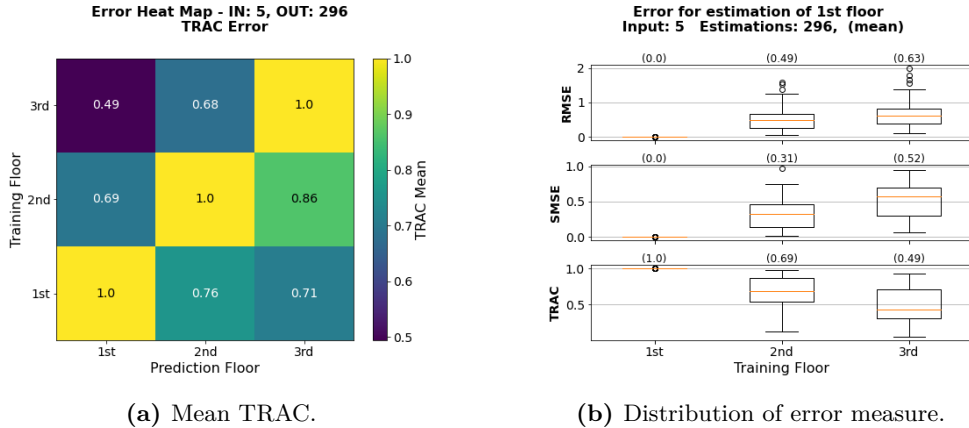


Figure 5.10: The mean TRAC measure for the 296 output responses for each input/output node pair.

It can be seen that the mean values do not vary if either the training or prediction node is changing location on the same floor. The floors then seem to not have a large difference in responses, which is also seen from the previous case-studies. However, if the nodes are changing location in terms of floor, a variety of the mean TRAC measure is noted with the smallest values occurring when predicting nodes 20-23 based on responses from nodes 40-43, i.e. the worst predictions in terms of TRAC occurs when predicting responses on the first floor based on responses on the third floor. Further, when predicting responses based on responses on the same floor, e.g. predicting on 2nd floor based on 2nd floor, the TRAC measure is equal to 1, meaning a perfect prediction in terms of shape.

These tendencies are the same for both the RMSE and SMSE measures, which are seen in Appendix F.

Due to the similar error estimations from nodes on the same floor, only one node for each floor is chosen to showcase the mean measure. This procedure has been done for the TRAC mean values and can be seen in Figure 5.11. The nodes chosen are 23, 33, and 43.



(a) Mean TRAC.

(b) Distribution of error measure.

Figure 5.11: Mean TRAC values and distribution of error values from the 296 predictions of the 1st floor.

Alongside the mean TRAC values are the distributions of the 296 error values seen in Figure 5.11(b). These distributions are depicted as box-plots for three error measures based on the predictions of the 1st floor. Each box-plot is then the distribution of each training input.

It can be seen that when estimating responses on the 1st floor the lowest errors are occurring when the predictions are based on responses from the 1st floor itself, where all values of the TRAC are close to 1. However, the error measures seem to increase the further away the input responses are from the 1st floor, with inputs from the 3rd floor having the worst predictions and a relatively wide distribution.

The same conclusions can be drawn from the remaining error measures and distributions based on other predictions, as seen in Appendix F.

5.2 Overall assessment of the model

The present section aims to evaluate the predictions provided by the Gaussian process for all the responses related to the SAS load-set in Section 4.3.1. The main differences from the preliminary analyses conducted in Section 5.1 is within; the selected responses used for the training phase, the selected responses used in the prediction phase, and nodes used for the predictions.

In the following analyses, there are two training sets to be considered. The responses used in both training sets have been randomly selected in relation to the SAS load-set, which includes 301 GMs all with a load-factor equal to 1. One of the training sets will be consisting of five responses, whereas the other set will be including 20 responses. The training set of 5 responses is identical to the one used in Table 5.1.

The related testing sets will then be the remaining responses related to the SAS load-

set. This means that in the case of five training responses, 296 responses are to be predicted, whereas 281 are to be predicted in the case where 20 responses are used for the training phase.

In regard to the nodes used for the input and predictions, the estimations will be made for node 42 given input from node 23.

In Table 5.11 an overview of the training and test sets used in this study is reported. In Case 5, a small training data-set is considered, while in the following case, the model is tested by considering a larger data-set. For the reasons related to the scalability of the GP, the model can include a maximum of 20 responses in relation to the training phase.

Table 5.11: Training and testing sets used for the overall assessment in Case 5 and Case 6. Only the responses related to the initial 301 GMs in the SAS load-set are to be used.

Case ID	Set label	Response IDs	Number of responses
Case 5	Train C5	052, 086, 149, 182, 247	5
	Test C5	Remanding, excluding training set.	296
Case 6	Train C6	013, 040, 053, 064, 073, 086, 092, 095, 121, 126 186, 204, 225, 226, 232, 234, 258, 260, 270, 295	20
	Test C6	Remanding, excluding training set.	281

One simulation has been carried out for each of the cases, given the prediction of the response in node 43 and the inputs from node 23. In order to give a complete overview of the obtained results and their accuracy, the Figure 5.12 does show the box-plots for the errors and the TRAC values. In the figure, there are the mean values for each error measure presented above each box-plot.

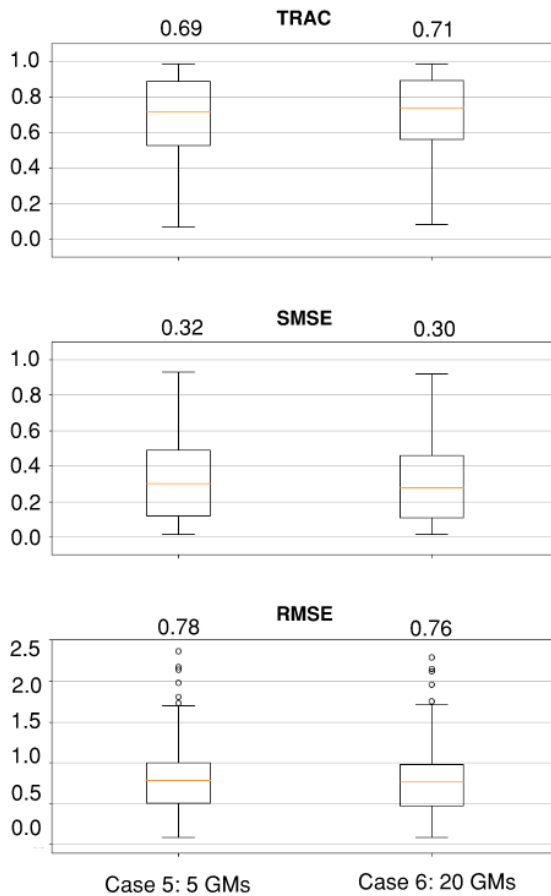


Figure 5.12: GP overall estimation: box plots of TRAC, SMSE and RMSE for Case 5 and Case 6. Input node: 23, output node: 42.

Both the box-plots and their mean values show that the results are difficult to distinguish since the distributions of the errors and of the TRAC values are almost the same in Case 5 and Case 6. This is an indication that increasing the amount of data used in the training phase did not lead to significant improvements in the estimations. This argument is strengthened when comparing the acceleration signals obtained in Case 5 and Case 6, for the responses associated with GM41 and GM23. The predictions for these GMs are seen in Figure 5.13 and Figure 5.14 respectively, while the correspondent error and TRAC values are listed in Table 5.12. Here, the two predictions are similar with both Case 5 and Case 6 having higher errors when predicting the larger amplitudes (ID41). Small improvements are thought to be seen since the RMSE and SMSE errors are lower when the training set includes more responses.

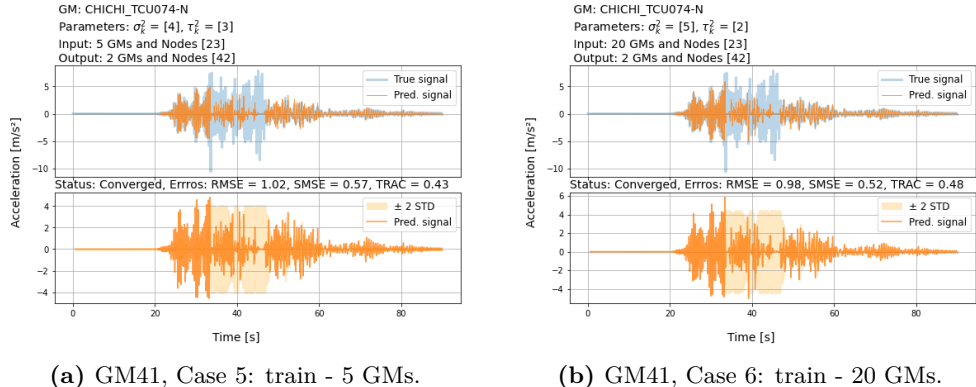


Figure 5.13: Comparison results Case 5 and Case 6 for the overall assessment of the GP. The predictions are seen for the responses associated with ground motion GM41 CHICHI-TCU074-N. The predictions were made in node 42 given the inputs from node 23.

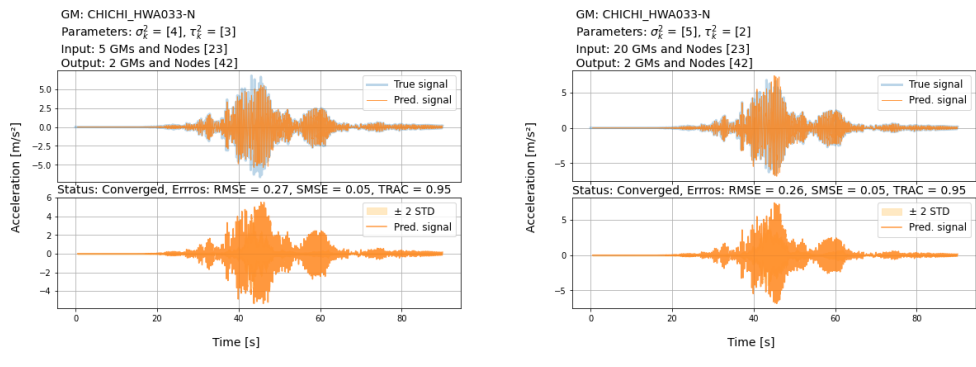


Figure 5.14: Comparison results Case 5 and Case 6 for the overall assessment of the GP. The predictions are seen for the responses associated with ground motion GM23 CHICHI-HWA033-N. The predictions were made in node 42 given the inputs from node 23.

Table 5.12: Error and TRAC values for Case 5 and Case 6. The listed values refer to the prediction of the signals associated with CHICHI-TCU074-N and CHICHI-HWA033-N. Input node:23, output node:42

GM Name	Response ID	Case 5			Case 6		
		RMSE	SMSE	TRAC	RMSE	SMSE	TRAC
CHICHI-TCU074-N	41	1.02	0.57	0.43	0.98	0.52	0.48
CHICHI-HWA033-N	23	0.27	0.05	0.95	0.26	0.05	0.95

Apart from the small improvement driven by the selection of a larger training set, another point can be observed from the presented results. All the box-plots show a long distance between the 25th and the 75th percentiles, as well as relatively long whisker lengths.

Moreover, for Case 5 as well as Case 6, regarding the RMSE, it is possible to see some outliers with much higher RMSE than the average. These observations suggest that the GP is not able to generalize well and the accuracy of the predicted responses might vary when different seismic events are considered; in some cases, the prediction can be very precise while in other cases it might be much different than the real signal.

The performance of the GP is highly dependent on the signal the model is to predict. This becomes clear when comparing the predictions associated with GM23 CHICHI-HWA033-N and GM41 CHICHI-TCU074-N showed in Figure 5.14 and Figure 5.13. The main difference between these signals lies in their shape where the former presents a regular shape with a peak varying between 2 m/s² and 5 m/s² while the latter has a rugged shape and peaks reaching the 8 m/s². The higher acceleration presented in signal 41 must be associated with more severe consequences in the structure due to the occurred earthquake. This has already been assessed when the global dissipated energy and the damage state associated with GM23 and GM41 have been evaluated and listed in Table 4.12. Therefore, it is a matter of interest for the present project to further investigate the relation of the final damage state of the structure with the error introduced in the predictions.

5.3 Influence of the final structural damage state

It has previously been observed that the final state of the structure, whether linear or non-linear, can have an influence on the accuracy of the predictions. Such dependency might be generated by an inadequate selection of the responses used to train the GP.

The common practice of machine learning consists in using most of the available data, around 60 % or 80 % for training the model [47]. This is done in order for the model to have a large set of data, such that the determination of the relations between the

input and outputs is based on more variety.

With this approach, the training of the GP model would be based on a wider range of responses representing an adequate amount of both linear and non-linear responses. However, the GP is trained only upon 7 % of the signals related to the SAS load-set, which counts 301 responses in total. The responses utilized for the training of the GP have until now been randomly selected, where it is not guaranteed that a good representation of different damage states is included. The random selection used for training may then consist of a majority of linear responses, which is not representing the testing responses well since this consists also of non-linear responses with energy dissipation of up to 250 kNm.

Therefore, the GP's difficulty in predicting large amplitude signals might be caused by the random procedure that has been followed to build the training sets. The present study then aims to train and test the GP through subsets of training and testing responses, that include exclusively linear responses or non-linear responses.

The selection of these training and testing sets will be based on responses related to the GMs with a load-factor of 0.5 and 1.5, since these are containing the responses categorized mostly as linear or non-linear respectively. From Table 4.10 is listed that 222 linear responses are related to the GMs with a load-factor of 0.5, whereas 275 non-linear responses are associated with the GMs with a load-factor of 1.5. These two sub-sets of GMs will be mentioned as the low-amplitude load-set (LAS) and the high-amplitude load-set (HAS) respectively.

The procedure is then go to through all 301 GMs in these two subsets. If a ground motion is classified as linear in the LAS, and the same ground motion is classified as non-linear in the HAS, the related response is included in the new training/testing set. After this procedure has been done, a total of 198 GMs are obtained in both the LAS as well as in the HAS. In Table 5.13 is a representation of the 198 selected GMs that are selected based on the method described.

Table 5.13: Specific selected GMs based on linear and non-linear behaviour. The linear subset is based on the LAS whereas the non-linear subset is based on the HAS. Both subsets are a total of including 198 GMs. In the table are listed the loaf-factor (LF) as well as the response type (RT). The RT is either linear (L) or non-linear (N).

Linear Dataset (LDS)				Nonlinear Dataset (NDS)			
ID	GM Name	LF	RT	ID	GM Name	LF	RT
301	BIGBEAR-DHP090	0.5	L	602	BIGBEAR-DHP090	1.5	N
303	CAPEMEND-EUR090	0.5	L	604	CAPEMEND-EUR090	1.5	N
305	CAPEMEND-RIO270	0.5	L	606	CAPEMEND-RIO270	1.5	N
:	:	:	:	:	:	:	:
599	WHITTIER-A-PAS180	0.5	L	900	WHITTIER-A-PAS180	1.5	N
600	WHITTIER-A-SMA360	0.5	L	901	WHITTIER-A-SMA360	1.5	N

The two sets of either the linear load-set (LDS) or the non-linear load-set (NDS) specified in Table 5.13 are then the GMs related to the responses that are to be made into training and test-sets. There will then be four sets in total: two training- and two testing sets each including only responses related to the GMs in the LDS or the NDS. In the simulations that have been carried out for the present study, the GP is trained and tested upon 20 responses, which are listed in Table 5.14.

Table 5.14: Training and test sets that only includes accelerational responses related to the LDS and NDS. These sets are to be used with the GP.

Set label	Response IDs	Number of Responses
Train L	20 linear responses, excluding Test L related to LDS in Table 5.13.	20
Test L	453, 454, 456, 457, 458, 460, 461, 463, 464, 468 469, 471, 472, 473, 475, 477, 479, 481, 482, 483	20
Train N	20 non-linear responses, excluding Test N related to NDS in Table 5.13.	20
Test N	754, 755, 757, 758, 759, 761, 762, 764, 765, 769 770, 772, 773, 774, 776, 778, 780, 782, 783, 784	20

The responses in the linear test set and in the non-linear test set, are based on the same seismic event with a different load factor given for the GMs. In this way, the GP is going to be evaluated upon the signals related to GMs with the same overall characteristics but different amplitudes.

In order to evaluate the influence of the linear and non-linear classification in relation to the testing and training process for the GP performance, are the four different linear and non-linear subsets combined for a total of four cases presented in Table 5.15.

Table 5.15: Overview of the training and test sets used in the four cases for the GP predictions. The responses composing the sets are further based on the GMs in Table 5.14.

Case label	Train set	Test set	Input node	Output node
Case 7 (LL)	Train L	Test L	23	42
Case 8 (NL)	Train N	Test L	23	42
Case 9 (NN)	Train N	Test N	23	42
Case 10 (LN)	Train L	Test N	23	42

The integration of cases in which the GP is trained on linear and non-linear data-sets allows for the evaluation of the improvement, that a wider training set would bring to the performance of the model. The implementation of the simulations with test sets of linear and non-linear nature is useful to evaluate whether the improvement in the performance of the GP would affect all the responses, or only a specific category. Moreover, these simulations would also provide a better overview regarding the differences in the estimation of linear and non-linear responses. The final results are summarized in Figure 5.15 in terms of errors and TRAC measured for the 20 response signals that have been estimated in each of the four cases.

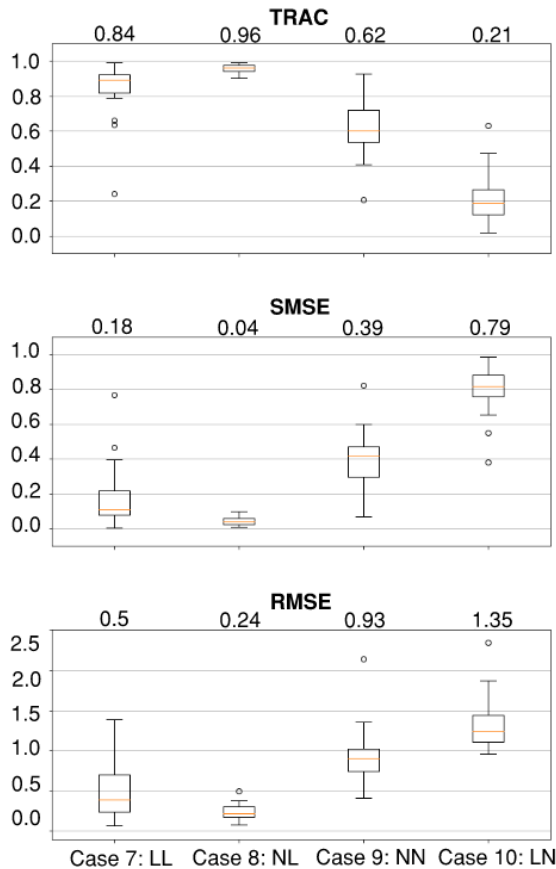


Figure 5.15: GP errors and TRAC value regarding the influence of the final structural state. The training and test sets used are listed in Table 5.15. The prediction were made for node 42 given the input for node 23.

Overall, the performance of the model improves, when the GP is trained on data similar to the predicted signals, instead of selecting random training data.

When predicting linear responses from non-linear inputs - i.e. Case 8: NL -, this results in the best performance with the lowest mean error measured and small variance. This might be due to the fact that the non-linear responses are associated with larger peaks cf. Figure 4.15, which therefore, include the smaller amplitudes by implication. This makes it possible for the model to have obtained information about a broader amplitude range, whereas the most extreme amplitudes are not to be used. For the remaining cases, the spread is seen to be much greater. On the contrary is Case 10: LN, which predicts non-linear responses from linear inputs, which have the

worst performance out of the four cases. This might be given due to the nature of linear and non-linear responses, but where the same argument with the amplitudes can be made in reverse.

When training upon linear responses, these are associated with lower PGAs. This means that when training the model, large amplitudes are not included, which makes it difficult for the model to predict these extreme amplitudes associated with the non-linear responses. This could also be the case seen in Figure 5.13, where the predictions are worse specifically when large accelerations occur, thus the training set has not included a sufficient number of accelerations with large enough amplitudes. This is especially important for the GP since only a small training set can be used.

This may indicate that even when the GP is trained and tested with only non-linear responses, the difference in the non-linear responses is still too large. The category of non-linear responses further covers a large range of energy-levels from 1.5 kNm and beyond. In order to see further improvements for the purely non-linear case, the category may have to be split into smaller sub-categories such that the energy-range is smaller for each non-linear class.

In conclusion, the GP would benefit from a larger training set, as the model would then be trained and exposed to a wider range of responses with varying final structural states including both linear and non-linear responses. This would greatly improve the prediction of the non-linear responses since the prediction of linear responses is sufficiently accurate in all the considered cases. These claims can be supported by comparing Case 9 and Case 10 where non-linear signals are predicted. Here the latter case, the GP is trained only upon linear responses and the errors are significantly higher than in the former case in which the model has been trained upon non-linear responses.

In general, the prediction of non-linear signals is challenging for the GP, which can be seen by the high error measures of both RMSE and SMSE in Cases 9 and 10, compared with the same errors in Cases 7 and 8.

CHAPTER 6

Results: Neural Network

In the following, both the overall assessment of the NN and the comparison with the GP are reported. The analyses performed for the overall assessment of the NN are analogous to those reported for the GP. However, the preliminary study that aims at the evaluation of different sensor layouts is carried out only for comparing the NN and the GP.

Hence, the considered input and output nodes' layout is the same as in the overall assessment of the GP: all the simulations made for the NN aim to estimate the acceleration signal in node 42 (third floor) given the signal at node 23 (first floor).

6.1 Overall assessment

The overall assessment of the NN is based on the estimation of the error and TRAC values introduced by the model when predicting the signals associated with the 301 SAS GMs all with a load-factor equal to 1. Since the NN can be trained on a larger amount of data, the evaluation is carried out through the K-fold cross-validation algorithm previously introduced. In the specific case of the presented NN, the technique is used by creating 10 folds therefore in each fold, 90 % of the data-set is used for training, while the remaining 10 % will be used for testing, hence predictions. As explained earlier, this technique is iterative thus, it provides the prediction of the entire data-set considered. The testing errors and TRAC values are reported in for each of the 10 folds.

Table 6.1: K-Fold validation results for NN: Testing errors and TRAC values for the predictions. The considered responses correspond to the 301 SAS GMs. For each fold, 90 % of the data has been used for training, where the remaining 10 % were used for predictions. The responses are estimated in node 42, given input responses for node 23.

Fold, i	RMSE	SMSE	TRAC
1	0.2273	0.0406	0.9614
2	0.3251	0.0503	0.9509
3	0.2701	0.0424	0.9593
4	0.3003	0.0507	0.9505
5	0.2865	0.0396	0.9622
6	0.2834	0.0512	0.9504
7	0.3947	0.0548	0.9469
8	0.3823	0.0611	0.9401
9	0.2615	0.0345	0.9683
10	0.3261	0.0560	0.9459
Mean	0.3057	0.0481	0.9536
STD	0.0498	0.0080	0.0083

In the table, the mean errors for all the 10 folds are listed. Since the number of signals in each fold is approximately the same, their mean value then corresponds to the generalized error, defined by Equation (2.24). Further, the standard deviations (STD) for each error are reported. The generalized error is based on the error measures for each individual fold. The distributions of all the errors for each fold are shown in the box-plots in Figure 6.1. Each box-plot is corresponding to one fold, representing the distribution of the errors obtained in predicting 10 % of the responses related to the SAS load-set. The last box-plot, seen on the right part of the figure, is the resultant for all the 10 folds. Therefore, it shows the distribution of the errors and TRAC relative to the estimation of all the 301 signals.

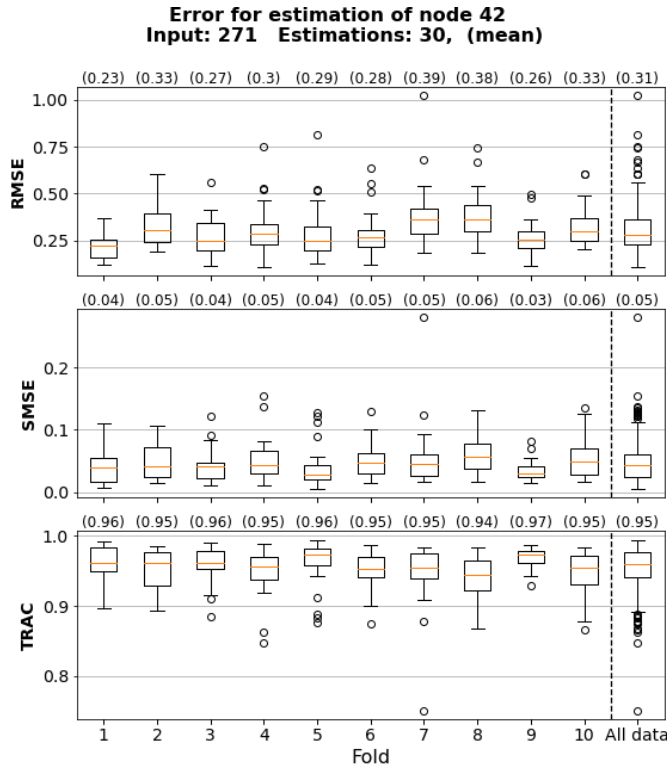


Figure 6.1: NN overall estimation: Box-plots of TRAC, SMSE and RMSE for each of the 10 K-folds. The responses are related to the SAS load-set with the box-plot furthest to the right, including all the 301 predictions. Input node: 23, output node: 42.

Figure 6.1 shows that the NN is able to predict most of the responses with an acceptable accuracy since the mean values of the errors are fairly low within the ranges of 0.23-0.39 and 0.04-0.06 for the RMSE and SMSE, respectively. This also results in a fairly low STD throughout the predictions. The box-plots seen in the figure are not deviating significantly from one fold to the next. This means that the NN generalizes well overall. Note that for each fold different responses are predicted, which may be the reason why the errors are different for each fold. But since the training data includes enough responses, the model has been trained with substantial variety to make up for this.

For completeness, it is interesting to show also the signals predicted from the NN in node 42 associated with the case studies of the GM41 CHICHI-TCU074-N and GM23 . Figure 6.2 illustrates the obtained results and the correspondent RMSE, SMSE and TRAC (reported also in Table 6.2).

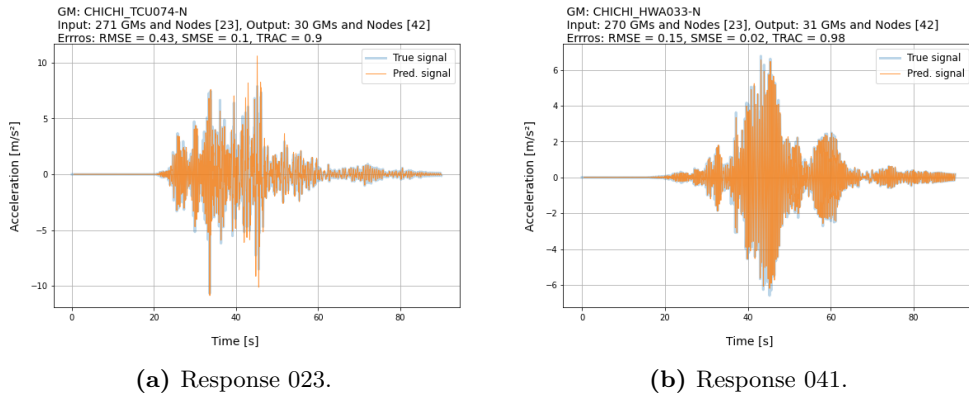


Figure 6.2: NN predictions for responses corresponding to GMs CHICHI-TCU074-N (ID 041) and CHICHI-HWA033-N (ID 023) - Input node: 23, output node: 42.

Table 6.2: Error and TRAC values for NN predicting signal in node 42, given input responses in nodes 23.

GM Name	Response ID	RMSE	SMSE	TRAC
CHICHI-TCU074-N	041	0.43	0.1	0.9
CHICHI-HWA033-N	023	0.15	0.02	0.98

6.1.1 Influence of the final structural damage state

The present analysis has been introduced in the assessment of the GP. In order to investigate whether the final damage state of the structure, the linearity or non-linearity of the predicted response has an influence also on the second ML model presented here, it has been reproduced for the NN.

The linear and non-linear data-sets used for this analysis have already been introduced and are the responses related to the GMs listed in Table 5.13. The reason for creating these data-sets was to be able to train and test the ML model only with responses categorized either as linear or non-linear. These data-sets are then based on the same ground motion recordings, but where two different load-factors have been utilized. For this reason, the characteristics of the excitations are the same, where the only difference is the scaling of the excitation.

Both of the load-sets, LDS and NDS, are then composed of 198 GMs each, with the training and testing sets being used in four cases specified in Table 5.15.

The same four cases will be used for the NN. However, since the NN has no limitation regarding the amount of training data, the training sets will include 178 responses,

while the test-sets stick to the 20 used also in the GP. By this measure, the NN is trained on a larger data-set than the GP, but both models predict the same responses. Also in the case of the NN is the K-fold scheme utilized which makes it possible for the NN to predict all the available responses. The K-fold is applied with 10 folds and the responses that are to be predicted in each fold are listed in Table G.1 and Table G.2 both found in Appendix G, based on the LDS and the NDS respectively. In the set K-fold, the NN will predict the same responses as the GP in fold number 6. The specific linear and non-linear data-sets for this 6th fold are listed in Table 6.3.

Table 6.3: Training and test sets for the K=6 fold for the NN. The predicted responses then matches the ones predicted for the GP.

Set label	Response IDs	Number of Responses
Train L	Remanding responses related to the LDS, listed in Table G.1. Excluding the test set Test L.	178
Test L	453, 454, 456, 457, 458, 460, 461, 463, 464, 468 469, 471, 472, 473, 475, 477, 479, 481, 482, 483	20
Train N	Remanding responses related to the NDS, listed in Table G.2. Excluding the test set Test N.	178
Test N	754, 755, 757, 758, 759, 761, 762, 764, 765, 769 770, 772, 773, 774, 776, 778, 780, 782, 783, 784	20

The four cases presented in Table 5.15 are then also to be carried out for the NN and labelled as Case 7.NN, 8.NN, 9.NN and 10.NN. Note that the 'NN' for all cases are referring to the Neural Network. In Table 6.4 are the mean errors for each fold listed. The generalized error is further evaluated in the last row of the table, considering all the 10 folds.

Table 6.4: K-Fold validation for NN for different state of input/output. In total 198 responses are used, which are all preset in both the linear and nonlinear state. Predictions of node 42 given input from node 23. The case of linear inputs and non-linear output is then referred to as (LN).

Fold <i>i</i>	Case 7.NN (LL)			Case 8.NN (LN)			Case 9.NN (NN)			Case 10.NN (NL)		
	RMSE	SMSE	TRAC	RMSE	SMSE	TRAC	RMSE	SMSE	TRAC	RMSE	SMSE	TRAC
1	0.1111	0.0234	0.9769	0.4140	0.1169	0.8926	0.3012	0.0601	0.9422	0.2142	0.0692	0.9426
2	0.1215	0.0153	0.9848	0.4937	0.1081	0.8952	0.3616	0.0557	0.9452	0.2661	0.0685	0.9429
3	0.1487	0.0184	0.9819	0.5347	0.1345	0.8702	0.3712	0.0639	0.9375	0.2932	0.0607	0.9467
4	0.1306	0.0210	0.9793	0.5092	0.1745	0.8327	0.3205	0.0680	0.9330	0.2231	0.0608	0.9502
5	0.1149	0.0113	0.9889	0.4718	0.0986	0.9039	0.3480	0.0505	0.9504	0.3059	0.0706	0.9424
6	0.1420	0.0173	0.9830	0.5289	0.1390	0.8643	0.3772	0.0669	0.9342	0.3024	0.0743	0.9403
7	0.1876	0.0215	0.9787	0.6509	0.1467	0.8586	0.4512	0.0686	0.9320	0.3339	0.0634	0.9460
8	0.1644	0.0197	0.9805	0.7087	0.1828	0.8374	0.4861	0.0850	0.9197	0.2928	0.0609	0.9503
9	0.1316	0.0142	0.9859	0.4865	0.0754	0.9255	0.4246	0.0545	0.9458	0.3157	0.0737	0.9360
10	0.1619	0.0316	0.9687	0.5547	0.1776	0.8333	0.4149	0.0994	0.9035	0.2685	0.0767	0.9292
Mean	0.1414	0.0194	0.9809	0.5353	0.1354	0.8714	0.3856	0.0673	0.9343	0.2816	0.0679	0.9427
STD	0.0232	0.0054	0.0053	0.0821	0.0343	0.0305	0.0551	0.0141	0.0132	0.0368	0.0058	0.0061

The standard deviations are relatively low for each fold, which indicates that the overall performance over the 10 folds generalizes well. For this reason, only one fold is further investigated, namely the 6th fold, since it has the same predicted responses as in the GP study. The box-plots corresponding to the 6th fold and for all the different cases are seen in Figure 6.3.

Overall, it can be observed that the error introduced in the predicted signals from the NN is lower when the training and the test sets are based on similar responses, i.e. Case 7.NN and Case 9.NN. As already noticed in the assessment of the GP, the estimation of linear responses given non-linear responses, the scaling-down of data points with higher accelerations to lower values, leads to acceptable error and TRAC values also in the case of the NN. The same cannot be stated for the nonlinear responses. When the estimation of non-linear responses is based on linear responses (Case 10.NN) the error values as well as their variance reach the maximum value over the presented four cases. It is observed again that in order to attain accurate estimations of nonlinear responses, a good representation of similar responses must be included in the training set. This is proved when considering the box-plot for Case 9.NN and comparing it with Case 7.NN. In the case of train-set and test-set including similar responses, the NN returns accurate estimations both for linear and non-linear responses. In the latter case, the mean values of the errors are slightly higher as well as their variance, thus, their estimation is still more difficult. However, the difference in terms of errors between all the presented cases is low. It must be further reminded that the non-linear responses represent a wider range of damage states (Minor, Moderate, Severe and Collapse).

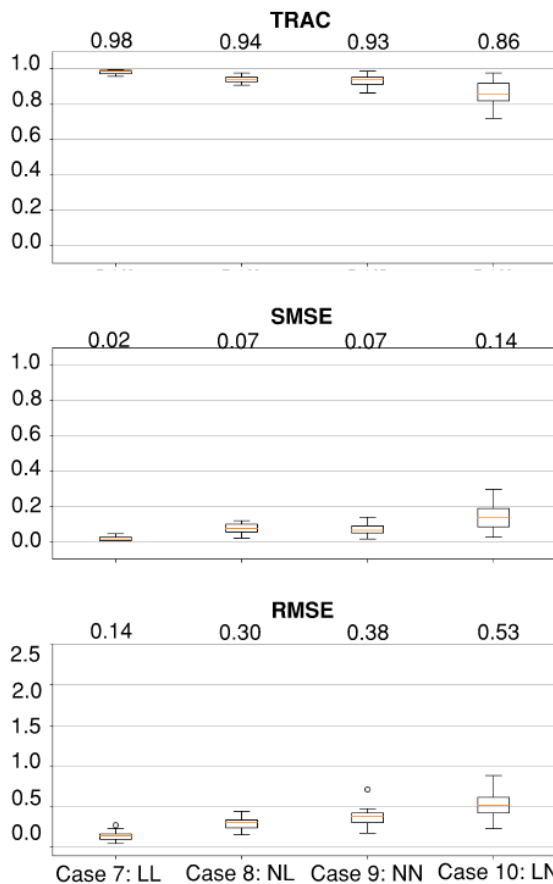


Figure 6.3: NN, errors and TRAC value box-plots: influence of the final structural state. 4 cases - input node: 23, output node: 42.

6.2 Comparison

From Section 5.2 and Section 6.1 the overall assessment of the two model-types have been investigated. In the case of the GP this includes how the model performed when training on a larger set, as well as the influence of linear and nonlinear training- and test sets. For the NN, the assessments have included the stability of the model using K-folds, as well as the influence of linear and non-linear training- and test sets. Since the two models are fairly different, the comparison between them is not trivial. For instance, the GP is limited to only include a small number of training data, because the kernel-matrix otherwise exceeds the computational power, whereas the NN

can include a much larger number of training data. With such a premise, it is interesting to compare the signals with IDs 041 and 023 estimated both by the GP and the NN in node 42. The predictions resulting from the former are shown in Figure 5.13 and Figure 5.14 while the results of the latter are reported in Figure 6.2. Here it seen that the NN is able to give a better prediction of the two signals in comparison to the GP. Especially for the response related to GM41, since the overall shape of the response relates to the true signal. The NN is then able to predict even the large acceleration amplitudes.

Given that both models have been investigated on the effects of linear and non-linear responses, this is a topic for comparison. The effects are seen in Figure 5.15 and Figure 6.3 for the GP and NN respectively, where the responses were predicted for node 42 given inputs from node 23 in both cases. The two investigations are performed using the same testing sets, such that the two models are predicting the same responses. However, the NN was trained on a larger training set of 178, whereas the GP was only trained from a sub-set of this with a number of 20.

For the NN, the overall errors seen in Figure 6.3 are much lower than the ones seen for the GP. This is most likely caused by the fact that the NN has a much larger training set. A large improvement has further been obtained in terms of the variance of the errors for all cases, since these have been reduced significantly in comparison with the GP.

The best performance for the NN is where linear responses are predicted based on linear - i.e. Case 7.NN. The worst performance still occurs for Case 10.NN.

A larger spread is seen for the non-linear predictions than for the linear predictions, which aligns with the observations made for the previous analyses in relation to the GP.

Since there is a disadvantage to the GP in relation to the size of the training set, the following comparison will try to even this disadvantage by using the same number of training responses for both models. Thus, the number of training responses and predictions will be the same for both models. This will in turn investigate if the NN needs a large training set in order to outperform the GP. If the GP then performs better in these two models under these circumstances, it might be possible for the GP to improve predictions to the same extent as the NN, when using training sets of equally large size.

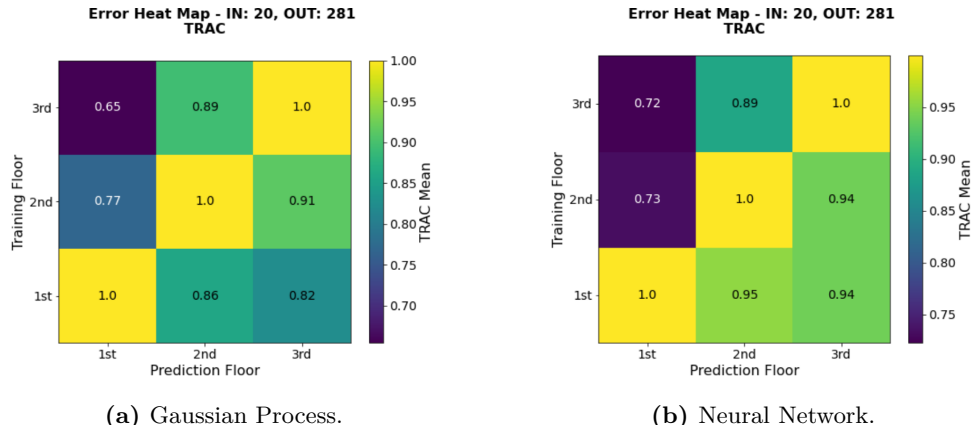
Due to the similar error estimations from nodes on the same floor, only one node for each floor is chosen to showcase the correspondent error measure. The training and test sets are the same for both the models and are listed in Table 6.5.

Table 6.5: Training and testing sets including responses based on the 301 GMs in the SAS.

Set label	Response IDs	Number of Responses
Training set	020, 030, 057, 068, 070, 079, 111, 136, 140, 144 161, 165, 173, 201, 236, 238, 239, 283, 289, 300	20
Testing set	Remaining, excluding the training set.	281

The mean TRAC error measures are seen in Figure 6.4 for both the GP and NN respectively. From the figure, it can be seen that the anti-diagonal is composed of all values of 1 for both models. This means that the given input from the same floor, the predictions are having the same shape as the true response, which was to be expected. However, in general, the NN is performing better than the GP with higher TRAC values, except when predicting responses on the 1st floor given inputs from the 2nd floor. In this case, the GP performs better.

The largest difference of TRAC occurs when predicting responses from the 1st floor given responses from the 3rd floor or when predicting responses on the 3rd floor based on responses from the 1st floor. These predictions should be the most difficult, since the prediction and input responses are located on different floors, with the largest vertical distance.



(a) Gaussian Process.

(b) Neural Network.

Figure 6.4: Mean TRAC measure for each floor, given one node to be used as input that is used to predict responses on a different or the same floor.

The same tendencies are generally true with the remaining error measures that can be found in Appendix H, where the NN is performing to the same extend or better than the GP. Both for the RMSE and SMSE the highest difference is also found when the predictions and input responses are furthest apart.

From the distributions of the error measures, which are also shown in Appendix H, it

can be seen that the spread of the distributions is also smaller for the NN. Meaning that the overall predictions are more concentrated.

This means that even with a relatively small training set the NN does perform at the same level or better than the GP. Especially the NN is able to make better predictions when the predictions and input responses are located on different floors. The performance may then increase when a larger training set is used, which the NN is capable of including.

When only considering the part until after the optimization, i.e. model initialization, training, and optimizing, the prediction phase is not included, there is a difference between the two models. When using the training set as listed in Table 6.5, the GP used an average of 12 minutes, compared to the NN using only 2 minutes. As a comparison, when the NN used a training set consisting of 812 responses the process took 12 minutes, only for the training phase. The NN is then able to process and optimize 40 times as much data, and still, it uses as much time as the GP. It is to be noted that these times are highly dependent on the software and hardware used to run and optimize these models. These times are simply to be used as an indication that the computational time in general is larger for the GP than for the NN. This denotes the scaling issues that are within the GP.

To summarize, the NN has equal or better performance than the GP when compared with the same training and testing sets, and at a faster computational time. Further, the NN is able to comprehend a larger amount of data, since there is not the same scaling problem as for the GP. Meaning that more diverse data can be used in order to train the model.

On the contrary, the GP provides probabilistic outputs such as mean and variance for the predictions, such that a credible interval can be obtained. The GP further gives the possibility to interpret the hyper-parameters in a physical sense. More knowledge is also to be provided by the user, since suitable kernel functions, or a combination of these, are to be selected in order to get satisfying predictions. Here the NN works as a 'black-box' and gives little to no physical interpretations or statistical outputs.

6.3 Noise

From the comparison between the GP and NN, it is found that the NN outperforms the GP both in terms of accuracy in predicting the responses and computational time. The NN is then to be investigated in relation to the addition of noise to the input responses.

Until now, the responses used as input and output for the models have all been without any noise. This means that these responses have been the true accelerations that the specific parts of the structure would have been experiencing. However, in reality, these acceleration responses are obtained using measurement equipment, meaning that some level of noise is present.

In this section noise is added to the input responses, to mimic that these are obtained using measurements of the true structure. No noise is added to the output responses - i.e. the predicted responses - since the predictions should be of the true response of the structure.

There are multiple ways to incorporate noise in the response signals such as adding noise as a percentage of the standard deviation (STD) of the signal or adding noise with a constant standard deviation independent of the original signal. However, given measuring equipment, such as accelerometers, it is not trivial to determine the related noise level given these methods.

An additional method is to use the Signal-to-Noise Ratio (SNR), where the noise ratios can be determined for measuring equipment given their noise density, which is often given in the technical declaration of the equipment. The method of the SNR has further been used in the literature to add noise to a response signal [49].

Even though these methods have different measures of noise, they all assume that the noise is given as Gaussian white noise with a zero-mean, thus, only characterized by a standard deviation. All three measures then have an equivalent standard deviation in terms of a Gaussian distribution.

In Figure 6.5 the three methods of noise are applied to a sine-wave with peak amplitude $A = 1$, and a total duration of 10 units of time. The noise levels for each method as well as their Equivalent Gaussian Standard deviations (EGS) are listed in Table 6.6.

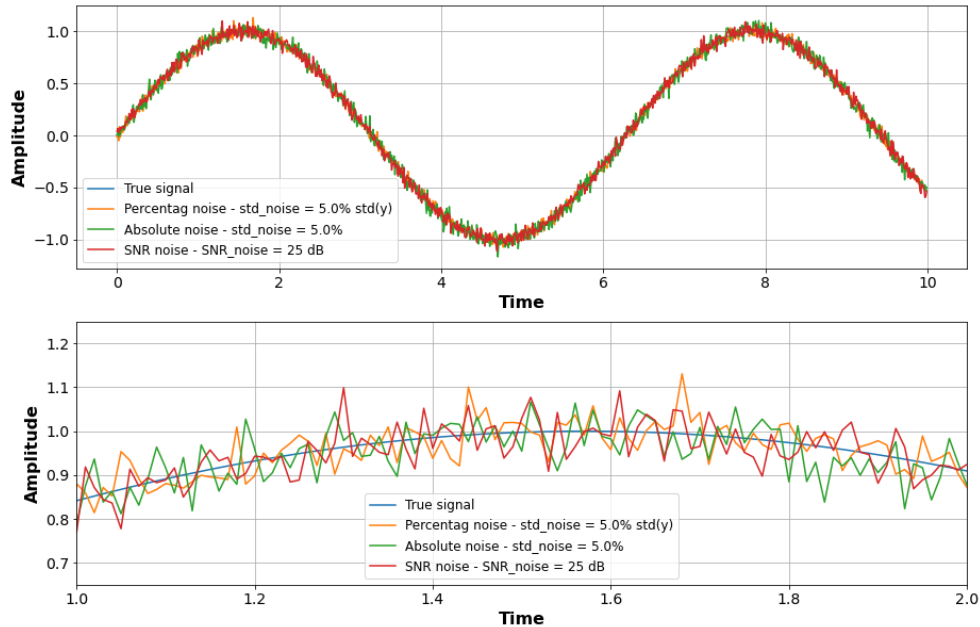


Figure 6.5: Different noise levels added to a sine-wave with peak amplitude $A = 1$. The noise levels are related to; 5% of the STD of the signal, a white noise with STD of 5%, and a SNR of 25 dB.

From the figure, it can be seen that even though the noise levels of the three methods are different, the EGSs are similar. This means that the added noise from the three methods is comparable. For the two methods of percentage and absolute standard deviation, the level of noise is the same and equal to 0.05. However, since one is defined as the percentage of the standard deviation of the signal, where the other is the applied standard deviation, the associated EGS are not the same for the two methods.

Note that the associated Gaussian STDs listed in Table 6.6 are specific to the case of a sine-wave with a peak amplitude of unity.

Table 6.6: Noise levels and Equivalent Gaussian Standard deviation (EGS). In accordance with Figure 6.5.

Method	Noise	EGS
Percentage of STD	0.05	0.03
Absolute STD	0.05	0.05
SNR	25 dB	0.04

Since the SNR method has a direct linkage with the characteristics of the sensor, this

method will be used in the following investigations, with noise ratios of 40 dB, 30 dB, and 20 dB added to the original signal, along with the true signal with no noise. The equivalent Gaussian standard deviation of these noise ratios is further listed in Table 6.7. Note that a noise ratio of low dB is associated with a larger standard deviation of the noise when compared to a noise ratio of high dB.

Table 6.7: Noise ratios and EGS that are to be used for the further analysis, using the SNR to define noise.

Method	SNR	EGS
SNR	No Noise	0.00
SNR	40 dB	0.01
SNR	30 dB	0.02
SNR	20 dB	0.07

6.3.1 Determining noise of equipment

The SNR is defined as the ratio between the Root-Mean-Square (RMS) value of the signal and of the noise. The SNR value can be given as a ratio in dB such as:

$$\text{SNR}_{\text{dB}} = 20 \log_{10} \left(\frac{S_{\text{RMS}}}{N_{\text{RMS}}} \right) , \quad \begin{cases} S_{\text{RMS}} = \frac{A_S}{\sqrt{2}} \\ N_{\text{RMS}} = \rho_N \sqrt{\text{BW}_N} \end{cases} \quad (6.1)$$

where S_{RMS} and N_{RMS} are the signal and noise RMS-values respectively. If it is assumed that the signal is given as a sinusoidal, the RMS-value is then determined based on the RMS peak amplitude, A_S . The RMS-value of the noise is determined as the product of the Noise density, ρ_N and the square root of the Noise equivalent bandwidth, BW_N . Often the noise density and bandwidth, or even the RMS noise value, are given in the technical specifications of the sensor.

In order to get an understanding of SNR, a number of commercially available accelerometers and their characteristics are investigated. The characteristics are available from the data-sheets of the sensors, from where the SNR can be determined using Equation (6.1). In Table 6.8 are listed several accelerometers along with their characteristics and associated SNR.

Table 6.8: Accelerometer characteristics and SNR obtained from their datasheets [5, 25, 2, 1].

Sensor Model	Noise Density ρ_N [$\mu\text{g}/\sqrt{\text{Hz}}$]	Bandwidth BW_N [Hz]	N_{RMS} [mg]	Range [g]	SNR _{dB}
LSM303DLHC	220	200	3.11	± 8	65
MPU-6000	400	10	1.26	± 2	61
DYTRAN-3211A2	-	-	0.10	± 50	111
ADXL206	110	160	1.39	± 5	68
A/1800/V	4.8	10	0.02	± 0.5	87

Note that the SNR-values that are associated with the commercial accelerometers are much higher than the ones to be used in the further analysis given in Table 6.7. This means that the imposed noise levels would be lower since they are associated with a larger STD than experienced from the commercial accelerometers, which makes the investigations conservative.

6.3.2 Influence of noise on predictions

The noise is assumed to have the characteristics of white Gaussian noise, with a zero-mean value, such that it's only defined by its standard deviation. The standard deviation can be determined using the SNR as well as the signal on which the noise is to be applied. The true signals are obtained as the acceleration responses from the FE model.

The SNR in dBs is estimated using the ratio between the power of the signal, P_S and the power of the noise, P_N . In this case, P_R refer to the average power for a given response R , i.e. the mean square¹ of R such that $P_R = \text{E} [R^2]$.

$$\text{SNR}_{\text{dB}} = 10 \log_{10} \left(\frac{\text{E} [S^2]}{\text{E} [N^2]} \right) = 10 \log_{10} (\text{E} [S^2]) - 10 \log_{10} (\text{E} [N^2]) \quad (6.2)$$

From Equation (6.2) is given the formulation of how the SNR in dB is determined, using two terms. One term is related to the known true signal S whereas the other is associated with the unknown noise N . Since the SNR is known, the only unknown is the term involving the noise. Further, since the mean value of the noise is zero, the mean square simply denotes the variance which is the square of the noise standard deviation. This standard deviation is then to be used in order to apply a Gaussian white noise to the true signal.

¹Note that the mean square is equal to the sum of the variance and mean squared such that: $\text{E} [R^2] = \text{Var} [R] + (\text{E} [R])^2$, which is derived from the definition of the variance.

Now that the noise ratios as well as how these ratios are applied to the signal have been determined, the NN can be used to predict noise-free signals given inputs with varying SNRs. It is only the input accelerations that are affected by noise, where the predicted outputs are noise-free. The same NN framework is to be used as in previous predictions, meaning that the NN does not know the level of noise that the inputs are affected by. Only signals with the same amount of noise are used as inputs, meaning that all inputs have the same noise ratios, which are either: no noise, 40 dB, 30 dB, or 20 dB.

A K-fold scheme is to be used together with the total number of 903 responses associated with the GMs in SAS, LAS, and HAS load-sets. The K-fold then allows for predicting all 903 responses, based on different subsets of training and testing sets. In total are 10 folds to be used, thus the number of training responses is either 812 or 813 and the number of prediction responses is 91 or 90. This means that 90% of the responses are to be used in the training phase, whereas the prediction phase uses the remaining 10%. The model is inputted with responses from node 23 as input in order to predict responses in node 42. In Table 6.9 are the error-measures from each fold listed, alongside the mean and standard deviation for each noise ratio.

Table 6.9: K-Fold validation for NN with different SNRs. Predictions of responses in node 42 given input from node 23. A total of 903 responses have been utilized related to the GMs in the SAS, LAS, and HAS load-sets.

Fold <i>i</i>	No noise			40 dB			30 dB			20 dB		
	RMSE	SMSE	TRAC	RMSE	SMSE	TRAC	RMSE	SMSE	TRAC	RMSE	SMSE	TRAC
1	0.2764	0.0443	0.9571	0.2801	0.0455	0.9559	0.2776	0.0444	0.9567	0.2977	0.0505	0.9505
2	0.2906	0.0455	0.9555	0.2935	0.0466	0.9546	0.2937	0.0463	0.9547	0.3189	0.0540	0.9469
3	0.3430	0.0468	0.9543	0.3537	0.0497	0.9514	0.3464	0.0478	0.9531	0.3771	0.0560	0.9450
4	0.2403	0.0460	0.9561	0.2265	0.0412	0.9604	0.2271	0.0412	0.9602	0.2405	0.0454	0.9555
5	0.1975	0.0342	0.9677	0.1810	0.0280	0.9728	0.1926	0.0316	0.9697	0.2025	0.0346	0.9657
6	0.2248	0.0320	0.9692	0.2373	0.0357	0.9661	0.2306	0.0334	0.9682	0.2503	0.0384	0.9623
7	0.2325	0.0494	0.9522	0.2298	0.0484	0.9538	0.2407	0.052	0.9498	0.2493	0.0550	0.9466
8	0.3722	0.0648	0.9362	0.3737	0.0654	0.9356	0.3801	0.0675	0.9336	0.4062	0.0764	0.9249
9	0.4422	0.0794	0.9245	0.4451	0.0806	0.9238	0.4488	0.0819	0.9227	0.4604	0.0849	0.9193
10	0.4313	0.0802	0.9222	0.4319	0.0803	0.9222	0.4327	0.0804	0.9223	0.4520	0.0861	0.9162
Mean	0.3051	0.0523	0.9495	0.3053	0.0521	0.9497	0.3070	0.0526	0.9491	0.3255	0.0581	0.9433
STD	0.0832	0.0161	0.0156	0.0868	0.0169	0.0162	0.0858	0.0171	0.0164	0.0883	0.0174	0.0166

It can generally be seen from the table that the mean value for each type of error becomes higher with a decrease of SNR. This is as expected since a noise ratio of 20 dB is having a larger standard deviation with respect to a noise ratio of 40 dB. This means that the larger the standard deviation in the added noise, the worse the general predictions. However, note that the error-measure only changes slightly. For instance, the mean RMSE error has a relative change of 6.69% between the case of no noise and the case of maximal noise of 20 dB. The standard deviation for the same two cases has a relative change of 6.13%. The relative change between a given SNR

and no noise is listed in Table 6.10. Here, a positive value indicates that the numeric value of the error has increased whereas the opposite is true for negative values.

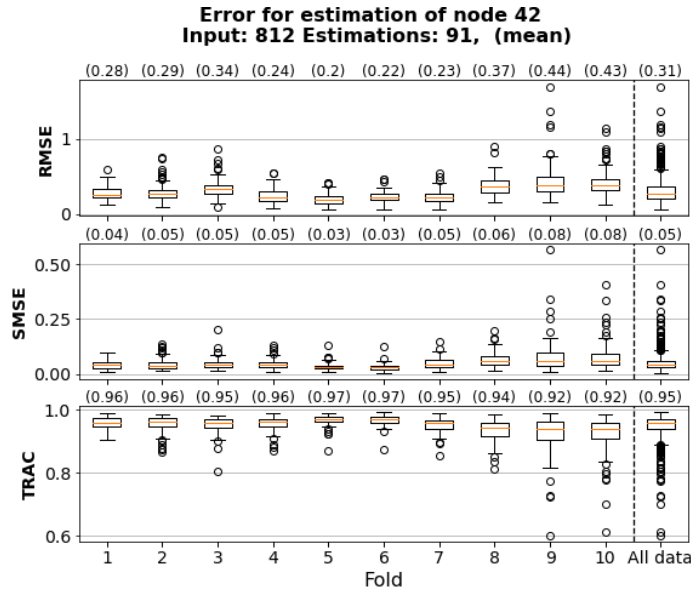
Table 6.10: Relative change in mean error and standard deviation error between a given SNR and the case with no noise from Table 6.9. All values are given as a percentage.

	No noise			40 dB			30 dB			20 dB		
	RMSE	SMSE	TRAC	RMSE	SMSE	TRAC	RMSE	SMSE	TRAC	RMSE	SMSE	TRAC
Δ_{rel} Mean	0.00	0.00	0.00	0.07	-0.38	0.02	0.62	0.57	-0.04	6.69	11.09	-0.65
Δ_{rel} STD	0.00	0.00	0.00	4.33	4.97	3.85	3.13	6.21	5.13	6.13	8.07	6.41

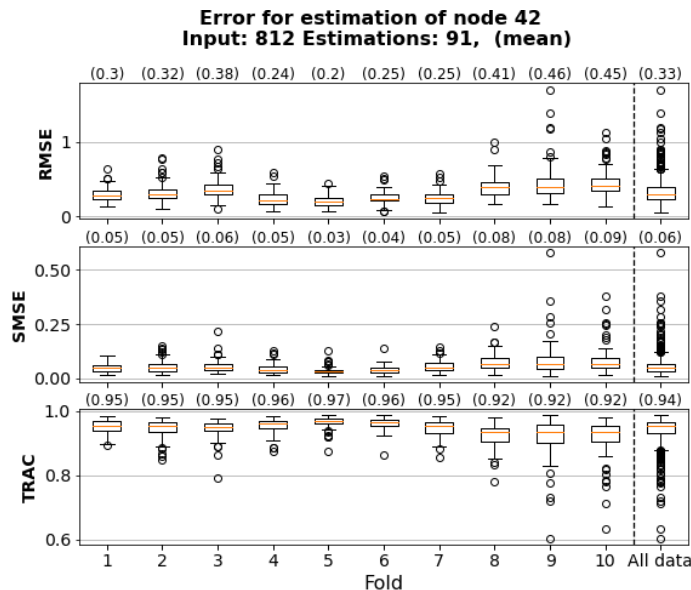
The standard deviations are seen to generally increase as well, with the largest deviations associated with the largest noise. The addition of noise does have a minor influence with a maximal change in the mean error of 11.09%, in relation to SMSE between the case of no noise and a noise ratio of 20 dB.

In Figure 6.6 are the distributions of the errors for each fold in the two cases of no noise and a noise ratio of 20 dB. The mean values are associated with Table 6.9. These distributions are used to showcase how the overall performance of the error-measures, and not only be a mean value. It can here be seen that the overall error-values are centred around the median, with some 'outliers', which are predicted worse than the rest of the predictions. Here it can be seen that a larger number of outliers are present. In general, it can be seen that the distributions of the predictions are fairly comparable, meaning that the models are generalizing well. The same can be said for the distributions of all the noise ratios. The remaining distributions are seen in Appendix I.

Note that for each fold, different ground motions are predicted, such that none of the folds contains the same predictions. This can also have an influence on why some folds are predicted worse than others.



(a) Noise ratio: No Noise.



(b) Noise ratio: 20 dB.

Figure 6.6: Distributions of error for each fold, using the NN model to predict responses with various noise ratios SNR. Predictions of node 42 given input from node 23.

CHAPTER 7

Conclusion & Further studies

7.1 Summary

The main objective of the project was to estimate the state of a given structure. Here, state estimation has been done in terms of the prediction of the acceleration responses in one part of the structure by knowing acceleration time histories recorded at different locations. This suggests that the structural responses are measured in one part of the structure by means of sensors, where the correspondent signals at different locations are of interest. Machine learning has been utilized in order to make these predictions, especially the two methods of a Gaussian Process, and a Neural Network has been used. The acceleration histories in the structural nodes have been obtained using a Finite Element model, where the structure has been excited with 903 different strong ground motions in the form of ground accelerations. From this variety of ground motion excitation, the associated responses have been categorized as either linear or non-linear based on the global energy dissipated from the structure. The characterizations were made based on the relation between the global energy and the maximal inter-story drift since the latter is associated with different damage states. Here, the responses in the non-linear category are associated with permanent deformations for the structure.

In general, the two models have been investigated in terms of their performance, and under which conditions they make the best estimations. These investigations have included the location of the response predictions, the number and location of the known responses used for the predictions, as well as how noise in the known input signals affects the predicted noise-free responses. The performance of these models has been evaluated in relation to the difference between the estimated and the true time histories, which is defined through error and similarity measures including RMSE, SMSE, and TRAC.

7.2 Discussion

For the Gaussian Process, it has been seen that the optimization of the hyper-parameters makes the predictions much more accurate. It has especially been shown that the responses in the form of accelerations are the most relevant if these are obtained from the same floor of the frame structure. The optimization makes this clear, since only the signals recorded on the same floor as where the prediction is to be made, have an optimized scaling-factor different from zero. The remaining zero-terms are then not considered when making a prediction. This holds also when the physical distance between the prediction and the given response on the same floor is relatively large compared to the dimensions of the structure. This may be implicitly caused by the choice of using a frame structure, where each floor moves together, meaning that the acceleration histories at a given floor are more similar than when compared to signals on other floors.

This was further seen in Section 5.1.4 Case 4, where the GP was to estimate a response given an input only from a different floor. In this case, the predictions were not as accurate as in Case 3, where the predicted and input responses were located on the same floor. The same tendencies were shown also in the last study proposed in the Preliminary Analyses (Section 5.1). In that study, the GP was predicting 296 responses considering all the possible combinations of input and output nodes Section 5.1.5. The mean error and TRAC values showcased that what has been observed in the examples preceding this study is true also for the general case of 296 motions as well.

In Section 5.2 it was seen that when taking a random sample of training data including either 5 or 20 responses, the accuracy of the GP in predicting the same test-set of responses does not differ significantly. It was further noticed that the GP had more difficulties when predicting responses with higher acceleration amplitudes. This was further investigated when taking into account the linearity or non-linearity of the responses which corresponds to the non-presence or presence of damage in the structure. As mentioned earlier, the linear responses are associated with relatively small PGAs, whereas the non-linear responses are associated with responses with larger PGAs. This means the GP is very susceptible in relation to the specific training set. This is in fact one of the drawbacks of the GP, since it does not handle the scaling of training sets very well. This means that when predicting a response with large amplitudes, the training data must also include responses where large amplitudes are present. The selection of the training set then becomes of much importance given that the GP cannot incorporate a large training set.

The scaling issue with the GP is grounded in the kernel matrix, which includes all information about the training data. Methods have been proposed in order to approximate or simplify this matrix, in order to reduce the computational time and thus make the model work with larger data-sets [59]. Other solutions may to be reduce

the input dimension, or only to use specific areas of the original kernel matrix. In this way can the probabilistic outputs of the GP be provided.

This is an obstacle that the Neural Network overcomes since it scales well and is therefore able to train on a much larger training set. The selection of an appropriate training set then becomes less important, as long as the NN is trained on enough data that includes both small and large acceleration amplitudes. The results seen in Section 6.1 prove that the NN generalizes well since the general errors for each of the 10 folds were fairly similar with low standard deviations. The same investigation in relation to the linear and non-linear input and prediction responses was made for the GP, with similar results. However, the NN was able to make better predictions in general.

In order to make a fair comparison between the two models, a specific analysis was created where the GP and NN were both trained and tested on exactly the same training and testing sets. This means that both the NN and the GP were trained only on responses associated with 20 ground motions. However, even here the NN was able to perform at the same level or better than the GP. The NN could then make further improvements on these initial predictions when the amount of training data was increased.

Since, in the specific case of the present project, the NN has proved to be the model with the best performance, the last analysis tries to take into account also the noise of the recorded signals. Here it was seen that, with a larger amount of noise added to only the input responses, the noise-free predictions got slightly worse. Therefore, the NN was still able to provide accurate predictions and did not outperform the GP in terms of scale-ability, computational time, as well as prediction accuracy.

7.3 Further Work

The performed investigations originate in the FE model, where the software OpenSees was used. One structure has been investigated, meaning that the findings of this report are only valid for this type of structure. The structure in question was a three-bay, three-storey reinforced concrete frame structure. The reinforced concrete material was modelled using non-linear material properties, in order for the structure to experience non-linear behaviour given the ground motions available. Other materials, such as steel or wood, or a combination of different materials would be of interest to investigate since these are often the true materials used in civil structures. Further, different structural geometries could be investigated, in order to show if the proposed methods generalize in terms of different structural systems. This has for instance been investigated by Ngueyen et. al. [57] where an ML model was trained for several steel structures with different geometries. The model was then able to use the spectral acceleration of the load, and the natural periods of the structure to

predict the damaged state of the structure.

The ground motions applied on the structure were then to be classified as either linear or non-linear based on a threshold of the global energy dissipation that has been determined in relation to damage states - i.e. maximum inter-storey drift. Here, the global energy was estimated based on the roof displacement and the total base shear force, at the support of the structure. The reason why the non-linearity measure was to be included, is due to the fact that an element in the non-linear regime has undergone permanent deformation, which could be an indication of damage. However, since the estimation was made for the whole structure, certain structural elements could be in the non-linear regime, but the structure as a whole may still be classified as linear for the given ground excitation. This would be the case if only a small amount of structural elements, such as the columns on the lowest floors, have reached non-linear behaviour, but where the majority of the elements are still behaving linearly. The described scenario may be the reason why in the present report, low-energy ground motions are associated with high PGAs. On the other hand, the ground motions with a large global energy dissipation are only related to responses with relatively large PGAs, meaning that about the entirety of the structural elements are in the non-linear regime.

Under the described premises, additional approaches could be used to assess the individual structural elements and detect the location of the non-linearity and its severity. This can be achieved by the evaluation of the local energy dissipation which is analogous to the global energy but the displacements and forces are replaced by rotations and moments [61]. Furthermore, a valid alternative to the global dissipated energy in the identification of the state of the structure could be the evaluation of dynamic properties such as the structural natural frequencies. These are estimated in the present report only before the dynamic analyses for the initial state. If these were to be estimated after or during the dynamic analyses, the difference in relation to the initial state could be assessed. A difference could then indicate that the structure has changed properties and that permanent damages may be present. Other measures, such as the residual inter-story drift or even damage indexes such as the Park-Ang index, could be used to classify the state of the structure and/or the individual elements. Two formulations of the Park-And index have been indeed defined: one for the global assessment of the structure and another one for the individual structural elements [61].

The procedure involving the ML consisted of using responses in the form of accelerations as both input and output for the models. The acceleration signals were chosen since these are quantity measurable on real structures using accelerometers, which is a common practice in structural assessments. In this report, the procedure of estimating acceleration time histories given data of the same typology has been shown to be possible using the machine learning models of GP and NN.

The utilization of other input and output quantities, however, could be investigated. If the purpose of the models is to use real measurements of a structure as inputs, realistic alternatives would include displacements, velocities, or strains, which are other common data recorded on civil structures. A combination of these could also be used as inputs, for instance, both acceleration and strain to provide the ML model with more information about the structure. Moreover, noise may be another input that could be introduced as an additional variable to the acceleration. If the model knows the noise level associated with a given instrument, the predictions may be able to take this into account, in order to make more reliable predictions. Regarding the output, ML offers broader flexibility. The output of the model does not have to be a measurable quantity of the real structure. In the case of supervised learning, it is of essential importance that the output corresponds to a quantity that can be recorded at least from a FE simulation¹. Furthermore, the output doesn't need to be a function over time, as for the predicted acceleration in this project. Alternative outputs could be everything: from displacements, moments, curvatures, and forces to global and local damage indices. This may be an advantage of the application of ML since the output may include measures that are difficult to obtain by other methods, but which are essential to indicate the damaged state of the structure.

The damaged state of the structure could especially be of interest. This could be used to predict the damage location and severity - e.g. structural elements, or the state of the entire structure, after an earthquake event. In this way, both the damages and the residual capacity of the structure to withstand future events could be assessed. Hence, this would be of extreme importance for the evaluation of the lifetime of structures, especially for structures that are remote such as offshore structures. The prediction of the state could then be used as a preliminary investigation, to inform whether repairs are needed and in which capacity. Structures such as bridges or tunnels could also be subjected to such type of monitoring.

With the ML being able to predict different outputs, the type of model could also be changed. In this report, only relatively simple models have been used. For the Gaussian Process, a sum-kernel was used since the inputs and outputs were all the same type of response - i.e. accelerations. The kernel-matrix itself could be approximated such that the process would be able to consider larger data-sets, while also providing uncertainty estimations to the predictions. For this report, the basic feed-forward architecture has been used for the Neural Network. It proved to give good predictions of the acceleration responses of the structure, using only one hidden layer with 20 neurons. More advanced architecture could be used with a larger number of hidden layers, combined with linear or nonlinear layers. The usage of a Convolutional Neural Network (CNN), could further be explored since these models have proved to make

¹A ML problem is defined as supervised learning when, in the training phase, the model takes the input x with the correspondent real output y . In this way, it is possible to compare the predicted signal $\hat{y}(x)$ with the provided real signal $y(x)$ and adjust the model settings - i.e. the model is learning.

good predictions of various time-varying signals [67, 38].

7.4 Conclusion

The usage of accelerational responses as inputs, in order to predict responses of a frame structure has been proved to be possible in this thesis. This is true when using the frameworks of a Gaussian Process as well as a Neural Network.

The responses were estimated for a reinforced concrete structure, which was used as the basis of the investigations. Preliminary analyses were performed for the structure in order to define dynamic properties such as the natural frequencies which were used to define the overall damping of the structure. Due to the nature of the frame structure, the responses that were located on the same floor were similar, to such an extent, that when an input response was taken from the same floor as a prediction, the accuracy of the prediction was higher. This is in relation to when the input response was given for a different floor than from where the prediction was to be made.

Such an aspect was showcased for the GP by only one scaling-factor being different from zero after optimization. The remaining terms in the sum-kernel all resulted in scales-factors equal to zero, thus not used when making new predictions. The GP further showed difficulty with predicting responses with high acceleration amplitudes when selecting a random training set with 5 or 20 responses. This was seen as an increase in the associated standard deviation of the errors' distributions associated with approximately 281 predicted responses. This aspect was further investigated and the signals with higher amplitudes were then shown to be more accurate when taking into account the structural state of the responses either being linear or non-linear. Since the GP does not scale well in terms of training data, it was then shown that when responses with large amplitudes are to be predicted, the GP must be trained with data that includes responses with similar amplitudes. However, when predicting responses with low amplitudes, the training data could include amplitudes with varying intensity. This makes the selection of training data a crucial step of the GP.

Analogous investigations were performed for the NN, which scales well in terms of training data. The model is then able to include more data, therefore, the selection of the training set results of less importance in the application of the NN. As long as the training set includes enough data, the NN is able to predict the responses with acceptable margins of error.

Overall, the NN outperformed the GP both in terms of accuracy as well as in computational time. Even when the two models were trained on the same data, the NN performed at the same level or better than the GP, and at a faster rate. This further shows that the NN does not necessarily need a large amount of training data in order

to make better predictions than the GP. The last study was intended to evaluate the performance of the outperforming model when noise was added to the recorded signals that were used to make the signals' predictions. Therefore, the noise was added to the training data of the NN, from where it resulted that the model was able to estimate responses with a marginal loss in accuracy.

In conclusion, although the error introduced in the predictions of high-amplitude acceleration signals remains relatively high, the Gaussian Process has proved suitable for predicting acceleration time histories. This is supported by the fact that the estimation of signals, which are not characterized by high amplitudes, is completed with sufficient accuracy. Its poor performance related to high-amplitude signals is due to the fact that the model does not scale well in terms of dimensionality, thus, it cannot be trained with larger data-sets. Such a limitation could be addressed through techniques that aim at the reduction of computational complexity. On the other hand, since the Neural Network is suitable to work with large data-sets, it returns accurate predictions in all the presented applications. Furthermore, the two models differ in the returned output. In order to use a Gaussian Process, prior knowledge of the data is required and used by defining distributions over functions. Yet, the Gaussian Process returns also uncertainty outputs in the form of mean and standard deviation related to the prediction. Regarding the Neural Networks, little to no knowledge about the underlying process is used. Therefore, Neural Networks consider a unique underlying function that returns only the prediction.

References

- [1] A1800. <https://www.djbinstruments.com/products/piezoelectric-accelerometers/monoaxial-iepe/view/Micro-g-Piezo-Tronic-IEPE-Accelerometer-A1800>. Accessed: 2023-01-02 (cited on page 106).
- [2] ADXL206. <https://www.analog.com/en/products/adxl206.html?doc=ADXL206.pdf#product-overview>. Accessed: 2023-01-02 (cited on page 106).
- [3] AK Agrawal and M Amjadian. “Seismic component devices.” In: *Innovative bridge design handbook*. Elsevier, 2016, pages 531–553 (cited on page 131).
- [4] Jimmy Xu Allan Bower. *Introduction to Dynamics and Vibrations*. https://www.brown.edu/Departments/Engineering/Courses/En4/Notes/vibrations_free_damped/vibrations_free_damped.htm. Accessed: 2020-05-31. 2018 (cited on page 26).
- [5] Juan Alvarez, Diego Alvarez, and Antonio Lopez. “Accelerometry-Based Distance Estimation for Ambulatory Human Motion Analysis.” In: *Sensors* 18 (December 2018), page 4441. DOI: 10.3390/s18124441 (cited on page 106).
- [6] Analysis Commands. <https://openseespydoc.readthedocs.io/en/latest/src/analysiscmds.html>. Accessed: 2023-01-02 (cited on page 139).
- [7] Abdelhamid Charif. “Flexural Behavior of Beams Reinforced with Steel Bars Exceeding the Nominal Yield Strength.” In: *Latin American Journal of Solids and Structures* 13 (May 2016), pages 945–963. DOI: 10.1590/1679-78251683 (cited on page 42).
- [8] Chaulagain et al. “Seismic response of current RC buildings in Kathmandu Valley.” In: *Structural Engineering and Mechanics* 53(4) (2015), pages 791–818. URL: <https://doi.org/10.12989/SEM.2015.53.4.791> (cited on page 61).
- [9] Brian Chiou et al. “NGA Project Strong-Motion Database.” In: *Earthquake Spectra* 24.1 (2008), pages 23–44. DOI: 10.1193/1.2894831. eprint: <https://doi.org/10.1193/1.2894831>. URL: <https://doi.org/10.1193/1.2894831> (cited on page 50).
- [10] Anil K. Chopra. *Dynamics of Structures*. Pearson, 2011 (cited on page 65).
- [11] American Society of Civil Engineers (ASCE). “FEMA 356 Prestandard and Commentary for the Seismic Rehabilitation of Building.” In: *Rehabilitation* 221 (2000) (cited on page 60).

- [12] European Committee et al. “EN 1992-1-1 Eurocode 2: Design of Concrete Structures—Part 1-1: General Rules and Rules for Buildings.” In: *European Committee: Brussels, Belgium* (2005) (cited on page 45).
- [13] *Concrete02 Material – Linear Tension Softening.* https://opensees.berkeley.edu/wiki/index.php/Concrete02_Material_--_Linear_Tension_Softening. Accessed: 2023-01-02 (cited on pages 41, 43).
- [14] Giorgio Corani, Alessio Benavoli, and Marco Zaffalon. “Time series forecasting with Gaussian Processes needs priors.” In: *Joint European Conference on Machine Learning and Knowledge Discovery in Databases*. Springer. 2021, pages 103–117 (cited on page 13).
- [15] Building Seismic Safety Council. *FEMA 273–NEHRP Guidelines For The Seismic Rehabilitations Of Buildings*. 1997 (cited on page 60).
- [16] Cristian Cruz and Eduardo Miranda. “Evaluation of the Rayleigh damping model for buildings.” In: *Engineering Structures* 138 (2017), pages 324–336 (cited on page 30).
- [17] Jingpei Dan et al. “Global bridge damage detection using multi-sensor data based on optimized functional echo state networks.” In: *Structural Health Monitoring* 20.4 (2021), pages 1924–1937. DOI: 10.1177/1475921720948206. URL: <https://doi.org/10.1177/1475921720948206> (cited on page 2).
- [18] Hung V. Dang et al. “Deep learning-based detection of structural damage using time-series data.” In: *Structure and Infrastructure Engineering* 17.11 (2021), pages 1474–1493. DOI: 10.1080/15732479.2020.1815225 (cited on page 2).
- [19] Ismail Derbal et al. “Neural network-based prediction of ground time history responses.” In: *European Journal of Environmental and Civil Engineering*, 24:1 (2020), pages 123–140. DOI: 10.1080/19648189.2017.1367727 (cited on pages 19, 20).
- [20] Chuong B Do and Honglak Lee. “Gaussian processes.” In: *Stanford University, Stanford, CA, accessed Dec 5* (2007), page 2017 (cited on pages 11, 12, 14, 15).
- [21] Wenqi Du. “An empirical model for the mean period (T_m) of ground motions using the NGA-West2 database.” In: *Bulletin of Earthquake Engineering* 15.7 (2017), pages 2673–2693 (cited on page 52).
- [22] David Duvenaud. “Automatic model construction with Gaussian processes.” PhD thesis. University of Cambridge, 2014 (cited on page 12).
- [23] *Eigen command.* <https://openseespydoc.readthedocs.io/en/latest/src/eigen.html>. Accessed: 2023-01-02 (cited on page 47).
- [24] *Ex9e, Fiber Section: Reinforced Concrete Section – Rectangular Section.* https://opensees.berkeley.edu/wiki/index.php/OpenSees_Example_9._Build_%26_Analyze_a_Section_Example. Accessed: 2023-01-02 (cited on page 136).

- [25] *Examining the Dynamic Range of Your Controller.* <https://vibrationresearch.com/resources/examining-the-dynamic-range-of-your-controller/>. Accessed: 2023-01-02 (cited on page 106).
- [26] G. L. Fenves F. McKenna and M. H. Scott. *Open System for Earthquake Engineering Simulation. University of California, Berkeley.* <http://opensees.berkeley.edu>. Accessed: 2023-01-02. 2000 (cited on page 37).
- [27] Charles Ferrar and Keith Worden. *Structural Health Monitoring : A Machine Learning Perspective.* Chichester West Sussex U.K: Wiley, 2012. DOI: 10.1002/9781118443118 (cited on pages 1, 2).
- [28] *Fiber Section.* https://opensees.berkeley.edu/wiki/index.php/Fiber_Section. Accessed: 2023-01-02 (cited on page 40).
- [29] *Force-based beam-column element.* https://opensees.berkeley.edu/wiki/index.php/Force-Based_Beam-Column_Element. Accessed: 2023-01-02 (cited on page 38).
- [30] *Geometric Transformation Command.* https://opensees.berkeley.edu/wiki/index.php/Geometric_Transformation_Command. Accessed: 2023-01-02 (cited on page 39).
- [31] Ahmed Ghobarah. “Performance-based design in earthquake engineering: state of development.” In: *Engineering structures* 23.8 (2001), pages 878–884 (cited on page 61).
- [32] Ian Goodfellow, Yoshua Bengio, and Aaron Courville. *Deep Learning.* <http://www.deeplearningbook.org>. MIT Press, 2016 (cited on page 17).
- [33] Ian Goodfellow, Yoshua Bengio, and Aaron Courville. *Deep Learning.* MIT Press, 2016 (cited on page 21).
- [34] Jochen Görtler, Rebecca Kehlbeck, and Oliver Deussen. “A Visual Exploration of Gaussian Processes.” In: *Distill* (2019). <https://distill.pub/2019/visual-exploration-gaussian-processes>. DOI: 10.23915/distill.00017 (cited on page 13).
- [35] GPy. *GPy: A Gaussian process framework in python.* <http://github.com/SheffieldML/GPy>. since 2012 (cited on page 16).
- [36] *GPy Models package.* <https://gpy.readthedocs.io/en/deploy/GPy.models.html#id31>. Accessed: 2023-01-02 (cited on page 16).
- [37] P Hamidian, Y J Soofi, and Bitaraf M. “A comparative machine learning approach for entropy-based damage detection using output-only correlation signal.” In: *J Civil Struct Health Monit* 2 (2022), pages 975–990. DOI: <https://doi.org/10.1007/s13349-022-00587-z> (cited on page 2).
- [38] Yingying He et al. “A framework of structural damage detection for civil structures using fast fourier transform and deep convolutional neural networks.” In: *Applied Sciences* 11.19 (2021), page 9345 (cited on page 116).
- [39] Christoph Heinemeyer. “EUROPEAN DESIGN GUIDE FOR FOOTBRIDGE VIBRATION.” In: (December 2022) (cited on page 25).

- [40] Tue Herlau, Mikkel N. Schmidt, and Morten Mørup. *Introduction to Machine Learning and Data Mining: Lecture Notes*. Volume 1.2. 2021 (cited on pages 5, 17, 18, 21).
- [41] Rongrong Hou et al. “Genetic algorithm based optimal sensor placement for L1-regularized damage detection.” In: *Structural Control Health Monitoring* 26.1 (2018) (cited on page 2).
- [42] Yiwei Hu et al. “Site-specific response spectra: Guidelines for engineering practice.” In: *CivilEng* 2.3 (2021), pages 712–735 (cited on page 55).
- [43] Daniel J Inman. *Engineering vibration*. Volume 2. Prentice Hall Englewood Cliffs, NJ, 2001 (cited on page 26).
- [44] Mohsen Kalateh-Ahani and Saeed Amiri. “A Park-Ang damage index-based framework for post-mainshock structural safety assessment.” In: *Structures* 33 (April 2021), pages 820–829. URL: <https://doi.org/10.1016/j.istruc.2021.04.039> (cited on pages 59, 60).
- [45] EI Katsanos, AG Sextos, and AS Elnashai. “Prediction of inelastic response periods of buildings based on intensity measures and analytical model parameters.” In: *Engineering Structures* 71 (2014), pages 161–177 (cited on pages 3, 49, 50, 52).
- [46] Evangelos I Katsanos, Anastasios G Sextos, and George D Manolis. “Selection of earthquake ground motion records: A state-of-the-art review from a structural engineering perspective.” In: *Soil dynamics and earthquake engineering* 30.4 (2010), pages 157–169 (cited on pages 3, 49).
- [47] Max Kuhn and Kjell Johnson. *Applied Predictive Modeling*. Springer, 2013 (cited on page 86).
- [48] Soon-Jung Kwon et al. “Design of Accelerometer Layout for Structural Monitoring and Damage Detection.” In: *KSCE Journal of Civil Engineering* 7.6 (2003), pages 717–724 (cited on page 2).
- [49] Jun Li et al. “Development and application of random forest technique for element level structural damage quantification.” In: *Structural Control and Health Monitoring* 28.3 (2021), e2678 (cited on page 103).
- [50] Dan Lu et al. “Damping Ratios of Reinforced Concrete Structures Under Actual Ground Motion Excitations.” In: *Dynamics of Civil Structures, Volume 2*. Springer, 2020, pages 259–268 (cited on page 25).
- [51] Antonio Luca et al. “Vibration analysis of footbridges: an overview of the current practice.” In: *MATEC Web of Conferences* 211 (January 2018), page 10002. DOI: [10.1051/matecconf/201821110002](https://doi.org/10.1051/matecconf/201821110002) (cited on page 25).
- [52] John B Mander, Michael JN Priestley, R Park, et al. “Theoretical stress-strain model for confined concrete.” In: *Journal of structural engineering* 114.8 (1988), pages 1804–1826 (cited on pages 40, 42, 133–135).

- [53] *matplotlib.pyplot.boxplot*. https://matplotlib.org/3.1.1/api/_as_gen/matplotlib.pyplot.boxplot.html. Accessed: 2023-01-02 (cited on page 10).
- [54] G. Mauro and L. K. Fogh. *Nonlinear State Estimation via Machine Learning*. Technical University of Denmark. https://github.com/s163761/Nonlinear_State_Estimation_ML. 2023 (cited on page 3).
- [55] *Model Commands*. <https://openseespydoc.readthedocs.io/en/latest/src/modelcmds.html>. Accessed: 2023-01-02 (cited on page 140).
- [56] *Neural Network hyperparameters and their optimization*. https://pytorch.org/tutorials/beginner/basics/optimization_tutorial.html. Accessed: 2023-01-02 (cited on page 20).
- [57] Hoang D Nguyen et al. “Rapid seismic damage-state assessment of steel moment frames using machine learning.” In: *Engineering Structures* 252 (2022), page 113737 (cited on page 113).
- [58] Guofei Pang, Liu Yang, and George Em Karniadakis. “Neural-net-induced Gaussian process regression for function approximation and PDE solution.” In: *Journal of Computational Physics* 384 (2019), pages 270–288 (cited on page 15).
- [59] Carl Edward Rasmussen. “Gaussian processes in machine learning.” In: *Summer school on machine learning*. Springer. 2004, pages 63–71 (cited on pages 11, 14, 112).
- [60] Michael H Scott. “Numerical integration options for the force-based beam-column element in OpenSees.” In: *Force-based element integration options in OpenSees* (2011), pages 1–7 (cited on page 38).
- [61] Debarati Datta Siddhartha Ghosh and Abhinav A. Katakdond. “Estimation of the Park–Ang damage index for planar multi-storey frames using equivalent single-degree systems.” In: *Engineering Structures* 33 (2011), pages 2509–2524. URL: <https://doi.org/10.1016/j.engstruct.2011.04.023>. (cited on pages 61, 114).
- [62] Carl Sisemore and Vit Babuška. *The Science and Engineering of Mechanical Shock*. Springer, 2020 (cited on pages 24, 26–28).
- [63] Elgar Slooten. “Feasibility study of a wood-concrete hybrid super tall building and optimization of its wind-induced behaviour.” PhD thesis. September 2018 (cited on page 26).
- [64] Hoon Sohn et al. “A Review of Structural Health Review of Structural Health Monitoring Literature 1996-2001.” In: *Office of Scientific Technical Information Technical Reports* (2002) (cited on page 2).
- [65] *Steel02 Material – Giuffré-Menegotto-Pinto Model with Isotropic Strain Hardening*. https://opensees.berkeley.edu/wiki/index.php/Steel02_Material---Giuffr%C3%A9-Menegotto-Pinto_Model_with_Isotropic_Strain_Hardening. Accessed: 2023-01-02 (cited on pages 41, 42).

- [66] Marius Tarpø et al. “Operational modal analysis based prediction of actual stress in an offshore structural model.” In: *Procedia engineering* 199 (2017), pages 2262–2267 (cited on page 10).
- [67] Shuai Teng et al. “Structural damage detection using convolutional neural networks combining strain energy and dynamic response.” In: *Meccanica* 55.4 (2020), pages 945–959 (cited on page 116).
- [68] *UniaxialMaterial Command.* https://opensees.berkeley.edu/wiki/index.php/UniaxialMaterial_Command. Accessed: 2023-01-02 (cited on page 41).
- [69] USGS. *Moment magnitude, Richter scale.* <https://www.usgs.gov/faqs/moment-magnitude-richter-scale-what-are-different-magnitude-scales-and-why-are-there-so-many>. Accessed: 2022-01-02. 2017 (cited on page 52).
- [70] SEAOC Vision 2000. “Performance based seismic engineering of buildings, vols. I and II: Conceptual framework. Sacramento.” In: *Structural Engineers Association of California, Sacramento, Calif* (1995) (cited on page 60).

APPENDIX A

Structural Model - Finite Element Model

Finite element (FE) analysis is a useful tool in order to estimate responses and forces for a given structure. The model used in a FE analysis is also known as a finite element model (FEM). In the following example, a frame structure will be analyzed, and the steps of the finite element analysis will be explained.

A.1 Equation of Motion

In figure A.1 the frame structure is seen with the numbering of elements and degrees of freedom (DOF). The structure is a 2-story frame with 6 beam elements and in total 6 generalized degrees of freedom.

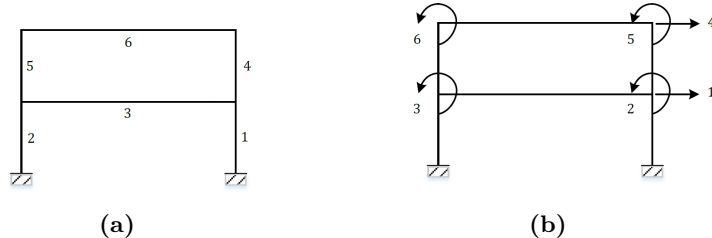


Figure A.1: Frame structure and labeling of: (a) elements and (b) degrees of freedom.

In this case, only the horizontal displacements and rotation DOFs are investigated i.e. the elements are having 4 local DOFs (two longitudinal and two rotational). The vertical displacements are then neglected and not used for the analysis, these could however easily be included by implementing structural elements with 6 local DOFs. The analysis itself originates from the equation of motion (EOM) of the structure:

$$\mathbf{M}\ddot{\mathbf{x}}(t) + \mathbf{C}\dot{\mathbf{x}}(t) + \mathbf{K}\mathbf{x}(t) = \mathbf{f}(t) \quad (\text{A.1})$$

where \mathbf{M} , \mathbf{C} , and \mathbf{K} the mass-, damping-, and stiffness matrices respectively which are associated with the generalized DOFs in the displacement vector $\mathbf{x}(t)$, while the $\mathbf{f}(t)$ describes the loading. These generalized DOFs discretize the structure such that each element in the vectors and matrices represents a generalized DOF - i.e. $\mathbf{x}(t) = [x_1(t), x_2(t), \dots, x_n(t)]^T$. The matrices and the loading are known, such that the EOM is solved with respect to the deformations. The solution is found by direct integration e.g. Newmark integration (Section A.2).

For a linear¹ analysis the stiffness matrix is constant and acts as the relation between deformation and loading. However, in the case of non-linear analysis, the term $\mathbf{K}\mathbf{x}(t)$ is replaced with the integral $\int \mathbf{K}(\mathbf{x})d\mathbf{x}$, which is not solved analytically but analytically by approximating the integral to a sum. The error by the approximation is then reduced with e.g. Newton-Raphson iterations.

Further, are the matrices are describing the entire structure, and are built using the mass and stiffness of the individual elements.

A.1.1 Stiffness matrix

The stiffness matrix is a fundamental component of the dynamic analysis for a given structure. To determine the stiffness matrix of the structure, the local stiffness matrices of the structural elements must be determined beforehand. The local stiffness matrices are usually determined by considering 2D elements with 2 degrees of freedom (DOF) per node and the corresponding actions (Figure A.2).

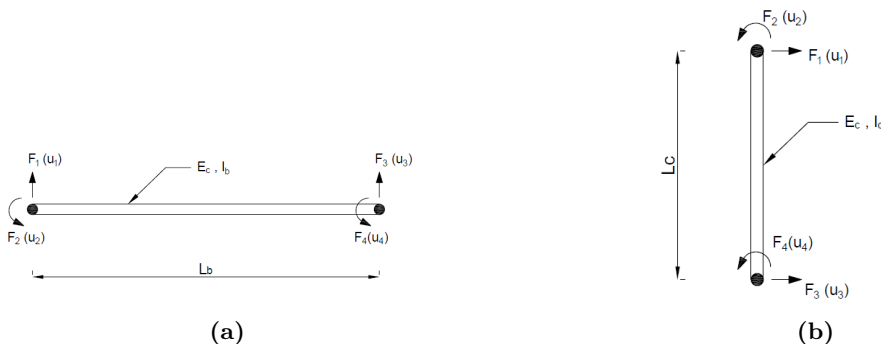


Figure A.2: Reference model for beams (a) and columns (b)

In Figure A.2, F_i denotes the reaction (force or moment) correspondent to the DOF u_i , E is the stiffness of the element (Young modulus), I is the inertia modulus of the

¹Linear and non-linear in this case correspond to the linearity and non-linearity of material/element behavior. A linear behaviour is when the materials deformations u is proportional with the applied loading F : $\mathbf{K}\mathbf{u} = F \Leftrightarrow \mathbf{K}^{-1}F = u$. The proportionality is then the stiffness K . A non-linear behavior is when the stiffness relation varies in order to correlate deformation and loading. The relation between the deformation and loading is then expressed using the integral: $\int \mathbf{K}(u)du = F$.

section and l is the length of the element ($l_{beam} = l_{column}$). Taking into account the presented reference systems, the local stiffness matrix can be defined as follows:

$$\mathbf{K}_{loc} = \begin{bmatrix} \kappa_{11} & \kappa_{12} & \kappa_{13} & \kappa_{14} \\ \kappa_{21} & \kappa_{22} & \kappa_{23} & \kappa_{24} \\ \kappa_{31} & \kappa_{32} & \kappa_{33} & \kappa_{34} \\ \kappa_{41} & \kappa_{42} & \kappa_{43} & \kappa_{44} \end{bmatrix} = \begin{bmatrix} 12\frac{EI}{l^3} & 6\frac{EI}{l^2} & -12\frac{EI}{l^3} & 6\frac{EI}{l^2} \\ 6\frac{EI}{l^2} & 4\frac{EI}{l} & -6\frac{EI}{l^2} & 2\frac{EI}{l} \\ -12\frac{EI}{l^3} & -6\frac{EI}{l^2} & 12\frac{EI}{l^3} & -6\frac{EI}{l^2} \\ 6\frac{EI}{l^2} & 2\frac{EI}{l} & -6\frac{EI}{l^2} & 4\frac{EI}{l} \end{bmatrix} \quad (A.2)$$

Each element stiffness coefficient k_{ij} is equal to the reaction j which is developed due to the activation of the unitary DOF i .

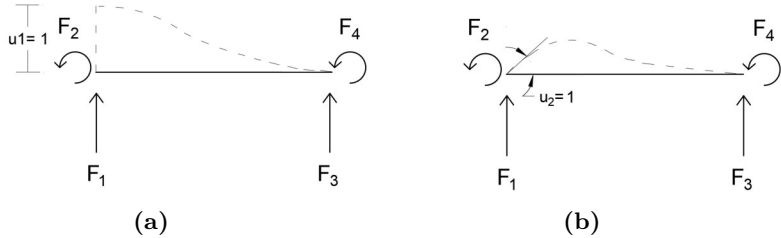


Figure A.3: Deformed shape of a beam due to a unit displacement (a) or due to a unit rotation (b)

For instance, when the DOF 1 is activated - e.g. vertical displacement $u_1 = 1$ illustrated in Figure A.3(a) - the following stiffness coefficients will be defined:

$$k_{11} = F_1 = 12\frac{EI}{l^3} \quad (A.3)$$

$$k_{12} = F_2 = 6\frac{EI}{l^2} \quad (A.4)$$

$$k_{13} = F_3 = -12\frac{EI}{l^3} \quad (A.5)$$

$$k_{14} = F_4 = 6\frac{EI}{l^2} \quad (A.6)$$

$$(A.7)$$

The same procedure can be applied for the second case in Figure A.3(b) which defined the stiffness coefficients placed in the second row of the matrix introduced in Equation A.2.

Once the local matrices have been defined, the global stiffness matrix can be assembled. Hence, a unit displacement or rotation is activated per each of the global DOFs

(Figure A.1(b)) giving a total of 6 cases. Note that each global stiffness coefficient is obtained by adding the corresponding local coefficients of the structural elements converging to the same nodal point. For example, the local stiffness coefficients involved in case 1 - e.g. activation of the global u_1 introduced in Figure A.1(b) - are illustrated in Figure A.4. Note that the superscript of each coefficient k_{ij} represents the element index.

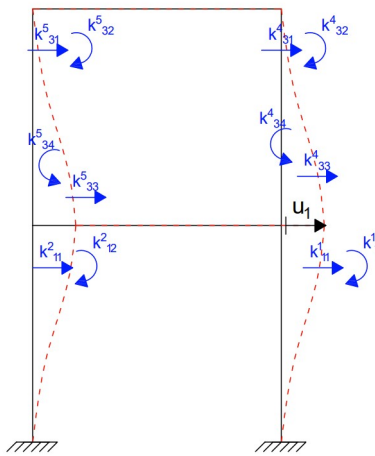


Figure A.4: Deformed shape of the structure in case 1

In the following, some of the coefficients for case 1 are calculated:

- Horizontal reaction correspondent to the global DOF 1:

$$K_{11} = \kappa_{11}^1 + \kappa_{11}^2 + \kappa_{33}^4 + \kappa_{33}^5 = 4 \cdot \frac{12EI}{l^3} \quad (\text{A.8})$$

- Moment correspondent to global DOF 2 and DOF 3:

$$K_{12} = \kappa_{12}^1 + \kappa_{34}^4 = \frac{6EI}{l^2} - \frac{6EI}{l^2} = 0 \quad \text{and} \quad K_{13} = \kappa_{12}^2 + \kappa_{34}^5 = 0 \quad (\text{A.9})$$

Finally, the global stiffness matrix is defined as follows²:

²NOTE: The indices $(\cdot)_c$ and $(\cdot)_b$ refer to the columns and beams respectively.

$$K = \begin{bmatrix} 48\frac{EI_c}{l_c^3} & 0 & 0 & -24\frac{EI_c}{l_c^3} & -6\frac{EI_c}{l_c^2} & -6\frac{EI_c}{l_c^2} \\ 0 & 4\frac{EI_b}{l_b} + 8\frac{EI_c}{l_c} & 2\frac{EI_b}{l_b} & 6\frac{EI_c}{l_c^2} & 2\frac{EI_c}{l_c} & 0 \\ 0 & 2\frac{EI_b}{l_b} & 4\frac{EI_b}{l_b} + 8\frac{EI_c}{l_c} & 6\frac{EI_c}{l_c^2} & 0 & 2\frac{EI_c}{l_c} \\ -24\frac{EI_c}{l_c^3} & -6\frac{EI_c}{l_c^2} & -6\frac{EI_c}{l_c^2} & 24\frac{EI_c}{l_c^3} & 6\frac{EI_c}{l_c^2} & 6\frac{EI_c}{l_c^2} \\ 6\frac{EI_c}{l_c^2} & 2\frac{EI_c}{l_c} & 0 & 6\frac{EI_c}{l_c^2} & 4\frac{EI_b}{l_b^2} + 4\frac{EI_c}{l_c} & 2\frac{EI_b}{l_b^2} \\ 6\frac{EI_c}{l_c^2} & 0 & 2\frac{EI_c}{l_c} & 6\frac{EI_c}{l_c^2} & 2\frac{EI_b}{l_b^2} & 4\frac{EI_b}{l_b^2} + 4\frac{EI_c}{l_c} \end{bmatrix} \quad (A.10)$$

A.1.2 Mass matrix

Overall, the procedure followed for constructing the mass matrix is similar to the process introduced for the stiffness matrix previously: the local mass matrix is determined for the single elements and its elements are employed to build the global matrix afterwards. However, in this case, the elements of the matrices represent inertia forces due to unit translational or rotational accelerations $\ddot{u}_i = 1$ at DOF_i .

Therefore, it is worth noting to report the final local mass matrix which holds both for beam elements and column elements (Equation A.11).

$$m_{loc} = \begin{bmatrix} m_{11} & m_{12} & m_{13} & m_{14} \\ m_{21} & m_{22} & m_{23} & m_{24} \\ m_{31} & m_{32} & m_{33} & m_{34} \\ m_{41} & m_{42} & m_{43} & m_{44} \end{bmatrix} = \frac{\bar{m}l}{420} \begin{bmatrix} 156 & 22l & 54 & -13l \\ 22l & 4l^2 & 13l & -3l^2 \\ 54 & 13l & 156 & -22l \\ -13l & -3l^2 & -22l & 4l^2 \end{bmatrix} \quad (A.11)$$

where \bar{m} represents the mass of the element per unit length l .

Finally, as previously shown in the case of the stiffness matrix, the accelerations at each global DOF (Figure A.1(b)) are activated and the global mass coefficients are obtained by adding the local mass coefficient and the global mass matrix 6x6 can be determined.

$$M = \begin{bmatrix} 624\frac{m_c l_c}{420} & 0 & 0 & 108\frac{m_c l_c}{420} & 13\frac{m_c l_c^2}{420} & 13\frac{m_c l_c^2}{420} \\ 0 & 4\frac{m_b l_b^3}{420} + 8\frac{m_c l_c^3}{420} & -3\frac{m_b l_b^3}{420} & 13\frac{m_c l_c^2}{420} & -3\frac{m_c l_c^3}{420} & 0 \\ 0 & -3\frac{m_b l_b^3}{420} & 4\frac{m_b l_b^3}{420} + 8\frac{m_c l_c^3}{420} & 13\frac{m_c l_c^2}{420} & 0 & -3\frac{m_c l_c^3}{420} \\ 108\frac{m_c l_c}{420} & 13\frac{m_c l_c^2}{420} & 13\frac{m_c l_c^2}{420} & 312\frac{m_c l_c}{420} & 22\frac{m_c l_c^2}{420} & 22\frac{m_c l_c^2}{420} \\ 13\frac{m_c l_c^2}{420} & -3\frac{m_c l_c^3}{420} & 0 & 22\frac{m_c l_c^2}{420} & 4\frac{m_b l_b^3}{420} + 4\frac{m_c l_c^3}{420} & -3\frac{m_b l_b^3}{420} \\ 13\frac{m_c l_c^2}{420} & 0 & -3\frac{m_c l_c^3}{420} & 22\frac{m_c l_c^2}{420} & -3\frac{m_b l_b^3}{420} & 4\frac{m_b l_b^3}{420} + 4\frac{m_c l_c^3}{420} \end{bmatrix} \quad (A.12)$$

A.1.3 Damping matrix

In order to determine the damping matrix \mathbf{C} , the same procedure could be applied when determining the mass and stiffness matrices i.e. determining the damping matrix from the elements. However, since the damping of the elements is not as easily estimated as mass and stiffness, the concept of Rayleigh damping is usually applied. Rayleigh damping consists of two terms proportional to the mass and stiffness matrices:

$$\mathbf{C} = \alpha \mathbf{M} + \beta \mathbf{K} \quad (\text{A.13})$$

where the α -term represents damping by motion e.g. interaction with external factors such as wind, water, or soil, and the β -term represents damping by deformation e.g. internal factors such as yielding, damage, and friction. In this way, the damping matrix is constructed from the two known matrices of mass and stiffness.

The two parameters α , and β are determined using the damping ratio³ ζ , and natural frequency⁴ ω , for different modes j :

$$\zeta_j = \frac{1}{2} \left(\frac{\alpha}{\omega_j} + \beta \omega_j \right) \quad (\text{A.14})$$

A.2 Newmark Integration

The Newmark method apart from the discretization of the structure provides also the discretization of the time domain into time-steps $\Delta t = h$. The time integration results are then noted as:

$$\mathbf{x}(t_0) = \mathbf{x}_0 \quad , \quad \mathbf{x}(t_1) = \mathbf{x}_1 \quad \dots \quad \mathbf{x}(t_N) = \mathbf{x}_N \quad (\text{A.15})$$

The method further requires initial conditions in terms of displacement and velocity such that:

$$\mathbf{x}(0) = \mathbf{x}_0 \quad , \quad \dot{\mathbf{x}}(0) = \dot{\mathbf{x}}(0) \quad (\text{A.16})$$

from where the acceleration term is estimated. The aim of the method is then to definition of the solution \mathbf{x}_{n+1} and $\dot{\mathbf{x}}_{n+1}$ at the time step $n + 1$, from the previous time step n , and then determine the acceleration $\ddot{\mathbf{x}}_{n+1}$. The method is then a 'single step - single solve' procedure.

³The damping ratio is a ratio between the actual damping level of the structure and the critical damping level of the structure: $\zeta = \frac{c}{c_{critical}}$. The parameter is well known for civil structures, with levels of magnitude between $\zeta \in [0.01 - 0.05]$.

⁴The natural frequency is the frequency in which a specific mode of the structure resonates. The modes are simply the individual behaviours of a given structure. The natural frequencies are determined using modal analysis, where the number of modes (and frequencies) that can be determined from a FEM analysis is the number of generalized DOFs of the structure.

Since the displacement increment is the integral of the velocity, and the velocity increment is the integral of the acceleration, it is possible to express the time steps in time $n + 1$ in terms of the previous time step n as follows:

$$\dot{\mathbf{x}}_{n+1} = \overbrace{\dot{\mathbf{x}}_n + (1 - \gamma) h \ddot{\mathbf{x}}_n + \gamma h \ddot{\mathbf{x}}_{n+1}}^{\dot{\mathbf{x}}_{n+1}^*} \quad (\text{A.17})$$

$$\mathbf{x}_{n+1} = \mathbf{x}_n + h \dot{\mathbf{x}}_n + \underbrace{\left(\frac{1}{2} - \beta \right) h^2 \ddot{\mathbf{x}}_n + \beta h^2 \ddot{\mathbf{x}}_{n+1}}_{\mathbf{x}_{n+1}^*} \quad (\text{A.18})$$

Since the first terms, $\dot{\mathbf{x}}_{n+1}^*$ and \mathbf{x}_{n+1}^* are only containing values within the known time step n , these parameters are known as predictors and can be estimated with using known parameters. The remaining two terms that include accelerations in the following unknown step are known as correcter terms. Furthermore, are the parameters $\gamma \in [0, 1]$ and $\beta \in [0, \frac{1}{2}]$ indicators of how finely the time step h is split. Considering only the predicted values, it is possible to calculate the acceleration at step $n + 1$ applying the EOM as follows:

$$\mathbf{M} \ddot{\mathbf{x}}_{n+1} + \mathbf{C} \dot{\mathbf{x}}_{n+1} + \mathbf{K} \mathbf{x}_{n+1} = \mathbf{f}_{n+1}(t), \quad (\text{A.19})$$

substituting Equations (A.18) and (A.17) it results in:

$$\mathbf{M}^* \dot{\mathbf{x}}_{n+1} = \mathbf{f}_{n+1} - \mathbf{C} \dot{\mathbf{x}}_{n+1}^* - \mathbf{K} \mathbf{x}_{n+1}^*, \quad (\text{A.20})$$

where

$$\mathbf{M}^* = \mathbf{M} + \gamma h \mathbf{C} + \beta h^2 \mathbf{K} \quad (\text{A.21})$$

As a result, once the acceleration at step $n + 1$ is calculated through Equation A.20, the correction factors in Equations (A.17) and (A.18) are estimated and the final solution is obtained.

The choice of the parameters γ and β , which are introduced to control the interpolation of the acceleration, and of the time step length h is fundamental to getting reliable solutions through the Newmark method. In fact, the issues of this method regard both stability and accuracy [3].

In order to guarantee stability⁵ of the algorithm, $\gamma \geq \frac{1}{2}$ is required, corresponding to a forward weighting in the acceleration interpolation. While $\beta \geq \frac{1}{4}(\gamma + \frac{1}{2})^2$, is required for an unconditional stability - i.e. not dependent on the time step length h . These stability conditions are valid when investigating harmonic oscillations.

Common values for γ and β that assures stability are seen in Table A.1

⁵Stability meaning the free vibration response is not increasing i.e. $|\lambda| \leq 1$.

Table A.1: Selection of Newmark parameters based on algorithm.

Algorithm	γ	β	$(\omega h)_{cr}$	$ \lambda - 1$	$\frac{\Delta T}{T}$
Fully Explicit	0	0	0	$\frac{1}{4} (\omega h)^2$	$-\frac{1}{96} (\omega h)^2$
Central Difference	$\frac{1}{2}$	0	2	0	$-\frac{1}{24} (\omega h)^2$
Fox-Goodwin	$\frac{1}{2}$	$\frac{1}{12}$	$\sqrt{6}$	0	$O((\omega h)^3)$
Linear Acceleration	$\frac{1}{2}$	$\frac{1}{6}$	$2 \sqrt{3}$	0	$\frac{1}{24} (\omega h)^2$
Average Acceleration	$\frac{1}{2}$	$\frac{1}{4}$	∞	0	$\frac{1}{12} (\omega h)^2$

APPENDIX B

Material properties of confined concrete

The concrete elements used for the analysis are constructed with stirrups. A way to model this in OpenSees, is by assuming that the concrete is then composed of an un-confined outer layer, and a confined inner layer with different strengths. The confined concrete strength is then to be larger than the original un-confined, and this increase in strength can be estimated by assuming a Mander Model [52].

B.1 Mander Material

The Mander model, the additional strength of the concrete is determined by a ratio $\eta = f_{cc}/f_{c,0}$ between the confined concrete f_{cc} and the un-confined concrete $f_{c,0}$. The model further takes into account the geometry of the section as well as both the longitudinal and stirrup reinforcement. The strength of the confined concrete is to be found for two rectangular cross sections.

The area of the confined concrete A_{cc} is estimated based on the area of the total confined element A_c , and the ratio between the longitudinal reinforcement and the core section ρ_{cc} :

$$A_{cc} = A_c(1 - \rho_{cc}) \quad (\text{B.1})$$

This area is used to determine the confinement effectiveness coefficient $k_e = A_e/A_{cc}$, which is the ratio between the area of effectively confined concrete and the area of confined concrete A_{cc} .

Given for a rectangular cross section k_e can be estimated as:

$$k_e = \frac{\left(1 - \sum_{i=1}^n \frac{(w'_i)^2}{6b_c d_c}\right) \left(1 - \frac{s'}{2b_c}\right) \left(1 - \frac{s'}{2d_c}\right)}{1 - \rho_{cc}} \quad (\text{B.2})$$

where the dimensions used are defined in Figure B.1.

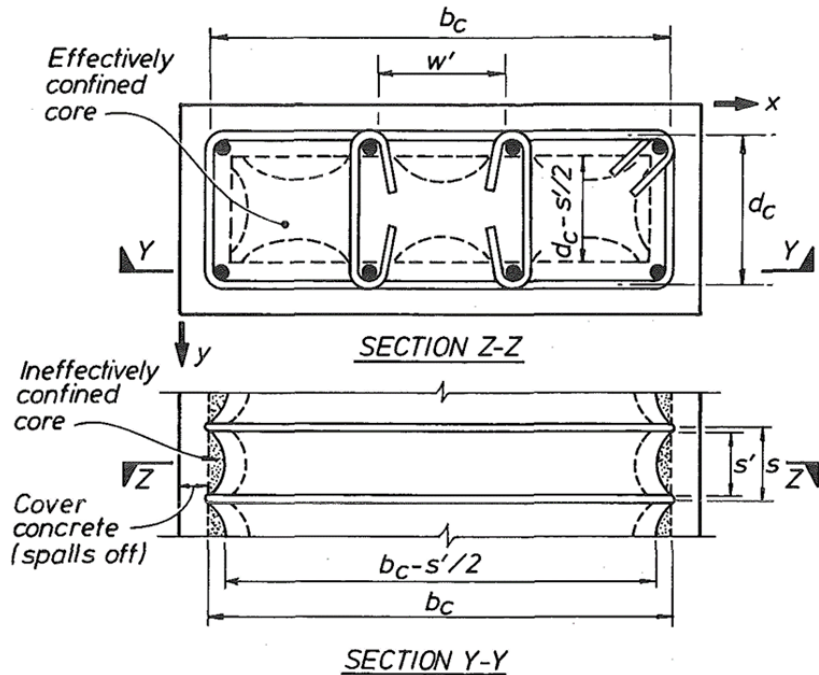


Figure B.1: Effectively Confined Core of Rectangular Stirrup Reinforcement [52].

The effective lateral confining stresses f'_{lx} and f'_{ly} can then be estimated for the x- and y directions respectively utilizing Equation (B.3).

$$f'_{lx} = k_e \rho_x f_{y,h} \quad , \quad f'_{ly} = k_e \rho_y f_{y,h} \quad , \quad \begin{cases} \rho_x = \frac{A_{sx}}{sd_c} \\ \rho_y = \frac{A_{sy}}{sb_c} \end{cases} \quad (B.3)$$

To find the strength parameter, these lateral confining stresses are then normalized with the strength of the un-confined concrete $f'_{c,0}$. These two ratios are then used to determine the strength parameter using Figure B.2.

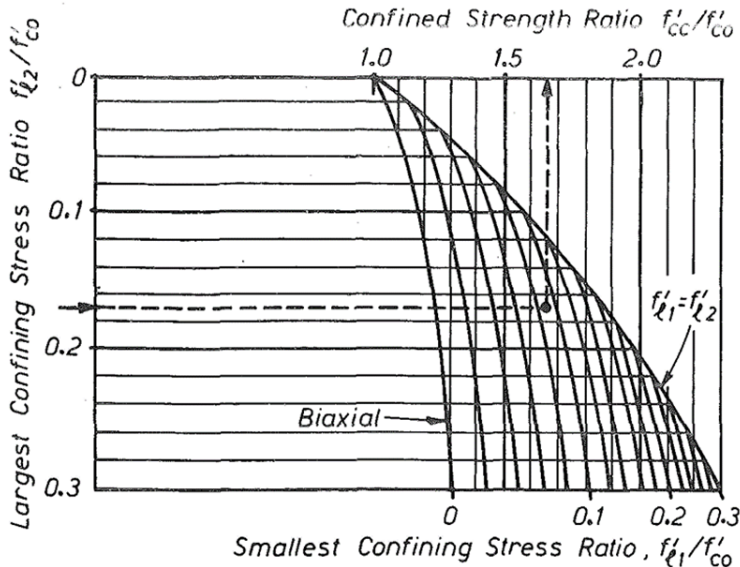


Figure B.2: Confined strength determination from lateral confining stresses for rectangular sections [52].

In Table B.1 the given parameters are listed along with the confined strength parameter $\eta = 1.45$ for both elements.

Table B.1: Material properties for concrete.

Cross section	Column	Beam
Ratio , ρ_{cc}	1.31 %	1.53 %
Confinement effectiveness coefficient, k_e	0.59	0.63
Lateral confining stress in x, $f'_{l,x}$	1.63 MPa	1.33 MPa
Lateral confining stress in y, $f'_{l,y}$	1.63 MPa	1.73 MPa
Un-confined concrete strength, $f'_{c,0}$	20 MPa	20 MPa
Minimum stress ratio, $f'_{l,1}$	0.08	0.07
Maximum stress ratio, $f'_{l,2}$	0.08	0.09
Strength ratio, η	1.45	1.45

B.2 Confined Concrete Parameters

The confined concrete parameter η has been estimated, based on the elements of reinforcement in both sections. With this information the material properties of both

elements can be estimated given they are composed of two concrete materials. The modelling of the material properties are based on the OpenSees example 'Ex9e', which models a rectangular reinforced concrete fiber section [24].

The formulations used to determine the material properties are listed in Table B.2. The properties of the un-confined material is solely based on the parameters of the un-confined material. However, some parameters of the confined material is based on the un-confined material. This is for instance the case with the compressive strength of the confined concrete $f_{c,c}$ that is based on the un-confined strength $f_{c,u}$. Note then that the index separated with a comma specifies if the property is for the un-confined material, i.e. $(-)_{-,u}$ is specifically referring to the un-confined material.

Table B.2: The formulations of the material properties for concrete.

Material	Un-confined	Confined
Compressive strength, f_c	20 MPa	$\eta f_{c,u}$
Strain at maximum strength, ε_{c0}	0.30 %	$2f_c/E_0$ %
Initial Young's Modulus, E_0	$2f_c/\varepsilon_{c0}$	$2f_{c,u}/\varepsilon_{c0,u}$
Crushing strength, f_{cu}	$0.2f_c$	$0.2f_c$
Strain at crushing strength, ε_{cu}	1.00 %	$5\varepsilon_{c0}$
Crushing slope ratio, λ	0.1	0.1
Tensile strength, f_t	$0.14f_{cu}$	$0.14f_{cu}$
Tension softening stiffness, $E_{t,s}$	$f_t/0.002$	$f_{t,u}/0.002$

APPENDIX C

Degree of Reinforcement

The element is normally reinforced if the degree of reinforcement ω is in between the limits of under- and over reinforcement ω_{und} , ω_{bal} respectively. I.e. the element is normally reinforced if $\omega_{und} \leq \omega \leq \omega_{bal}$, which means that the steel is yielding at the instance as crushing of the concrete occurs. The level of reinforcement is estimated based on Equation (C.1):

$$\omega = \frac{A_s f_{yd}}{b d f_{cd}} \quad (\text{C.1})$$

where A_s is the area of the tension steel, f_{yd} is the yielding stress of the steel, b is the width of the section, d is the distance from the top of the section to the tension reinforcement, and f_{cd} is the compressive strength of the concrete.

A schematic of a general reinforcement section along with its strain values are seen in Figure C.1:

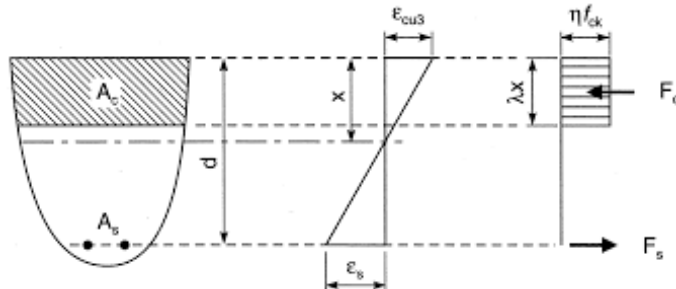


Figure C.1: General cross section showing compression zone as well as strains in the section.

The limit-values of the reinforcement degree are estimated based in Equation (C.2):

$$\omega_{und} = \lambda \frac{\varepsilon_{cu3}}{\varepsilon_{cu3} + \varepsilon_{uk}} \quad , \quad \omega_{bal} = \lambda \frac{\varepsilon_{cu3}}{\varepsilon_{cu3} + \varepsilon_{yd}} \quad (\text{C.2})$$

where $\lambda = 0.8$ is the ratio between the height of the compression zone x and the compression zone y of the cross section, $\varepsilon_{cu3} = 0.350\%$ is the maximal strain in the concrete¹, $\varepsilon_{uk} = 5.0\%$ is the maximal reinforcement strain for Class B steel, and ε_{yd} is the yielding strain in the steel.

Based on the equations (C.1) and (C.2), the degrees of reinforcement of the cross sections can be estimated. Along with material properties are the degrees listed in Table C.1. Note that both cross sections are normally reinforced.

Table C.1: Material properties for concrete.

Cross section	Column	Beam
Steel Material		
Area of tension steel, A_s	603 mm ²	1206 mm ²
Characteristic yield strength, $f_{yk,0}$	410 MPa	410 MPa
Design yield strength ² , f_{yd}	340 MPa	340 MPa
Maximal steel strain, ε_{uk}	5.0 %	5.0 %
Yield strain of steel ³ , ε_{yd}	0.16 %	0.16 %
Concrete Material		
Element width, b	400 mm	400 mm
Distance to tension steel, d	369 mm	467 mm
Characteristic crushing strength (un-confined), $f_{ck,0}$	20 MPa	20 MPa
Characteristic crushing strength (confined) ⁴ , f_{ck}	29 MPa	29 MPa
Design crushing strength ⁵ , f_{cd}	20 MPa	20 MPa
Maximal compression strain, ε_{cu3}	0.35 %	0.35 %
Degrees of reinforcement		
Degree of reinforcement, ω	7.0 %	11.0 %
Limit for under-reinforcement, ω_{und}	5.2 %	5.2 %
Limit for over-reinforcement, ω_{bal}	51.4 %	51.4 %

¹The values of $\lambda = 0.8$ and $\varepsilon_{cu3} = 0.350\%$ are valid for element with a concrete strength between C12-C50.

²The design strength is determined based on a partial coefficient $\gamma_s = 1.2$ such as $f_{yd} = f_{yk}/\gamma_s$.

³Yield strain of steel is estimated based on the Young's modulus and design yield strength $E_s = 210$ GPa such as $\varepsilon_{yd} = f_{yd}/E_s$.

⁴The crushing strength for the confined material is determined based on the strength ratio $\eta = 1.45$ such as $f_{ck} = \eta f_{ck,0}$.

⁵The design strength is determined based on a partial coefficient $\gamma_c = 1.45$ such as $f_{cd} = f_{ck}/\gamma_c$.

APPENDIX D

OpenSees: Analysis & Load Application

Two types of analysis are to be carried out, namely static analysis and transient analysis. The transient analysis is also known as a dynamic analysis. The gravity analysis is a static analysis, where the loads applied are line loads on the horizontal beam elements of the structure. For the transient analysis, the nodal masses are applied to the structure.

D.1 Analysis Creation

The way an analysis is created in OpenSees are by utilizing a series of command functions, which includes [6]:

- **analysis** : Describes which type of analysis is to be performed. In input to the command is either a static or transient.
- **constraints**: Object determines how the constraint equations are enforced in the analysis. For both analysis utilizes plain constraints, which are able to enforce homogeneous single point constraints such as the fixed constraints.
- **numberer** : Object that numbers the DOFs. The plain numberer is used, which just takes whatever order the domain gives it nodes and numbers them.
- **system** : Objects to store and solve the system of equations in the analysis. The command FullGeneral is used to construct linear system of equation object.
- **test** : Convergence test, that defines the tolerance and the number of iterations. The tolerance and number of iterations used are $\varepsilon_{tol} = 10^{-10}$ and $N_{iter} = 100$ respectively. The systems equation is given by formed as: $\mathbf{K}_T \Delta \mathbf{U} = \mathbf{R}_{Res}$.
- **algorithm** : Algorithm for solving the nonlinear equations. The Newton-Raphson method is utilized.

- **integrator** : Object that 1) determines the predictive step for time $t + \Delta t$, 2) specifies the tangent matrix \mathbf{K}_T and residual vector \mathbf{R}_{res} at any iteration, and 3) determines the corrective step based on the displacement increment $\Delta\mathbf{U}$.

The only command that differs between the static and transient analysis is the chosen integrator. For the static analysis the LoadControl command is used to increment the loads until fully applied, with a total of 10 steps.

Whereas the Newmark integrator is used for the transient analysis, using the Average Acceleration algorithm with parameters $\gamma = 1/2$, $\beta = 1/4$. This algorithm is unconditionally stable, meaning that it converges not based on the stepping-size $\Delta t = h$.

D.2 Load application

The loading is applied with the following commands in OpenSees [55]:

- **timeSeries** : Object that defines the relation between the time and the load-intensity.
- **pattern** : Object that add the loads to the structure.

For the static analysis a 'linear' time-series will be used for the gravity analysis, by which the gravity loads are applied incrementally until the full load is applied.

A plain load pattern is applied for the static analysis.

In addition to these commands is the load added using the command **eleload**, that along with the **beamUniform** type applies the uniform loads to specific beam elements.

For the transient analysis the time-series are added with the 'path' command, since the loads are given as measured accelerations. The command allows to multiply the entire time-series with a constant that is composed of the load-factor and the gravitational constant g . In that way the acceleration are converted to the unit m/s^2 , and scaled with the load-factor.

The load pattern used for the transient analysis is the 'UniformExcitation', that allows the load to be applied as a uniform excitation to a model acting in a certain direction. The loads are applied directly as nodal masses using the command 'mass', when the model geometry and supports are created. The nodal masses are only used for the transient analysis. Another pattern is the 'MultiSupport' excitation that enables the structure to experience similar or different prescribed ground motions at various supports in the structure.

APPENDIX E

Gaussian Process

E.1 Ground motions - train set

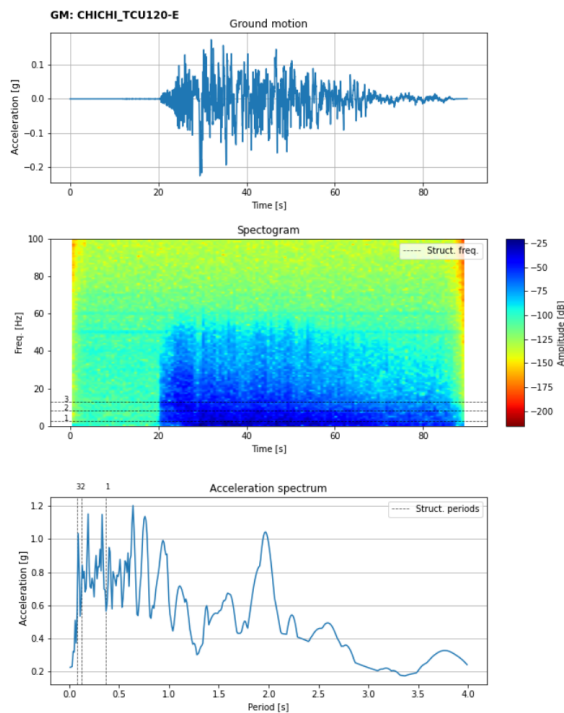


Figure E.1: GM in the train set for preliminary study: ID 52.

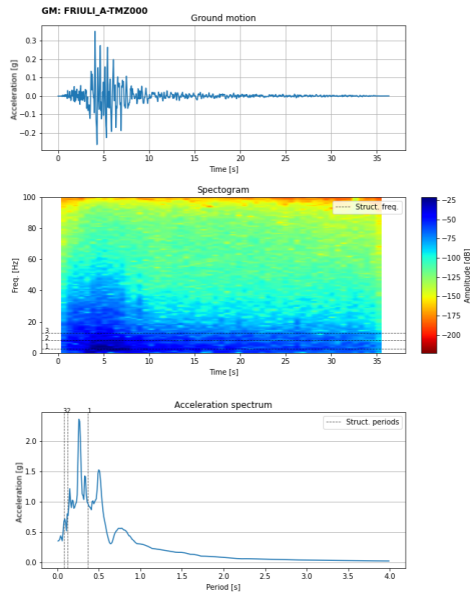


Figure E.2: GM in the train set for preliminary study: ID 86.

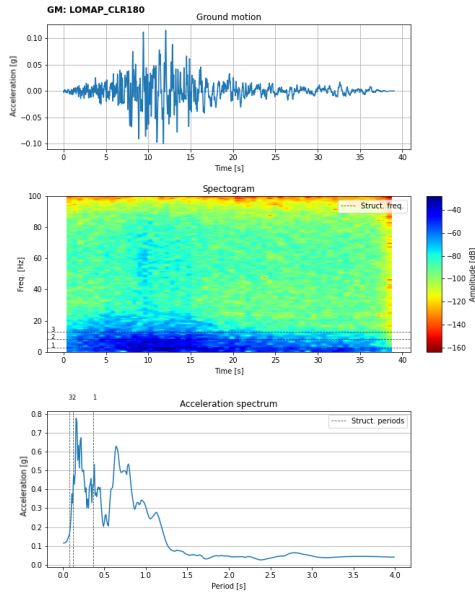


Figure E.3: GM in the train set for preliminary study: ID 149.

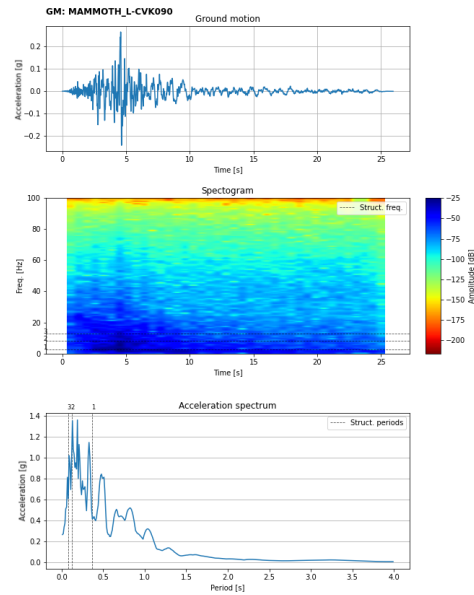


Figure E.4: GM in the train set for preliminary study: ID 182.

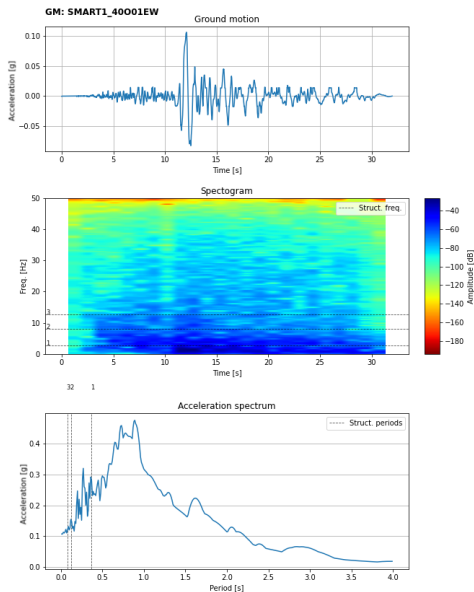


Figure E.5: GM in the train set for preliminary study: ID 247.

E.2 Preliminary study for GM CHICHI-HWA033-N (ID 23)

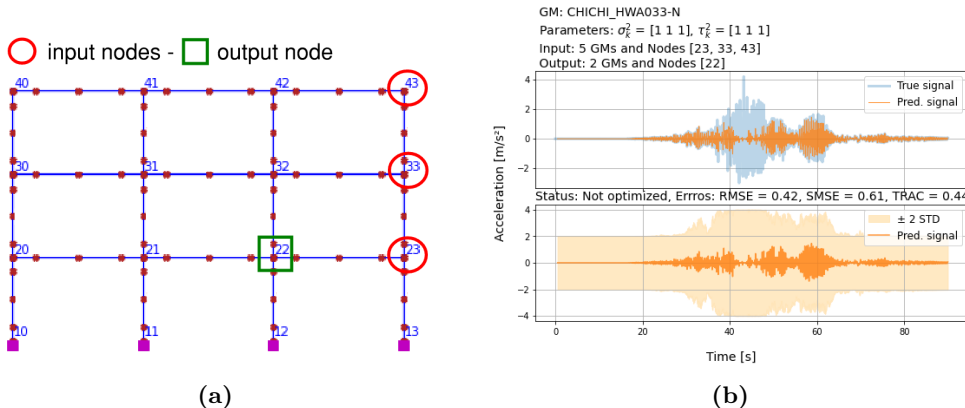


Figure E.6: C1.1: Non-optimized GP, prediction of CHICHI-HWA033-N, ID 23. Input and output nodes (a) - results and errors (b).

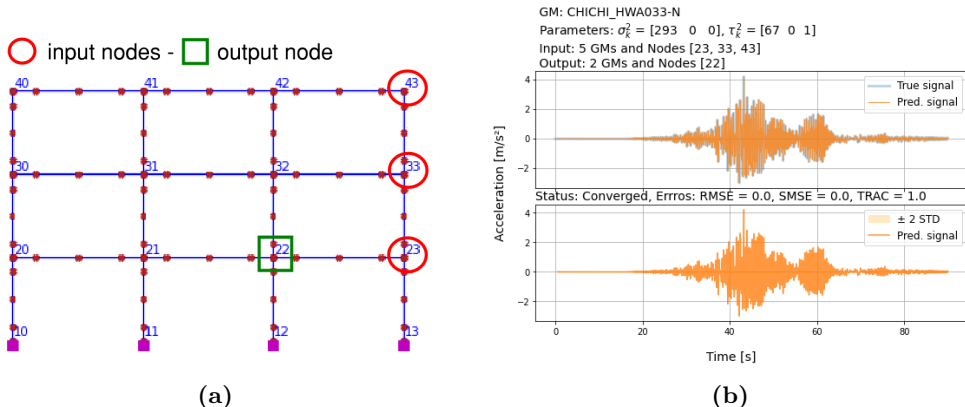


Figure E.7: C1.2: Optimized GP, prediction of CHICHI-HWA033-N, ID 23. Input and output nodes (a) - results and errors (b).

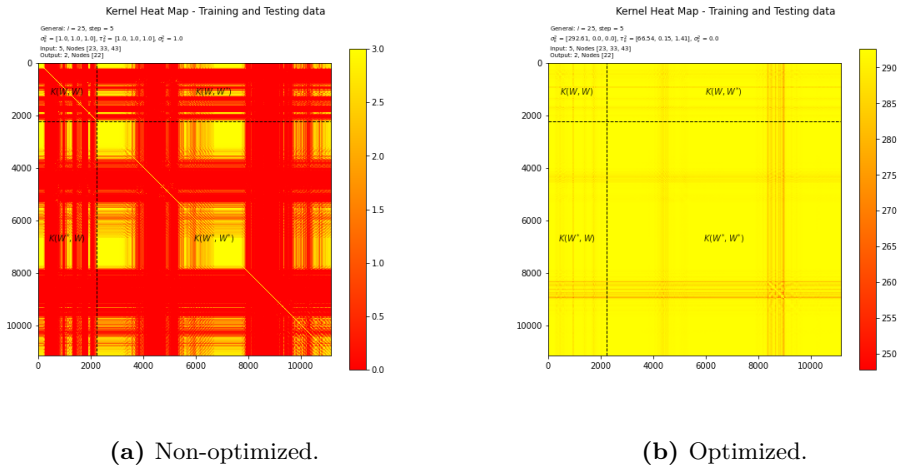


Figure E.8: Comparison of Kernel matrix for GP, prediction of CHICHI-HWA033-N, ID 23. With optimized parameters (a) - without optimized parameters (b)

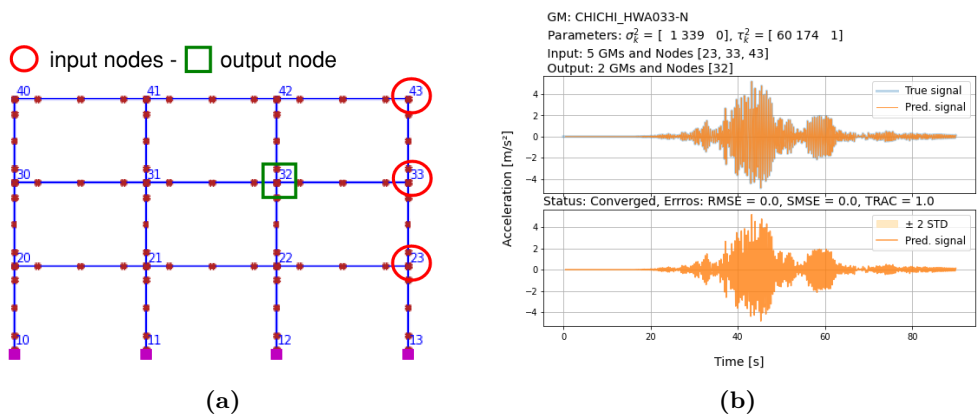


Figure E.9: C2.1: Optimized GP, prediction of CHICHI-HWA033-N, ID 23. Input and output nodes (a) - results and errors (b).

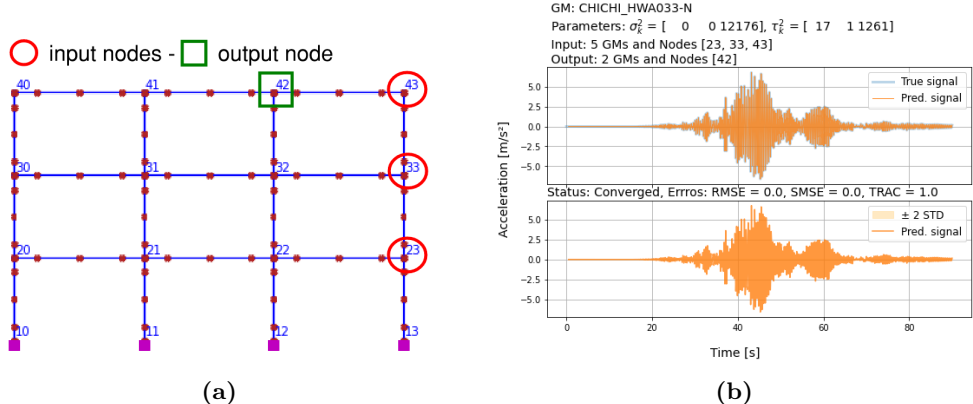


Figure E.10: C2.2: Optimized GP, prediction of CHICHI-HWA033-N, ID 23. Input and output nodes (a) - results and errors (b).

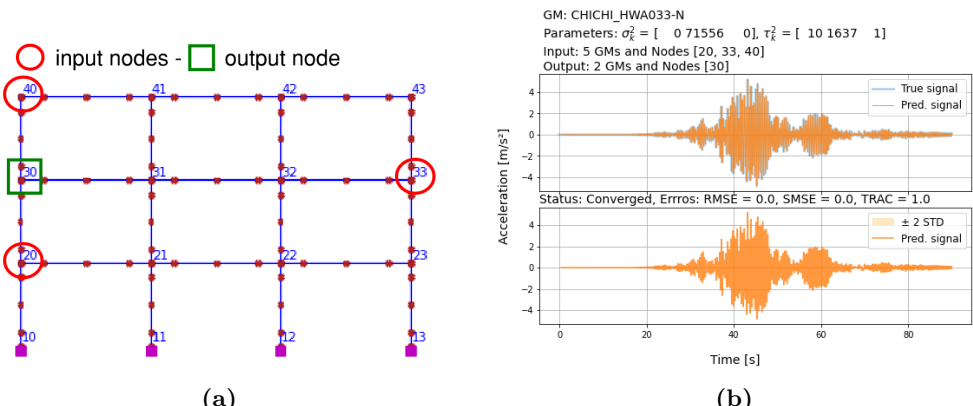


Figure E.11: C3.1: Optimized GP, prediction of CHICHI-HWA033-N, ID 23. Input and output nodes (a) - results and errors (b).

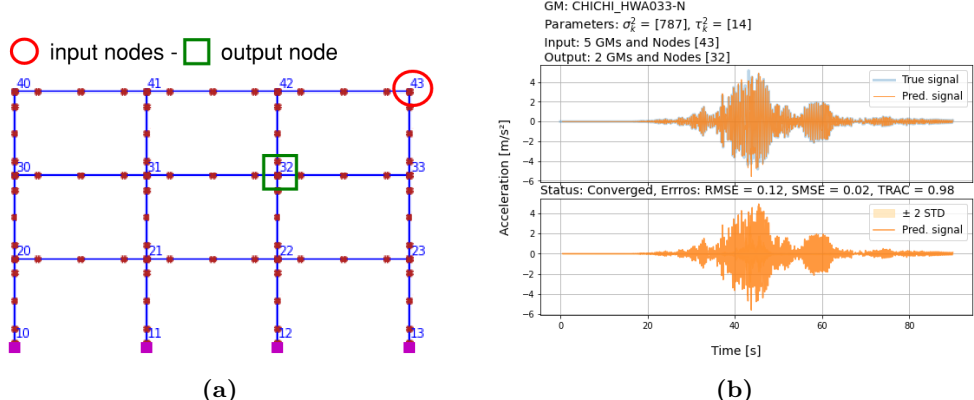


Figure E.12: C4.1: Optimized GP, prediction of CHICHI-HWA033-N, ID 23. Input and output nodes (a) - results and errors (b).

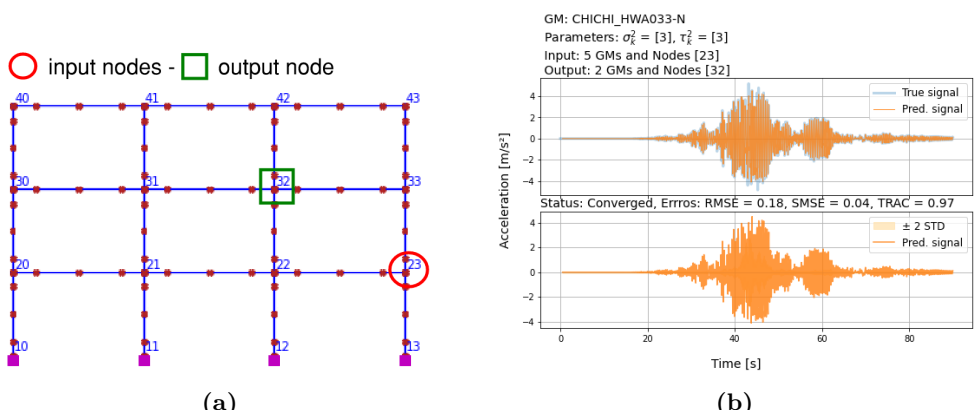
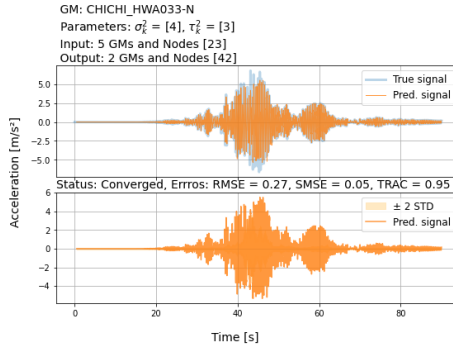
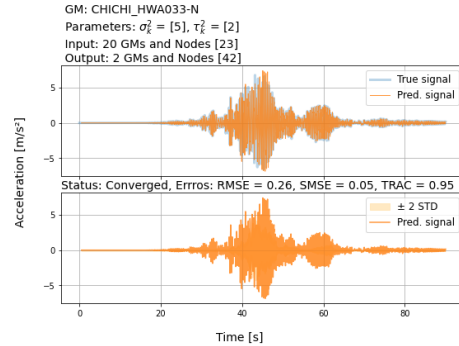


Figure E.13: C4.2: Optimized GP, prediction of CHICHI-HWA033-N, ID 23. Input and output nodes (a) - results and errors (b).

E.3 Overall assessment for GM CHICHI-HWA033-N (ID 23)



(a) GM23, Case 5: train - 5 GMs.



(b) GM23, Case 6: train - 20 GMs.

Figure E.14: Comparison results Case 5 and Case 6 for the overall assessment of the GP. The predictions are seen for the responses associated with ground motion GM23 CHICHI-HWA033-N. The predictions were made in node 42 given the inputs from node 23.

APPENDIX F

Gaussian Process - Error Matrices

F.1 Error Matrix for the entire structure

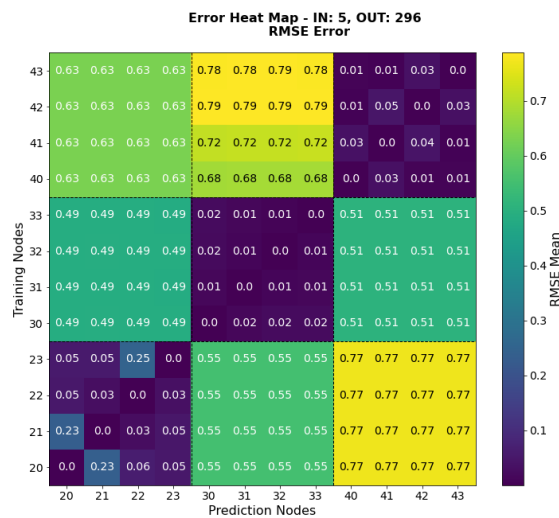


Figure F.1: The mean RMSE measure for the 296 output responses for each input/output node pair.

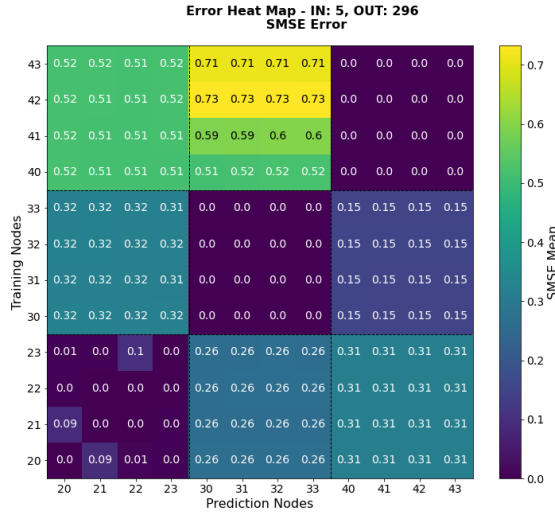


Figure F.2: The mean SMSE measure for the 296 output responses for each input/output node pair.

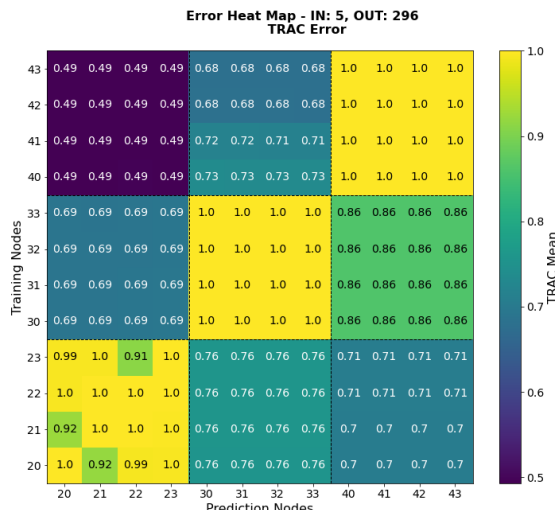


Figure F.3: The mean TRAC measure for the 296 output responses for each input/output node pair.

F.2 Error Matrix for each floor

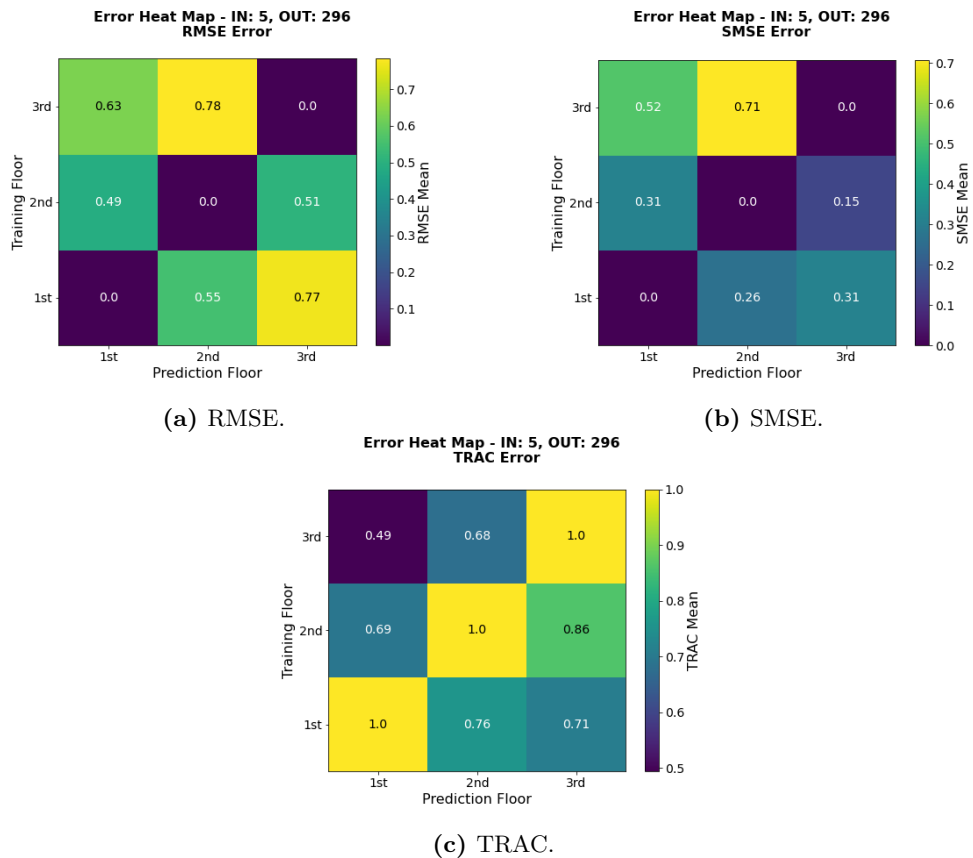


Figure F.4: Mean error estimations for each floor from 296 predictions.

F.3 Error distribution

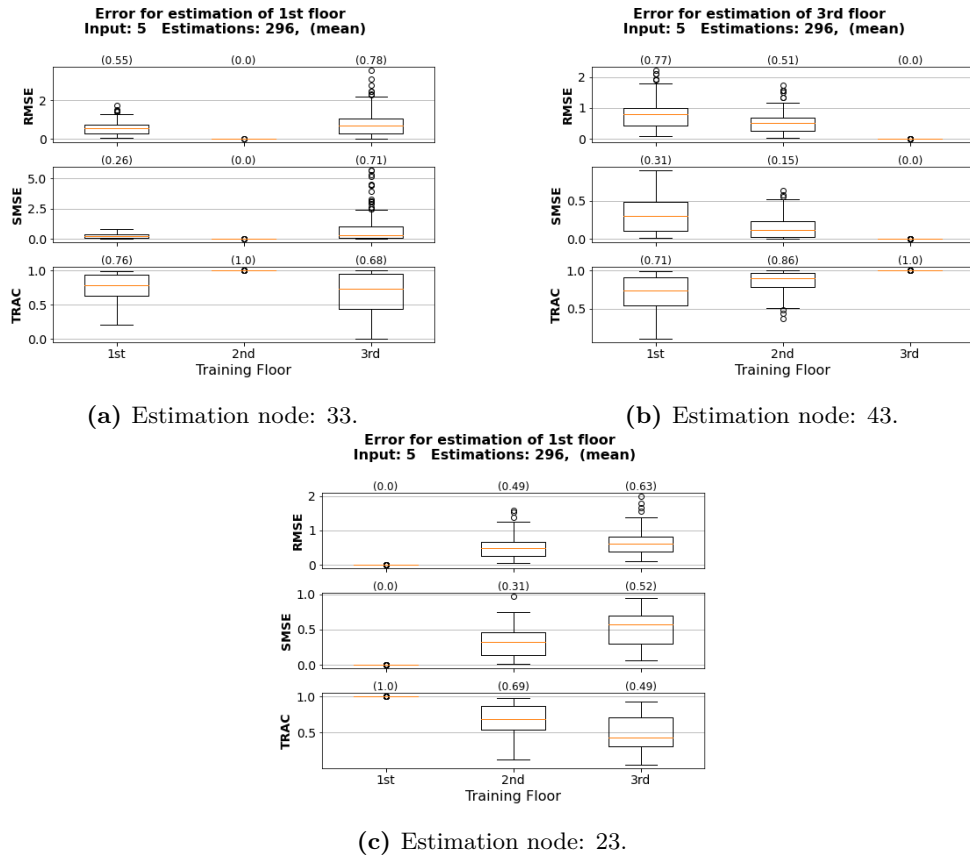


Figure F.5: Distribution of error measure based on the 296 estimation of each floor.

APPENDIX 

Neural Network - Responses related to the LDA & NDS Load-sets

Table G.1: Testing sets for each of the K=10 folds. The training set for each fold includes the remaining responses not used in the testing set. In total are this set composed of 198 responses in the linear and non-linear respectively. The presented responses associated with the LDA load-set, which are all categorized as **linear** and are all having a load-factor=0.5.

Fold, i	Response IDs	Number of Responses
1	301, 303, 305, 306, 308, 309, 310, 311, 313, 314 315, 316, 317, 318, 319, 321, 324, 325, 326, 327	20
2	330, 331, 332, 333, 335, 337, 339, 340, 347, 349 350, 351, 352, 353, 357, 358, 359, 361, 362, 363	20
3	364, 366, 367, 368, 369, 370, 371, 376, 377, 378 380, 381, 382, 385, 386, 387, 394, 395, 396, 398	20
4	401, 402, 403, 404, 405, 407, 408, 410, 411, 412 413, 415, 416, 417, 418, 419, 420, 421, 422, 423	20
5	425, 426, 427, 428, 429, 431, 432, 434, 435, 437 438, 440, 441, 442, 443, 445, 448, 449, 450, 452	20
6	453, 454, 456, 457, 458, 460, 461, 463, 464, 468 469, 471, 472, 473, 475, 477, 479, 481, 482, 483	20
7	484, 485, 489, 491, 492, 493, 496, 497, 498, 499 500, 501, 504, 505, 506, 507, 508, 509, 510, 512	20
8	513, 515, 517, 518, 519, 520, 524, 525, 527, 528 529, 530, 533, 535, 536, 538, 540, 542, 544, 550	20
9	551, 552, 553, 554, 555, 556, 557, 559, 560, 561 562, 563, 564, 565, 566, 568, 571, 572, 574	19
10	577, 578, 579, 581, 582, 583, 584, 585, 586, 587 588, 589, 590, 591, 593, 597, 598, 599, 600	19

Table G.2: Testing sets for each of the K=10 folds. The training set for each fold includes the remaining responses not used in the testing set. In total are this set composed of 198 responses in the linear and non-linear respectively. The presented responses associated with the NDS load-set, which are all categorized as **non-linear** and are all having a load-factor=1.5.

Fold, i	Response IDs	Number of Responses
1	602, 604, 606, 607, 609, 610, 611, 612, 614, 615 616, 617, 618, 619, 620, 622, 625, 626, 627, 628	20
2	631, 632, 633, 634, 636, 638, 640, 641, 648, 650 651, 652, 653, 654, 658, 659, 660, 662, 663, 664	20
3	665, 667, 668, 669, 670, 671, 672, 677, 678, 679 681, 682, 683, 686, 687, 688, 695, 696, 697, 699	20
4	702, 703, 704, 705, 706, 708, 709, 711, 712, 713 714, 716, 717, 718, 719, 720, 721, 722, 723, 724	20
5	726, 727, 728, 729, 730, 732, 733, 735, 736, 738 739, 741, 742, 743, 744, 746, 749, 750, 751, 753	20
6	754, 755, 757, 758, 759, 761, 762, 764, 765, 769 770, 772, 773, 774, 776, 778, 780, 782, 783, 784	20
7	785, 786, 790, 792, 793, 794, 797, 798, 799, 800 801, 802, 805, 806, 807, 808, 809, 810, 811, 813	20
8	814, 816, 818, 819, 820, 821, 825, 826, 828, 829 830, 831, 834, 836, 837, 839, 841, 843, 845, 851	20
9	852, 853, 854, 855, 856, 857, 858, 860, 861, 862 863, 864, 865, 866, 867, 869, 872, 873, 875	19
10	878, 879, 880, 882, 883, 884, 885, 886, 887, 888 889, 890, 891, 892, 894, 898, 899, 900, 901	19

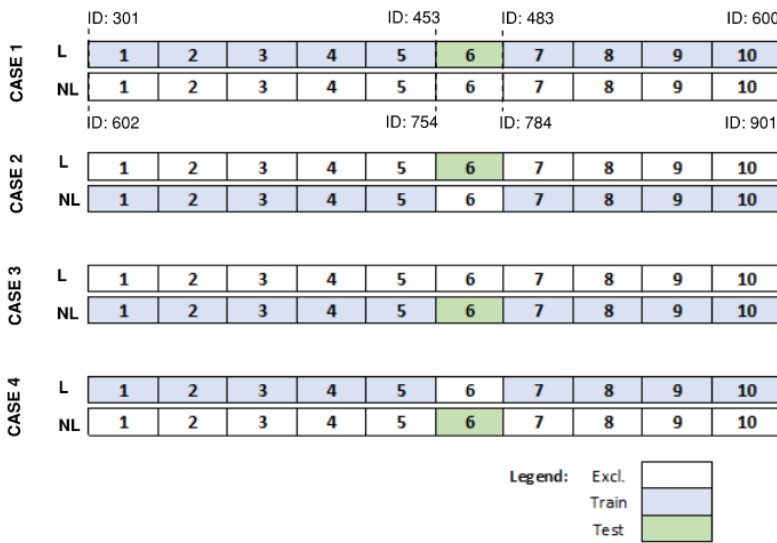


Figure G.1: LDS (L in the figure) and NDS (NL in the figure) divided in 10 folds leading to the dataset introduced in Table G.1 and Table G.2. Composition of the train-set and test-set by sampling from LDS and NDS according to the considered case (Table 5.15).

APPENDIX H

Comparison Gaussian Process & Neural Network

H.1 Comparison of mean error for each floor

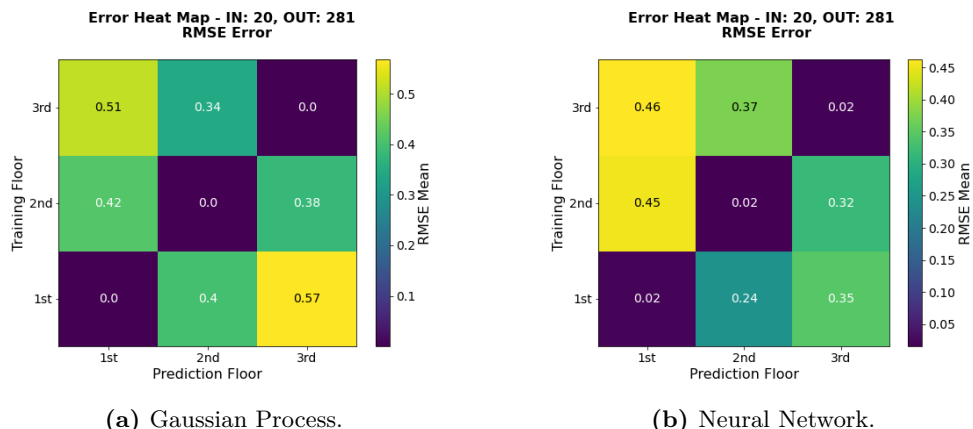


Figure H.1: Mean RMSE measure for each floor, given one node to be used as input that is used to predict responses on a different or the same floor.

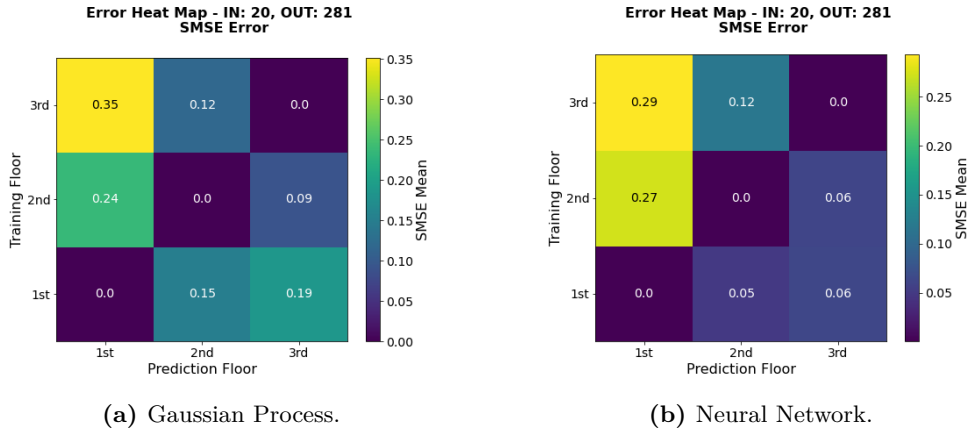


Figure H.2: Mean SMSE measure for each floor, given one node to be used as input that is used to predict responses on a different or the same floor.

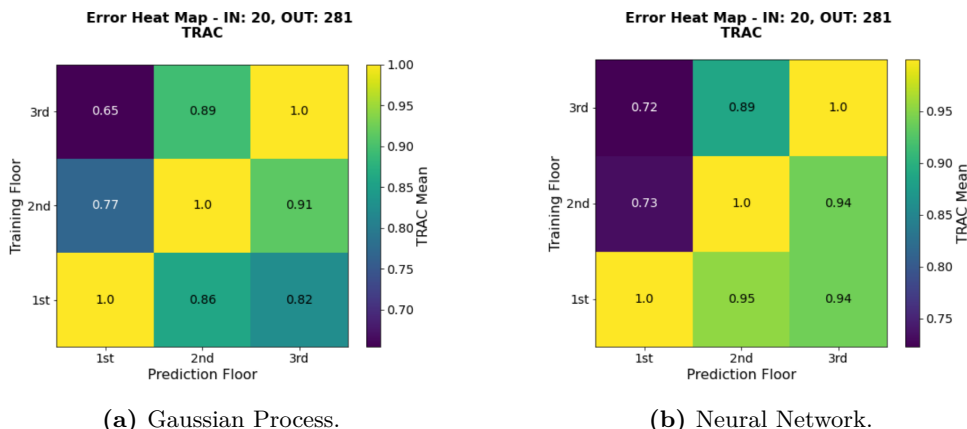


Figure H.3: Mean TRAC measure for each floor, given one node to be used as input that is used to predict responses on a different or the same floor.

H.2 Error Distributions

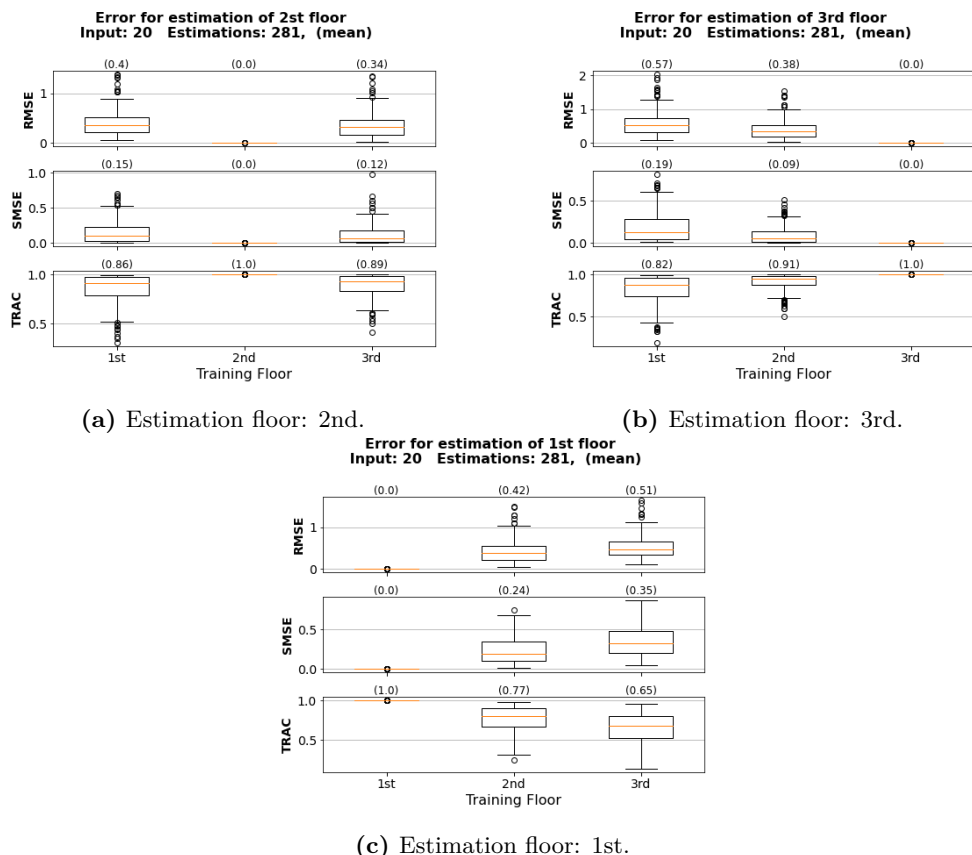


Figure H.4: Gaussian Process distribution of error measure based on the 281 estimation of each floor.

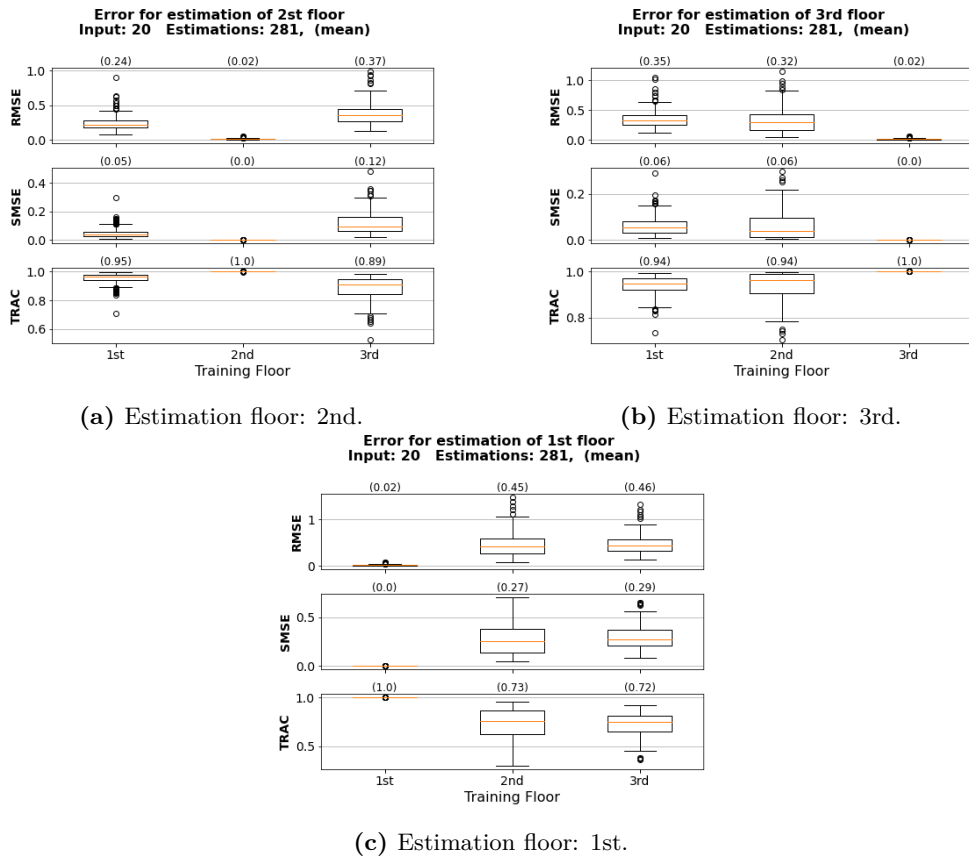


Figure H.5: Neural Network distribution of error measure based on the 281 estimation of each floor.

APPENDIX

Neural Network - Error Distribution

I.1 Distributions of error with noise

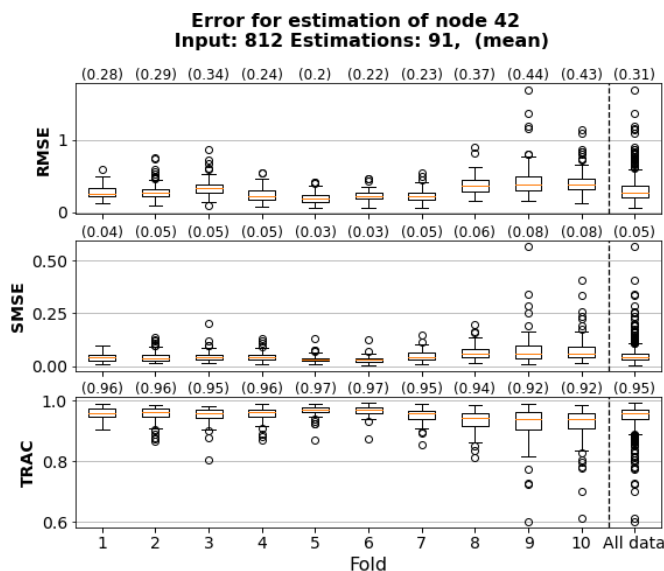


Figure I.1: Distributing of errors given each fold for the NN mode, with no noise. Predictions of node 42 given input from node 23.

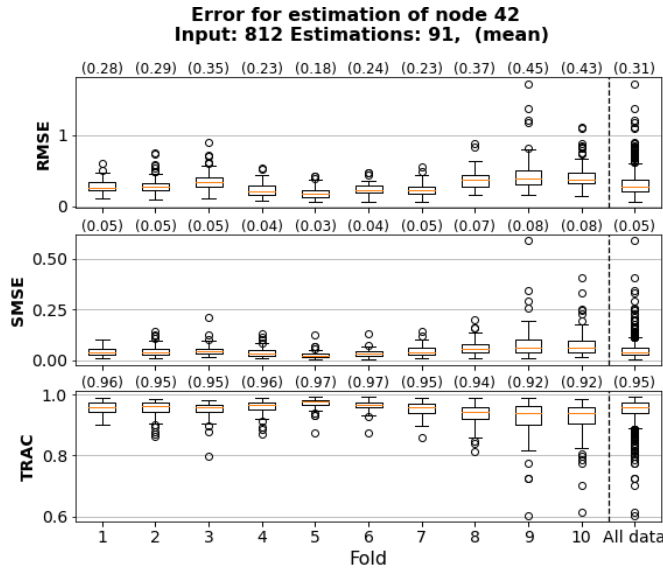


Figure I.2: Distributing of errors given each fold for the NN mode, with noise level 40 dB. Predictions of node 42 given input from node 23.

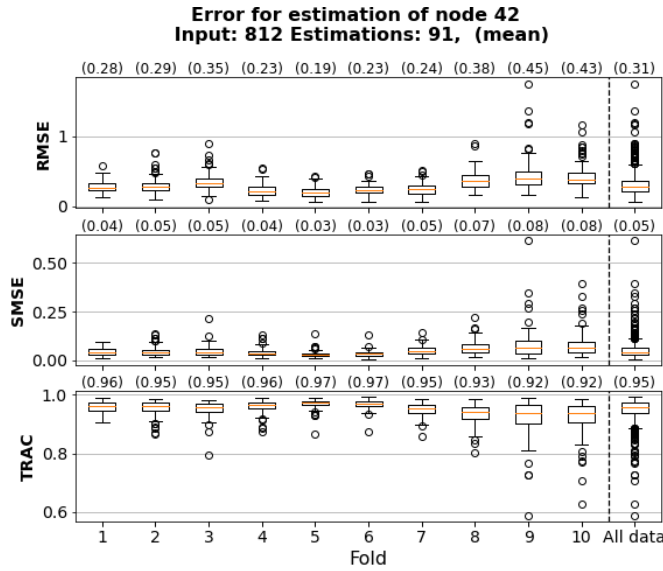


Figure I.3: Distributing of errors given each fold for the NN mode, with noise level 30 dB. Predictions of node 42 given input from node 23.

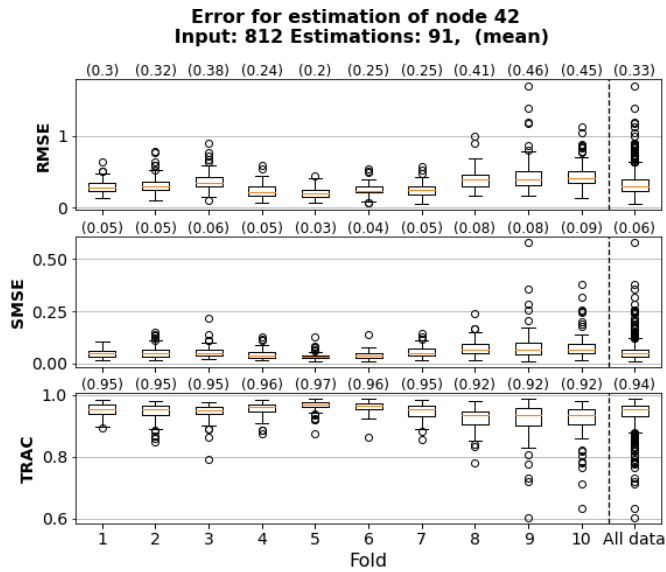


Figure I.4: Distributing of errors given each fold for the NN mode, with noise level 20 dB. Predictions of node 42 given input from node 23.

APPENDIX J

Project Plan

The damage state assessment of structures subjected to extreme loadings, such as intense sea waves and earthquakes, is a key task in the field of civil engineering. Damaged structures may lead to economic losses and in worst cases human casualties, and it is therefore of interest to monitor certain structures, to insure that they are performing sufficiently. The monitoring of structures is also referred to as structural health monitoring (SHM) where damage detection is one of the main activities. The damage assessment of structures can be performed using different techniques e.g. measurements of structural responses, visual inspections, or combinations of several techniques. According to Rytter, these techniques can be used to carry out damage detection at four levels:

- Level 1 - Detection: A qualitative indication that damage is present.
- Level 2 - Localization: The probable location of damage.
- Level 3 - Assessment: The size of damage.
- Level 4 - Consequence: The safety of the structure given a certain damage state.

The complexity and the size of several structures, as well as a potential difficulty to approach and inspect them, have led to the growing use of Machine Learning (ML) in SHM.

The SHM scheme that utilizes ML might be the following phases:

1. Measurement and acquisition of signals related to the structural response such as accelerations.
2. Signal processing and feature extraction.
3. Interpretation using Machine Learning (ML) and classification algorithms.

J.1 Initial Project Concept: 28-09-2022

The aim of the present project consists of the prediction of the damaged or undamaged state of a given structure through the use of Machine Learning (ML). The method of detection will be based on the dynamic responses of a structure with the aim to distinguish between damaged and undamaged structures. By inspiration from Rytters' classification, the damage assessment in this project will be divided into two steps: global assessment and local assessment. The former aims to associate a unique damage index to the whole structure (Levels 1 and 3 in Rytters' classification) while the latter provides the damage level per each structural element (Levels 2 and 3).

The training and testing phases of the ML method will use dataset that includes both dynamic responses of the structure¹ and the correspondent damage state (identified by a damage index) of the structure². To create a dataset that includes various responses from a structure corresponding to several dynamic load cases, a FE model is utilized. In the FEM, the elements are modeled with nonlinear materials therefore, the project will define damage as an inelastic behaviour of the structure.

The FE model provides the necessary information to quantify damage both in the whole structure and in single elements. This makes it possible to label the behaviour of the structure (and elements) with damage indices. Therefore, the state of the structure is either quantified for the entire structure (for the global assessment), or for the individual structural elements (for the local assessment).

The project will deal with supervised ML, since both the input and output to the ML model can be obtained.

¹Dynamic responses will be used as the **input** for the ML method.

²The damage state of structure will be used as the **output** for the ML method.

J.2 Revised Project Concept: 29-01-2023

The project concept and content remain overall unchanged. However, the predicted output provided by the ML method has been changed. The focus was moved from the prediction of damage detection (either local or global) to the prediction of the final state in selected nodes of the structures. In the present project, the local state corresponding to a seismic event is defined as the definition of the acceleration time history experienced from the considered node or point in the studied structure. In order to predict the acceleration signal in a node of the structure, the ML model is inputted with acceleration histories recorded by sensors placed at a certain distance from the considered node. The prediction of the structure's response was relative to a specific excitation generated from an earthquake thus, the predicted signal and the recorded data are associated with the same seismic event.

J.3 Evaluation of the project process

Through this project have topics within both civil engineering as well as computer science been used, in order to make the investigations regarding the non-linear state estimations of a civil structure. Thus, the present project represents the first collaboration between the two departments of DTU Contract and DTU Compute. The different background of the people involved in the project has been truly beneficial with respect to the fulfilment of the project's objectives. The participation of the whole team in the weekly meetings was essential both to keeping track of the progress in the project, but also to mitigate and clarify technical knowledge originated from the different backgrounds of the people involved.

The overall project goal were reached, with fruitful discussions regarding application and further investigations. The project plan as initialized in Figure J.1, was followed with only minor changes related which state of the structure that should be investigated, and the time spent on creating the data-sets used for the investigation. Since the data-construction took less time than expected, more time were used on the estimations using the ML methods. This further made it possible to include an additional ML method, such that in total two methods were investigated.

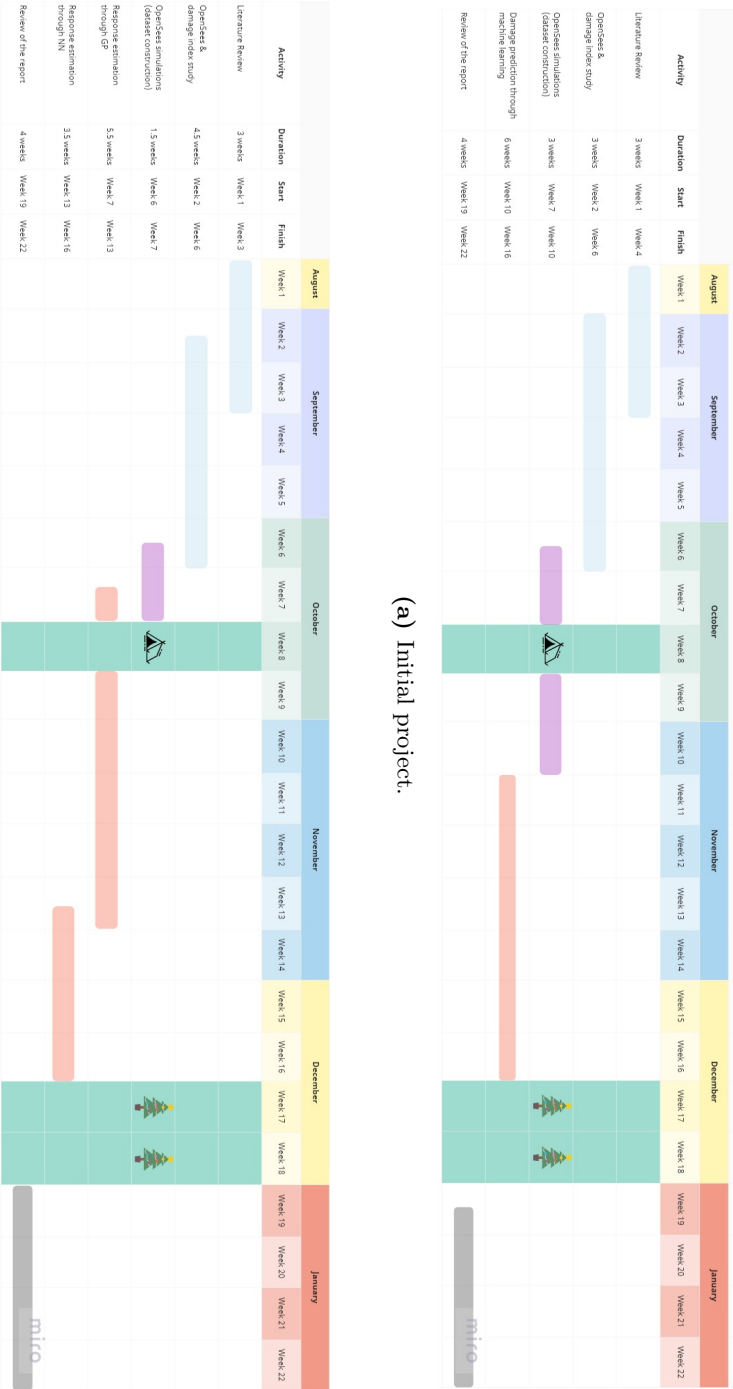


Figure J.1: Gantt-Chart as estimated in the initial and revised project.

